Métrologie en ligne de faisceaux et d'optiques X de synchrotrons

Sébastien Bérujon

UNIVERSITÉ DE GRENOBLE

THÈSE

Pour obtenir le grade de

DOCTEUR DE L'UNIVERSITÉ DE GRENOBLE

Spécialité : **Physique de la matière condensée et du rayonnement**

Arrêté ministérial : 7 août 2006

Présentée par

Sébastien Bérujon

Thèse dirigée par **Eric Ziegler et Kawal Sawhney**
et codirigée par **José Baruchel**

préparée au sein **de l'European Synchrotron Radiation Facility, de Diamond Light Source Ltd**
et de **l'École Doctorale de Physique**

Métrologie en Ligne de Faisceaux et d'Optiques X de Synchrotrons

Développement de Méthodes et Applications

Thèse soutenue publiquement le **13 Février 2013**,
devant le jury composé de :

Prof. Frédéric Livet
Chercheur Emerite au SIMAP - INPG, Président
Prof. Pierre Chavel
Directeur de recherche au CNRS, Institut d'Optique, Palaiseau, Rapporteur
Prof. Gerhard Grübel
Directeur de recherche au Hasylab - DESY, Rapporteur
Dr. Patrick Naulleau
Directeur du centre CXRO - LBNL, Examinateur
Dr. José Baruchel
Ancien directeur du groupe Imagerie - ESRF, Directeur de thèse
Dr. Eric Ziegler
Responsable de la ligne BM05 - ESRF, Co-Directeur de thèse
Dr. Kawal Sawhney
Chef du groupe optique - Diamond LS, Co-Directeur de thèse
Dr. Hongchang Wang
Chercheur - Diamond LS , Invité

Université de Grenoble

European Synchrotron Radiation Facility &
Diamond Light Source Ltd

At-Wavelength Metrology of Hard X-Ray Synchrotron Beams and Optics

Method Developments and Applications

Ph.D. Thesis

April 23, 2013

Sébastien Bérujon

Supervisors:
Dr. Eric Ziegler, Dr. Kawal Sawhney

As the night is falling, intense light sources and bright minds are working continuously for the understanding of the world at the nanoscale

To my future wife

Résumé en français

Cette thèse présente des travaux de recherche de métrologie en ligne de faisceaux de rayons X dans les installations synchrotrons. Deux approches principales ont été étudiées pour extraire la phase d'un front d'onde X : les méthodes dans le domaine X utilisant des réseaux de diffraction et celles utilisant l'effet speckle. L'interféromètre à réseaux X est l'outil le plus répandu et représentatif de la première catégorie. Ses performances et son potentiel furent étudiés dans diverses situations de métrologie en ligne. Les méthodes utilisant le speckle X sont des techniques originales développées au cours de ce projet. Elles utilisent des membranes faites de petits grains diffusants, dont seule la distribution statistique est connue, pour permettre la modulation du front d'onde. Les différentes techniques furent déployées expérimentalement sur les lignes de lumière BM05 de l'ESRF et B16 de Diamond Light Source. Leurs implémentations servirent à la caractérisation de différents composants optiques utilisés pour manipuler les faisceaux synchrotron X et à l'étude de la faisabilité de micro imagerie par contraste de phase avec les sus citées techniques.

Abstract in english

This thesis presents research and development work on synchrotron X-ray at-wavelength metrology methods. Two approaches for measuring the phase of an X-ray wavefront were studied: the grating-based and the speckle-based methods. The X-ray grating interferometer is the most widespread technique representative of the first category. Its performance and potential in various situations encountered in at-wavelength metrology were investigated. Speckle methods are X-ray phase sensing techniques newly developed during this thesis project. They make use of membranes with small features, whose statistical distribution is the only known specification, to modulate the beam wavefront. The different methods were deployed experimentally at the beamlines BM05 of the ESRF and B16 of the Diamond Light Source. Their implementation permitted the characterization of various kinds of optical elements used to manipulate synchrotron X-ray beams as well as the feasibility study of micro phase contrast imaging using the two methods described above.

Contents

Acknowledgement

Three years have been spent on this interesting and motivating thesis project and most results presented in this manuscript would have never been possible without the direct help, advice or inspiration from the people I interacted with.
Starting from the ESRF side, I have of course the greatest thanks to my supervisor Eric Ziegler. He has been a permanent support during these three years: he always found time to share his knowledge, make me benefit from his great experience and had a constant concern of making me learn and become the best researcher possible. His trust combined to the freedom of action he let me have were invaluable sources of motivation and skills development.
In Grenoble, I had the pleasure to work and interact with the staff of the BM05. I shared a lot with my coworkers about science of course but also as friends on various interests. I had the pleasure to meet and work from the beginning with Raphael Kluender, David Ghigo, Fabio Maziello, Luca Peverini, Tamzin Lafford, Jean-Yves Massonnat, Xavier Guichard, Genziana Bussone, Frederico Segato and Marc Dubrulle. Later, I really enjoyed working on the IBF project with Franck Demarcq and Iulian Preda.
I'm really grateful to Roberto Cerbino who I had the chance to meet at the beginning of my project. He kindly explained to me his work and revealed me the way to take benefit from it. I also had the chance to have the visit of Igor Kozhevnikov from Russia who taught me his approach for mirror figuring.
More widely, I had the privilege to be a member of first the Experience Division at ESRF and then of the Instrumentation division. Many people helped me in various ways to pursue my project: in this occasion I wish to address my thanks to Jean Susini, Ray Barrett, Irene Zanette, Timm Weitkamp, Amparo Vivo, Peter Cloetens and Lynda Graham.
I also have special thanks for Virginie Bonne and Aymeric Larrue who I met at ESRF and later helped me a lot to not become an Oxford homeless.
My gratitude goes to Pr. Pierre Chavel who transmitted me his meticulousness and his constant matter of clear science during our interviews.
Any experiment requires technical and related support and Jean-Yves Massonnat,

Andy Malandain and Graem Barlow were invaluable help for the set up of the experiments.
On the Diamond side I also have many thanks to give to my colleagues. I am greatly thankful to Kawal Sawhney who accepted me and trusted me from the beginning of this project. His confidence and support have been a major asset to my work.
I have special thanks to my closest Diamond collaborator Hongchang Wang. I shared with him a lot of knowledge and beamtimes at Diamond, from which a lot of meaningful results could come out.
I shared, during my time at Diamond, my office with Ian Pape who was more than a simple officemate. Thank you Ian for the fruitful discussions and for your great support. Likewise, Simon Alcock has been a precious help in many important circumstances.
I would like to acknowledge the people with whom everything really started, i.e. the people who decided of my selection and offer me the opportunity to spend these years working on this challenging and motivating project. This include the people involved in the selection process from both institutions ESRF and Diamond and who accorded me their trust: José Baruchel, Kawal Sawhney, Eric Ziegler, Pierre Chavel, Benedicte Henry-Canudas and probably some others.
Similarly, I'm very grateful to the people who intervened at the other end of this project. I acknowledge the jury members for the time they agreed to spend on my work and especially Gerhard Grübel and Pierre Chavel for their review of the manuscript.
I wish to express my warm thanks to my family. Although they never fully understood what my work consisted of, they have always support my carrier choices.
I acknowledge my friends, in particular the ones I have not been in contact for a while but will always be there when needed.
Last, I have thanks for Fabien Balezeau, Cameron Geddes, Pierre Graebling and many others for various reasons.

1 Introduction

1.1 Context

Since the first experiments taking advantage of X-ray sources based on synchrotron radiation, the interest for the X-ray beam properties provided by such facilities has kept growing. Synchrotron X-ray sources now offer X-ray beams with unprecedent intensity, collimation and coherence properties. Through various specific techniques, these beams permit the investigation of matter and its structure down to the atomic scale. Naturally, new developments and improvements on the source stimulate constant efforts to provide ever better instruments and methods to take full advantage of the source properties. This fact is particularly true in the field of nano-spectroscopy and high resolution X-ray imaging. Indeed, looking at a sample at the nanoscale puts strong challenges on aspects such as the beam coherence, the quality of the optics and the stability and positioning of the investigated sample at the nanometer scale. The constant progress observed in the fields of mechanics and X-ray sources during the last decades instills confidence into the researchers ability to meet these requirements. Nonetheless, substantial achievements on the performance of X-ray optics elements are needed until routine nanoscale experiments to become possible.

The performance criteria of X-ray optics include the capacity to concentrate the beam in a nanometer size area and the ability to propagate the beam wavefront emitted by the source through the optics without introducing optical aberration. The optical elements used in the hard X-ray regime differ in many aspects from the ones employed with visible light. As a matter of fact, because the wavelength for X-rays is several orders of magnitude smaller than the one of visible light, the shape profile and the surface roughness quality factors of the optics must be improved by the same order of magnitude.

Adaptive optics is an alternative approach to obtain the desired shape. Instead of using a monolithic mirror, the reflective surface is mechanically distorted to correct for manufacturing imperfections as well as for the unavoidable defects and instabilities of the beam. The beam defects are the sum of the imperfections coming from the various elements present in the beam, including the windows, and even the source. Thus, the production of diffraction limited experiments requires metrology capable of taking the effective state of the beam into account with an accuracy approaching the atomic length scale.

Online or at-wavelength metrology methods are seen as the natural path to this endeavor as they account for the X-ray optics effective performance affected, for instance, by the thermal load and the mechanical strains of any object present along the X-ray beam path. This can only be accurately known by investigating the beam itself. Owing to this intrinsic principle, the development of high sensitivity, high resolution at-wavelength methods is a cornerstone for nano-experiments to become routine.

Techniques analyzing the X-ray propagation direction may find applications beyond beam and optics metrology; when the spatial resolution of a metrology method is high enough, one can think for instance of exploiting the technique for imaging applications. Imaging methods sensitive to the beam propagation direction are called phase contrast imaging methods by opposition to the absorption imaging ones. Phase contrast imaging techniques are presently under thorough investigations as they are able to image the inner structure of light materials, such as biological samples, that show only low absorption contrast. The possibility of transposing imaging methods to metrology and vice versa is a subject of high interest to both communities, as they take advantage of the same principle, i.e. the monitoring of beam propagation.

1.2 Projects and work

While metrology laboratory instruments are reaching the repeatability and accuracy necessary to characterize diffraction limited hard X-rays optics, at-wavelength methods are still at an early development stage. Hence, in industrial optical production, the metrology is still performed using visible light instruments. In fact, only a few techniques based on visible light are effectively transposable to the X-ray regime. While the short wavelength of X-rays is expected to provide online metrology techniques with a higher accuracy than visible light based instruments, their routine implemen-

tation at synchrotrons is slowed down by technical issues. These constraints will be explained in the first part of this manuscript. The synchrotron physics and principles will be exposed in Chapter 2, while the instrumentation will be detailed in Chapter 3. Chapter 4 will then be dedicated to a quick overview of the phase sensing methods that were available at the time this project started.

The core work of this thesis aims at fulfilling, at least partly, the demands the community had for at-wavelength methods and their use for optical characterization during routine experiments. At the beginning of the project, two main at-wavelength technique categories were identified as interesting candidates: grating based methods and speckle technique. Since both method categories had their advantages and issues, parallel development was conducted on each of them.

The X-ray grating interferometer (XGI) was already a well known instrument in the synchrotron community. This device had proven great imaging capacities in phase contrast experiments. Today, the XGI is appreciated for its high phase sensitivity, in the order of a fraction of a wavelength, and also for the scattering map it is able to provide when imaging a non homogeneous sample. A more complete description of the grating interferometry technique is provided in Chapter 5. Nevertheless, only few works were carried out on the use of the XGI for metrology purpose. One goal of this thesis project was to push the metrology possibilities of the grating interferometer further for beam and optics characterization, using either the one or two dimensional versions.

The second kind of method considered uses near-field speckle. Many methods of the visible domain take advantage of the speckle effect obtained when using coherent light, to provide accurate metrology measurements. In contrary, no metrology method based on the use of speckle was available with X-rays at the inception of this thesis. The idea was to use a particular X-ray speckle regime labeled as 'near-field' speckle, characterized by the property to be space invariant upon propagation and independent of the source features. A large part of the thesis project consisted in setting up a technique that would make use of these invariant speckle grains. Indeed, their shape is similar to needles matching the trajectory of the rays, and so, by numerical tracking of pixels subset between speckle images, it was possible to infer the path of the photons. The outcome showed that the newly developed method, named XST, an acronym for X-ray Speckle Tracking, presents many advantages over previously available online metrology methods. The development of XST and the breakthrough it brought to the field of beam and optics characterization will be detailed in Chapter 6.

As unexpected, the work conducted on these two kinds of methods ended up merging into a single one. The unification of the XGI and XST speckle method will be explained in Chapter 7 where the XGI will be described as a special case of a more general method that uses any near field pattern containing high spatial frequency features.

A last method for characterizing reflective optics, based on a grating, will be described in Chapter 8. Although this method may seem, at first glance, related to the XGI, its principle is quite different. Full description of the technique and discussions related to the XGI methods will be exposed in this chapter.

The third part of this manuscript will aim at describing applications of the methods previously described and developed. Study cases of transmission X-ray optical elements such as the Fresnel zone plate (FZP) and the Compound Refractive Lens (CRL) investigated using at-wavelength metrology methods will be presented in Chapter 9.

Chapter 10 will briefly present an ESRF development program initiated in 2005 that aims at producing nanofocusing mirrors starting from a flat silicon substrate.

Chapter 11 is dedicated to the application of online metrology to X-ray adaptive optics, or, more precisely, correctable bimorph and KB bender mirrors. Beam focusing and wavefront correction using reflective optics is an active topic within the synchrotron X-ray community. Demonstration of the efficiency of the at-wavelength metrology methods and their proper implementation for adaptive optics will be demonstrated.

The imaging potential of the developed method will be investigated. The emphasis will be put on the spatial resolution aspect of the methods with respect to the sensitivity obtained when using the technique for metrology purposes. Some illustrative imaging study cases are presented within the second part of this manuscript, while deeper investigation work are presented in Chapter 12, especially about micro phase contrast imaging.

A summary of the accomplished work is ending this manuscript together with a discussion on the perspectives for further developments.

Introduction en Français

Contexte

Depuis les premières expériences scientifiques ayant su exploiter les propriétés uniques des faisceaux de rayons X produits par rayonnement synchrotron, l'intérêt montré par les chercheurs pour l'utilisation de tels faisceaux s'est révélé toujours croissant. Les sources de rayonnement synchrotron offrent aujourd'hui des faisceaux de rayons X aux propriétés de luminance et de cohérence sans précédents qui permettent, grâce à des techniques diverses, d'investiguer la matière à l'échelle nanométrique. Naturellement, les développements et progrès apportés aux accélérateurs motivent de façon permanente des développements équivalents dans les techniques et les instruments afin de bénéficier de façon optimale de ces avancées. Ces développements sont observés en particulier dans les domaines de la nanospectroscopie et de l'imagerie X à haute résolution pour lesquels les propriétés de cohérence des faisceaux, la qualité des optiques et la stabilité mécanique sont des facteurs cruciaux.

Alors que les avancées apparues dans les domaines de la mécanique et des sources permettent aujourd'hui de satisfaire un certain nombre d'exigences imposées par l'échelle nanométrique, d'importants challenges demeurent encore concernant la réalisation des éléments optiques.

La performance des optiques pour rayons X est d'une grande importance pour transporter de la lumière X de la source à l'échantillon sans en dégrader la qualité de son front d'onde, en particulier lorsqu'il s'agit de réduire la taille du faisceau par focalisation. La très courte longueur d'onde des rayons X durs et leur faible interaction avec la matière imposent des solutions optiques très différentes de celles employées avec la lumière visible. Les erreurs de forme et de rugosité des optiques doivent être diminuées de quatre ordres de grandeurs par rapport à celles des optiques visibles pour espérer obte-

nir les performances attendues par la diminution de la longueur d'onde. Les optiques adaptatives sont une alternative parfois employée dans le régime X pour approcher la forme parfaite recherchée. Au lieu d'utiliser un substrat monolithique, la technique utilise un miroir déformable pour lequel l'application de distortions locales permet de corriger certaines imperfections de conception. Ce genre d'optique offre aussi la possibilité de compenser des imperfections du faisceau incident, induites, par exemple, par les défauts des objets présents sur la trajectoire du faisceau. Ainsi, la production de miroirs parfaits, c'est à dire aux performances seulement limitées par la diffraction, nécessite de disposer d'une métrologie capable à la fois de tenir compte de l'état réel du faisceau X sonde et de fournir une précision approchant l'échelle atomique.

La métrologie en ligne ou dite « à la longueur d'onde » utilise les rayons X pour la mesure et donc tient compte de l'état du faisceau incident : ainsi elle est pressentie par la communauté scientifique comme la méthode la plus amène d'atteindre ces objectifs exigeants. La métrologie en ligne permet, par exemple, de considérer et d'inclure les charges thermiques ou mécaniques d'un système dans son environnement réel, contrairement à l'usage d'un instrument de metrologie utilisant la lumière visible. De par leur principe, les méthodes de métrologie en ligne et l'amélioration de leurs performances sont amenées à jouer un role essentiel dans la réalisation en routine d'experiences à l'échelle nanométrique.

Les techniques permettant d'analyser la direction de propagation des photons à l'intérieur d'un faisceau X trouvent aussi des applications en dehors du champ de la métrologie. L'imagerie par contraste de phase en est l'exemple le plus probant : au lieu d'utiliser l'absorption des rayons X par les objets, cette technique d'imagerie mesure la distorsion du front d'onde avec une haute résolution spatiale. Ce type de méthode s'avère tres attractif pour l'imagerie de l'intérieur de tissus mous, tels que des échantillons biologiques, lequels ne fournissent que peu de contraste par absorption. Du fait que la phase du front d'onde est là aussi la quantité mesurée, la perspective de transposer les techniques de métrologie à l'imagerie et vice versa est particulièrement interessante.

Projets et buts

Les instruments de métrologie employés aujourd'hui dans les laboratoires dédiés permettent d'obtenir des mesures de précision et de répétabilité suffisantes pour la pro-

duction d'optique de rayons X aux performances quasiment uniquement limitées par la diffraction. Il en est toutefois autrement des méthodes de métrologie en ligne, lesquelles en sont encore à un stade primitif de développement. Cet état de fait est plus particulièrement observable dans le milieu industriel de production des optiques X où, actuellement, la métrologie employée est systématiquement basée sur des instruments optiques opérant dans le spectre visible ou proche de celui-ci. Un frein important au développement de la métrologie à la longueur d'onde de travail réside dans la grande difficulté à transposer ou importer des techniques traditionnelles de l'optique visible dans le régime des rayons X durs. La faible interaction des rayons X avec la matière limite grandement le potentiel des méthodes optiques traditionnelles qui seraient transposées dans ce régime. Ainsi, en dépit de la courte longueur d'onde des rayons X, supposée offrir des performances de métrologie supérieure, les niveaux de performances théoriques ne sont toujours pas atteints.

Les contraintes engendrées par l'utilisation de rayonnement synchrotron seront abordées dans la première partie de ce manuscrit. Les principes de physique des sources synchrotron seront expliqués dans le chapitre 2 et l'instrumentation employée sera présentée dans le chapitre 3. Le chapitre 4 sera consacré à une revue des méthodes de métrologie à la longueur d'onde disponibles au commencement de ce projet. Le but de ce projet de recherche était de combler, du moins en partie, le besoin de la communauté synchrotron en méthodes de métrologie en ligne, en vue de la caractérisation d'optique au cours d'expériences de routine. Au commencement du projet, deux techniques distinctes ont été identifiées comme des candidates prometteuses : l'interférométrie à réseaux et les techniques utilisant le speckle. Du fait que chacune de ces méthodes possedait son lot d'avantages et d'inconvénients, et surtout de spécificités, elles ont été développées en parallèle.

L'interférométrie était, déjà avant le commencement de ces recherches, une technique bien connue et largement utilisée par la communauté synchrotron. Elle a su prouver ses capacités d'imagerie par contraste de phase, capacités maintenant utilisées lors d'expériences en routine. Comparativement à d'autres méthodes de phase, l'interféromètre à réseaux est apprécié pour sa très bonne sensibilité, de l'ordre d'une longueur d'onde, et pour la cartographie de la dégradation de cohérence qu'elle fournit dans le cas d'échantillons inhomogènes. Une plus ample description de l'interférométrie à réseaux X sera fournie dans le chapitre 5. En dépit d'une utilisation dans de nombreux domaines, peu de travaux se sont attachés à son usage en métrologie, et ce malgré des expériences pionnières en 2005 démontrant son potentiel pour la caractérisation d'optiques en réflexion. Le but du projet était ainsi d'améliorer et d'optimiser les pos-

sibilités de l'interféromètre pour la caractérisation d'optiques X, que ce soit avec les réseaux, anciens, à une dimension ou avec les nouveaux à deux dimensions.

La seconde catégorie de méthodes retenue est basée sur l'utilisation de speckle en champ proche. De nombreuses techniques de métrologie utilisent déjà l'effet speckle dans le domaine visible, lequel est facilement observable dès lors que de la lumière employée est cohérente. En revanche, aucune méthode en ligne n'utilisait l'effet speckle X au début de ce projet. L'exploitation du speckle en champ proche est intéressante du fait de ses propriétés de propagation uniforme ainsi que de son indépendance vis-à-vis des caractéristiques de la source. Une part importante du projet a consisté à développer et à mettre au point une technique tirant avantage de ce type de speckle. La forme en aiguille des grains de speckle en champ proche a pu être utilisée comme traceur de trajectoires des rayons X. En appliquant des algorithmes de suivi entre des petits ensembles locaux de pixels, il a été possible de déduire les trajectoires des photons. La nouvelle méthode établie, nommée 'X-ray speckle tracking', présente plusieurs avantages en comparaison avec les méthodes disponibles au préalable. Les percées réalisées avec la technique de speckle en champ proche seront présentées dans le Chapitre 6.

A partir de l'étude des méthodes utilisant le speckle et les réseaux, une théorie beaucoup plus globale regroupant ces deux approches a été développée, conduisant à une nouvelle technique dite globale, laquelle est développée dans le Chapitre 7. Il y est notamment démontré comment l'interféromètre à réseau, vu dans le contexte de cette nouvelle théorie, représente un cas particulier de cette méthode globale.

Une autre méthode pour la caractérisation d'optique pour rayons X en réflexion sera aussi décrite dans le Chapitre 8. Bien que celle-ci puisse, au premier abord, sembler similaire à l'interférométrie à réseaux, son principe en est pourtant distinct.

La troisième et dernière partie de ce manuscrit vise à présenter différentes applications expérimentales des méthodes étudiées dans la partie II. Des caractérisations en ligne de différents optiques X y sont décrites. Il s'agit par exemple, dans le Chapitre 9, de la caractérisation de lentilles réfractives et de zones de Fresnel.

Le Chapitre 10 présente brièvement un programme de développement initié en 2005 à l'ESRF et visant à produire des miroirs focalisant à l'échelle nanométrique, en partant de substrats plans en silicium.

Le Chapitre suivant est dédié aux applications de la métrologie en ligne aux optiques

adaptatives. Dans le domaine synchrotron, ces miroirs sont du type bimorphe ou à courbure dynamique. La focalisation de faisceaux utilisant ces optiques est un sujet d'intérêt pour les lignes de lumière synchrotron. L'implémentation et la démonstration de l'efficacité des méthodes développées pour l'optimisation des optiques adaptative de rayons X seront fournies dans le Chapitre 11.

Le potentiel des méthodes développées pour les applications de microscopie a été étudié, en particulier concernant les aspects relatifs à la sensitivité et à la résolution spatiale. Des études de cas d'imagerie de phase sont présentées dans la seconde partie de ce manuscrit et des résultats de recherches plus poussés en microscopie seront fournis dans le Chapitre 12.

Un résumé des travaux accomplis et des résultats obtenus conclura ce manuscrit ; il sera suivi d'une discussion sur les perspectives possibles dans le domaine.

Part I

Present status of synchrotron at-wavelength metrology

2 Background in synchrotron X-ray beams

The substantial investment made in third generation synchrotron facilities is justified by the various advantages synchrotron sources present over traditional X-ray sources. A common given factor to assess the quality of the source is its brilliance, a figure that quantifies the intensity in photons per second per surface unit, per 0.1% energy bandwidth and per angular divergence. In addition to the brilliance of synchrotron X-ray sources, many orders of magnitude higher than the one of laboratory sources, the synchrotron X-ray beam is partially coherent. That implies that two electromagnetic waves generated by the source can interfere with each other creating an usable contrast intensity pattern. To realize the stakes and challenges in X-ray optics and metrology, one has to understand how X-rays are produced, propagate and interact with matter.

In this chapter we will make a short presentation of the X-ray sources and of synchrotron radiation, explain how X-rays interact coherently with themselves and with matter and present two means of predicting their propagation in free space. One striking and important effect of the X-ray free space propagation known as the Talbot effect, will be presented in the last section of this chapter.

2.1 X-ray sources

One can find several kinds of hard X-rays source, i.e delivering photon energies in the $[5-200]$ keV range. Most experiments exploiting X-rays are nowadays still conducted using X-ray tubes or synchrotron radiation based sources. However, X-ray laser via Compton scattering, free electron laser (FEL) or laser-plasma interaction based sources are for instance new or promising technologies for the production of X-rays.

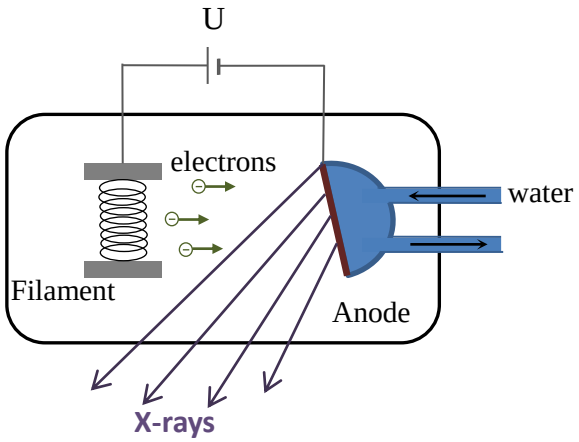

Figure 2.1: Schematic diagram of an X-ray tube.

2.1.1 X-ray tubes

The discovery of the X-rays by Wilhelm C. Röntgen in 1899 resulted from an experimental setup which we would call today X-ray tube. It consisted of a glass tube maintaining electrodes under vacuum. Röntgen observed that when an electric discharge was strong enough to free electrons from the cathode, the acceleration of these electrons towards the anode followed by their collision was generating radiation. The capacity of such radiation to go through matter soon awarded him a Nobel prize. Later, the X-ray tube technology experienced a lot of technical improvements among which the cooling of the anode and the development of filament based cathodes (cf. Fig. 2.1), that are still employed in nowadays tubes.

From a more physical point of view, X-rays from a tube are produced within two phenomena: Bremsstrahlung and fluorescence. Bremsstrahlung corresponds to the deceleration of the electrons when colliding the anode followed by a drastically slow down process due to electron-atom interaction. This effect results in the emission of electromagnetic radiation whose properties depend on the voltage applied between electrodes and on the amount of electrons colliding the anode. The spectrum of the emitted radiation is continuous and almost constant in intensity.

In addition to the X-rays generated by Bremsstrahlung effect, an X-ray tube produces radiation through ionization of the bounded electrons in the anode material. The recombination of the vacancy in the atomic electron configuration with an electron from an upper shell leads to the emission of short wavelength radiation. This fluorescence phenomenon creates sharp peaks in the emission spectrum that are characteristic of the anode material.

Typical voltages applied to the electrodes range from 10 keV to 100 keV with currents up to 0.5 A. The flux of the emitted X-ray beam is proportional to the electron current. However, as the temperature of the anode increases with the current, the evacuation of the heat generated on the anode, which represents 99% of the electron energy, puts technical limitations on the maximum beam intensity that can be generated.

The X-ray tubes found nowadays differ mostly from their cooling system and target material. As no such source was intended to be used during this thesis no further description will be provided on this topic. However, the development of the metrology techniques described further in this manuscript was done keeping in mind their potential adaptability to X-ray tube sources. Such accomplishment would extend their use to the broad community of users of laboratory sources.

2.1.2 Synchrotron sources

In a synchrotron, X-rays are produced from a physical effect equivalent to Bremsstrahlung occurring in an X-ray tube: the electromagnetic field emission is promoted by the acceleration of charged particles. The difference between Bremsstrahlung and synchrotron radiation lies in the speed of the accelerated particles. While the electrons in an X-ray tube are accelerated to energies up to 100 keV to emit radiation isotropically, the ones produced in a third generation synchrotron have a quasi relativistic speed with an energy of several GeV. Seen from an observer at rest, the electromagnetic field emitted by the particle is then collimated in a narrow cone with an ellipse as base. Using the Lorentz equations, one can demonstrate that the opening angle of the synchrotron radiation emission is inversely proportional to the energy of the accelerated electrons. The vertical opening angle of the radiation cone is usually expressed as $\frac{1}{\gamma}$, where γ is the energy of the accelerated electrons in unit of the rest mass energy that is: $\gamma = \frac{E_c}{m_e c}$ where m_e is the electron rest mass and E_c the energy of the photons. Therefore, the faster the electrons, the less diverging the X-ray beam emitted will be, thus making the synchrotron source much more brilliant one than the X-ray tube source.

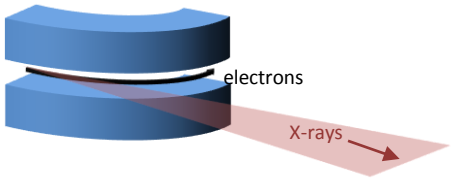

Figure 2.2: Sketch of a bending magnet.

In practice, a synchrotron is not circular but made of straight sections separated by

short curved sections. Both beamline BM05 at ESRF and B16 at Diamond Light Source use X-rays produced in bending magnets as sketched in Fig. 2.2. These magnetic dipoles, located in the curves of the storage ring, apply permanent magnetic fields: the field lines are oriented vertically to the moving direction of the electrons, generating an angular deviation of the electrons as displayed in Fig. 2.3. Passing through the magnetic field $\overrightarrow{B}$ at a velocity v, the electrons are deviated by the Lorentz force $\overrightarrow{F_l} = e\overrightarrow{v} \times \overrightarrow{B}$ that gives them a circular motion. This motion corresponds to a constant tangential acceleration that causes the emissions of an electromagnetic field from the charged particle.

The energy spectrum emitted by a bending magnet, such as the ones of ESRF BM05 and Diamond B16, is large, covering a spectrum from few eV to more than a hundred of keV. The characteristic energy E_c of these sources is defined by the storage ring properties and corresponds approximately to the peak of radiated power in the energy spectrum. Its mathematical definition is given by [1]:

$$E_c = \frac{3}{2}\hbar\gamma\omega_o$$

where ω_0 is the electron circular frequency inside the storage ring and $\hbar$ the reduced Planck constant.

At the ESRF beamline BM05, X-rays are created by a dipole applying a magnetic field of 0.85 T onto the electrons of the 6 GeV storage ring. The characteristic X-ray energy is of 19.9 keV for a total emitted power of $\sim$ 350 W for the usual intensity of 200 mA circulating in the ring. At beamline B16 of Diamond, the magnets induce a field of 1.4 T at the 3 GeV electrons position, giving a characteristic energy of 8 keV. Characteristic electron beam sizes and divergences for the two beamlines are summed

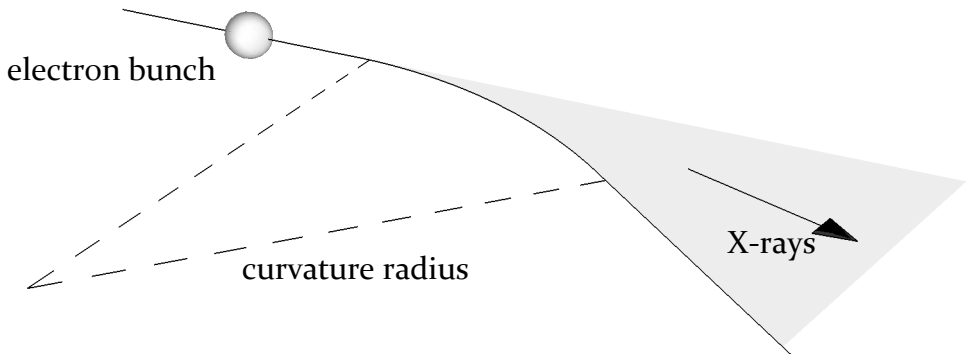

Figure 2.3: Trajectory of the electrons in a bending magnet (Sketch courtesy of R. Kluender).

	σ_x (μm)	σ_y (μm)	σ'_x (μrad)	σ'_y (μrad)	Flux (ph./s/0.1%BW)
Diamond B16	53.7	23.7	81.4	2.6	4×10^{11}
ESRF BM05	86	12.7	98	3	3.5×10^{11}

Table 2.1: Machine parameters (rms) of the ESRF BM5 and Diamond B16 bending magnets for $E = E_c$. Horizontal $\sigma_x(\mu m)$ and vertical $\sigma_y(\mu m)$ source sizes, and horizontal $\sigma'_x(\mu rad)$ and vertical $\sigma'_y(\mu rad)$ electron beam divergences.

up in Table 2.1.

A more efficient alternative to the bending magnets for producing synchrotron X-rays consists of using an insertion device, placed in one of the straight sections of the storage ring [2]. Instead of making the electrons describing a single piece of arc like in a bending magnet, the insertion device forces the electrons to execute oscillations in the horizontal planes (see Fig. 2.4). Such trajectories are obtained by making the electrons passing through an array of permanent magnets alternating polarity. Because the total radiated waves seen by an observer is the superposition of all the rays generated in each arc of the insertion device, the beam produced by such a source is much more intense than the one produced by a bending magnet on the same electrons.

There are basically two kinds of insertion devices: wigglers and undulators. Within wigglers, radiation emitted from the N arcs of the electron trajectory will be summed incoherently and the device will act as the sum of N bending magnets: the emitted spectrums will be equivalent to the one of a bending magnet but N times more intense.

Conversely, within an undulator the spatial frequency of the magnets is tuned to have the electrons oscillate in phase along the magnet of the device. The final intensity they produce is the coherent sum of all radiations emitted, i.e. the square of the amplitude sum. Undulator technology permits to obtain much greater beam brilliance thanks to a better beam collimation and a quasi monochromaticity. The energy radiated in this kind of insertion device is localized in spectrum peaks: the first largest peak is found around the fundamental designed frequency and the other peaks are harmonics of it.

As all experiments described in this manuscript were conducted on bending magnet source beamlines, no further description of the radiation emitted by the insertion device will be given here. However, the interested reader can see Ref. [3, 4] for more

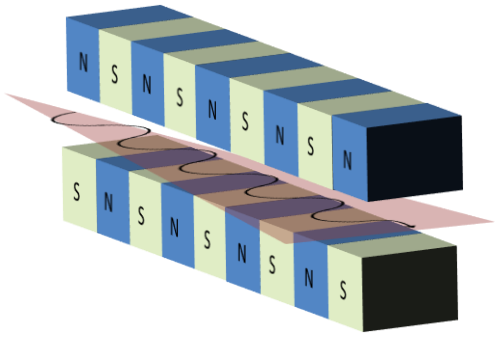

Figure 2.4: Sketch of an insertion device.

information.

2.2 X-ray coherence

One of the most striking property of synchrotron radiation from a third generation facility is coherence: this phenomenon permits the creation of observable contrast interferences. What we describe more specifically under the term coherence is actually the correlation between wave-fields at two different points in space and/or time. In a coherent beam, correlation between photon states occurs in a stationary way, i.e both temporally and spatially, leading to recordable interference patterns.

The coherent nature of synchrotron radiation is essential for most methods presented in this manuscript. Almost all techniques employed and developed here use the beam coherence to take advantage of interference patterns to obtain high contrast from non absorbing objects. It should be noticed that, because laboratory sources are not coherent, the techniques of this project are not directly transposable and applicable to X-ray tube sources.

The statistical relation between two complex field functions $u_1(x_1, t_1)$ and $u_2(x_2, t_2)$ can be expressed with the function $< u_1(x_1, t_1)u_2^*(x_2, t_2) >$ where $< . >$ denotes the temporal average and $*$ the complex conjugate. From this notation, two aspects of the coherence for contrast to arise are distinguishable: the first one is the longitudinal or temporal coherence and the second one is the transverse coherence, referring to the spatial properties of the source.

2.2.1 Longitudinal or temporal coherence

Temporal coherence relates to the monochromaticity of the source: when a detector records the superposition of different wavelength waves, the total collected intensity is the temporal sum of the waves. For interferences to arise and be observable, the waves have to be in phase. When the phase difference between waves gets larger, the interference visibility decreases and finally vanishes at anti-phase. This interference visibility can be described by the modulus of the normalized self coherence function [5]:

$$\gamma_t(\tau) = \frac{< u(t)u^*(t+\tau) >}{< u(t)u^*(t) >} \tag{2.1}$$

For a pure monochromatic beam ($\Delta\lambda = 0$), wavefields would be perfectly correlated at any time over an infinite propagation distance: one can show that $|\gamma(0)| = 1$ and decreases monotonically to 0.

Using $\tau = \frac{l_l}{c} = \frac{1}{\Delta\nu}$ where $\Delta\nu$ is the difference between the two frequencies of waves, the characteristic longitudinal coherence length can be expressed, assuming a gaussian line in the spectrum, by:

$$l_l = \frac{\lambda^2}{2\Delta\lambda} \tag{2.2}$$

This equation defines the distance at which, after propagation, two waves with wavelengths λ_1 and λ_2 will be out of phase by a factor $\pi/2$. At this distance, directly related to the energy bandwidth of the X-ray beam, waves will interfere partially and $|\gamma(\tau)| = \frac{1}{2}$. Thus, the monochromaticity is defined by the ratio $\frac{\Delta\lambda}{\lambda}$ or equivalently with $\frac{\Delta E}{E}$.

As seen previously, a bending magnet source emits a very large spectrum while an undulator spectrum is peaked with peaks having a width $\Delta E/E$ of several percents. To create in practice a high monochromaticity, beamlines use monochromators to select a narrow energy peak and obtain an energy resolution higher than the undulator peak. In the[10-20] keV range, the achievable longitudinal coherence length goes up to 10 μm ($\Delta E/E \approx 10^{-5}$), but it is usually of ~ 1 μm ($\Delta E/E \approx 10^{-4}$). This last energy selectivity corresponds to the use of Si(111) crystal based monochromators that are a reasonable choice for flux and setup simplicity (cf. 3.2.4).

2.2.2 Transverse or spatial coherence

While the degree of temporal coherence is particularly important in spectroscopy, for imaging applications it is the level of spatial coherence that matters. Indeed, in spite of a small source size, the short wavelength of the X-rays makes synchrotron beams only partially spatially coherent which imposes stringent conditions on the observation of wave interferences.

The transverse coherence length in a given spatial plane is linked to the source size s and to the distance z to it. Considering here a pure quasi-monochromatic wave, the mutual intensity of waves at two point x_1 and x_2 in a plane located at a distance z from the source is defined by:

$$J(x_1, x_2) =< u(x_1)u^*(x_2) > \tag{2.3}$$

When $x_1 = x_2$, the mutual intensity is equal to the usual observable intensity: $I(x_1) = |u(x_1)|^2$. The complex coherence factor γ_s is the normalized version of the mutual intensity:

$$\gamma_s(x_1, x_2) = \frac{J(x_1, x_2)}{\sqrt{J(x_1, x_1)J(x_2, x_2)}} \tag{2.4}$$

Following the same principle as for the normalized self coherence function, we have $\gamma_s = 1$ when $x_1 = x_2$, i.e when two waves originate from the same source point. The function γ then decreases to 0 as $\Delta x = x_2 - x_1$ increases. The function of Eq. 2.4 is used to predict and qualify the visibility of an interference pattern.

One standard theorem in optics to predict the coherence propagation function for an extended partial coherent source, is the Van Cittert theorem set in 1941. This theorem, later extended to a more generalized version by Goodman, is mathematically expressed by:

$$J_z(x_1; x_2) = \frac{\kappa(\overline{x})}{\lambda^2 z^2} \exp\left(\frac{i2\pi\overline{x}\Delta x}{\lambda z}\right) \tilde{I}_0\left(\frac{\Delta x}{\lambda z}\right) \tag{2.5}$$

where z is the observation distance from the source, $\tilde{I}_0$ is the Fourier transform of the function I_0, and $\overline{x} = \frac{x_1+x_2}{2}$. This relation expresses the spatial coherence property of the radiation emitted from a planar incoherent source in terms of the two-dimensional Fourier transform of the source intensity distribution. One important consequence brought up by the theorem is that the spatial coherence length can be improved upon free propagation in space. For these reasons, long beamlines are built at synchrotron facilities to increase the spatial coherence length.

The transverse coherence length l_t is more generally defined by the distance separating two points(x_1, x_2) such that $|\gamma_s(x_1, x_2)| = \frac{1}{2}$. At an observation distance z from the source and from Eq. 2.5, l_t can be approximated in function of the FWHM size s of the source as:

$$l_t \approx \frac{\lambda z}{2s} \tag{2.6}$$

Typical transverse coherence lengths at sample positions and for $E = 14.5$ keV are given for the Diamond's beamline B16 and the ESRF BM05 in Table 2.2. Due to the asymmetry of the source shape, one can easily predict a discrepancy between the transverse coherence lengths in the vertical and horizontal directions, and hence a different interference fringe visibility behavior along the two directions.

	Vertical (μm)	Horizontal (μm)
Diamond B16 ($z \sim 47$ m)	28	11
ESRF BM05 ($z \sim 40$ m)	25	10

Table 2.2: Typical transverse coherence lengths measured at sample position after a double crystal monochromator at E = 14.5 keV.

2.3 X-ray interaction with matter

An optical wave, which can be described by a complex field function $u(x, y, z) = u_0(x, y, z)e^{i\omega t}e^{i\phi(x,y,z)}$, is defined by four parameters: its amplitude u_0, its frequency $w/2\pi$, its phase ϕ and its polarization. In the hard X-ray regime, polarization properties of synchrotron light are exploited for magnetic studies with techniques using reflection geometry such as resonant and non-resonant magnetic X-ray scattering. For an experiment using a quasi-monochromatic beam, the wavelength or wave frequency is usually defined by either using a monochromator (cf. 3.2.4) or by taking advantage of a peaked source spectrum (cf. 2.1.2). Thus, the two parameters of interest for an X-ray imaging or a metrology experiment are the amplitude and the phase. As mentioned previously, the cause of the decrease of amplitude of a wave is called absorption and a change of its phase is called phase shift. For a given material and a given X-ray pulsation ω, the optical wave interaction with matter is described by the complex refractive index:

$$n_\lambda(x, y, z) = 1 - \delta_\omega(x, y, z) + i\beta_\omega(x, y, z) \tag{2.7}$$

This notation is often employed for X-rays because the small interaction of X-rays with matter, n being very close to unity. In this equation, β and δ are real numbers denoting respectively the attenuation and the phase shift induced upon X-ray transmission through matter. Thus, the propagation of a wave-field in a material along the z direction is following the equation:

$$\begin{aligned} u(x,y,z) &= u(x,y,0)e^{i\frac{2\pi}{\lambda}\int_0^z n_w(x,y,z)dz} \\ &= u(x,y,0)e^{i\frac{2\pi}{\lambda}}e^{-i\frac{2\pi}{\lambda}\int_0^z \delta dz}e^{-\frac{2\pi}{\lambda}\int_0^z \beta dz} \end{aligned} \tag{2.8}$$

As detectors are sensitive only to the intensity of the beam, i.e the sum of the square waves amplitude (see 3.3), the attenuation of the waves after a propagation distance is defined by:

$$A_{bs}(x,y,z) = \frac{|u(x,y,z)|^2}{|u(x,y,0)|^2} = e^{-\frac{4\pi}{\lambda}\int_0^z \beta dz} \tag{2.9}$$

And the phase shift is:

$$\delta\phi(x,y,z) = \frac{2\pi}{\lambda}\int \delta_w(x,y,z)dz \tag{2.10}$$

The transmission function T is sometimes used to define the propagation effect through an object of the wave-field:

$$T(x,y,z) = A_{bs}(x,y,z)e^{-i\delta\phi} \tag{2.11}$$

and then:

$$u_o(x,y) = T(x,y)u_{inc}(x,y) \tag{2.12}$$

One can show that $\beta(\omega)$ and $\delta(\omega)$ increase with the material electron density (higher for materials of higher atomic number Z), and proportionally to λ^2. By definition, under vacuum, no interaction exists and $\beta = \delta = 0$. A complete mathematical description on how to calculate the refractive index of the elements can be found in [6]. In practice, these values are obtained directly from a data booklet or an equivalent dedicated software.

For low-Z materials, such as the ones composing biological tissues, when increasing the energy, the β value of the material drops much quicker than the δ value. Indeed, at energies far enough from the absorption edges, the material absorption value decrease with the photon energy following a law proportional to $\beta(\lambda) \propto \lambda^4 \propto \frac{1}{E^4}$ while the δ value decreases only at a rate $\beta(\lambda) \propto \lambda^2 \propto \frac{1}{E^2}$ [6]. In imaging, techniques sensitive to the phase shift rather than the attenuation, find great interest for the study of light materials and dose-sensitive samples. As shown in Fig. 2.5, the δ/λ ratio for

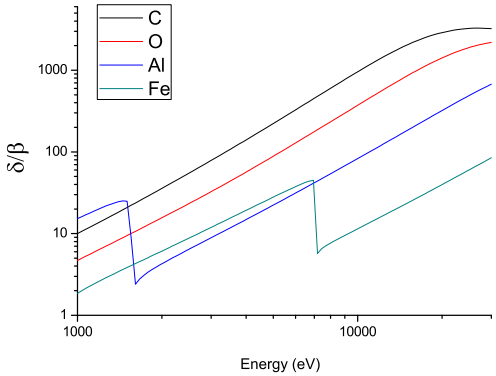

Figure 2.5: Ratio δ/β for light elements

some materials can reach up to a factor 1000 for hard X-rays, which translates into an important gain in contrast when imaging the phase shift rather than the absorption. Phase sensitive techniques are also of interest to distinguish materials having similar attenuation coefficients.

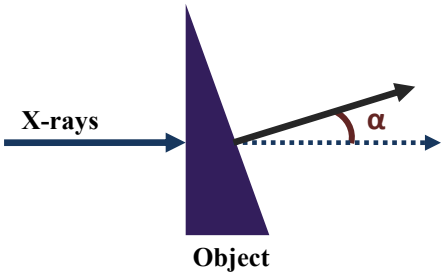

Figure 2.6: Definition of the refraction angle

As stated previously, detectors are not directly sensitive to the phase shift (cf. 3.3). Nevertheless, the latter can be recovered from the measurement of the refraction effect induced by a phase shift. A beam wavefront is defined as the surface W for which $\phi(W)$ is constant so that $\phi = \frac{2\pi}{\lambda}W$. One can show that X-rays propagate in the direction normal to the wavefront surface. Thus, using geometrical considerations [7], the refraction angle α (see Fig. 2.6) can be linked to the phase gradient of the beam by the equation:

$$\alpha(x,y) = \nabla W = \frac{\lambda}{2\pi}\nabla\phi(x,y) = \nabla\int \delta_\omega(x.y.z)dz \tag{2.13}$$

where ∇ is the nabla operator, i.e here the gradient operator.

This equation is the base for most of the work presented in this manuscript. By measuring the deflection angle α, one can recover, after integration, the wavefront and then the δ value of the sample. For metrology purpose, the photon propagation

direction being the key information for analyzing optics defects, the wavefront surface W is used and analyzed directly as it is homogeneous to a length. Conversely for phase imaging, the goal being to map the δ factors of a sample, the calculated map will be usually expressed in term of the phase shift $\delta\phi$.

2.4 X-ray beam propagation

Having discussed the way synchrotrons produce X-rays, we now envisage their propagation in free space. The following will adopt an optical point of view and distinguish two regimes of light propagation: the near field or Fresnel regime and the far field or Fraunhofer regime.

2.4.1 Near-Field

The near field is the region located at short distance beyond a diffracting aperture where the Fresnel approximation defined below holds.

An optical wave u can be represented as a sinusoidal function of time and space, which is, for convenience, often written as a complex form:

$$u(x, y, t) = U(x, y, t)e^{i(\mathbf{k}.\mathbf{r}-2\pi\omega t)} \tag{2.14}$$

where $\mathbf{k}$ is the wavevector with wavenumber $k = \frac{2\pi}{\lambda}$ and $\omega = E/\hbar$ is the carrier frequency. The wavevector $\mathbf{k}$ expresses the propagation light direction while the carrier frequency ω is proportional to the X-ray energy and can be calculated using the relation:

$$E = \frac{hc}{\lambda} \tag{2.15}$$

In equation 2.14, because the detector acquisition time is performed at a scale much larger than $1/\omega$, the carrier frequency component is often dropped. Furthermore, changing the spatial dependency of the wave with a phase factor from an origin, one can write:

$$u(x, y) = U_0 e^{i(\mathbf{k}.\mathbf{r}-\phi(x,y))} \tag{2.16}$$

In this equation U_0 represents the magnitude amplitude of the wave at the origin.

Photo-detectors, called here detectors, are only sensitive to the radiant power falling onto their sensitive surface S, i.e to the square magnitude of the optical wave amplitude:

$$I(S) =< |u^2(S,t)| > \tag{2.17}$$

where the bracket denotes the averaging over the acquisition time. One can infer from this property, that absorption contrast imaging will be a straight-forward process while phase sensing will be a more complex one. Indeed, sample X-ray absorption can be calculated from the ratio of the intensities falling onto the detector when the sample is in and out of the beam. Meanwhile, the photons phase information is lost when taking the modulus of the wave amplitude.

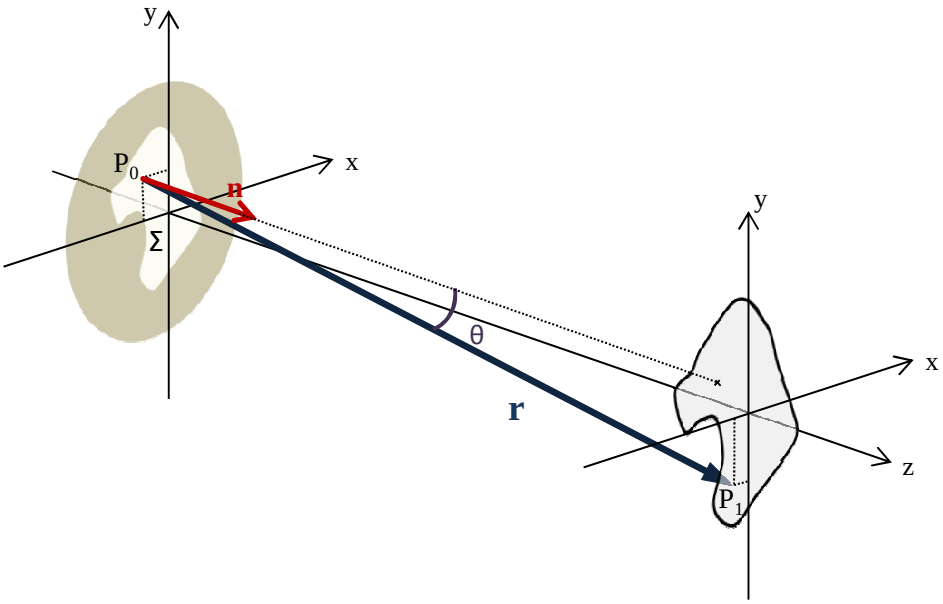

Figure 2.7: Geometric consideration for X-ray free space propagation.

As displayed in Fig. 2.7, we consider a wavefield $u_0(x,y)$ in a plane of an aperture Σ: the Huygens-Fresnel states that at a point of a plane located further away from an aperture, the wavefield is equal to the superposition of all the incoming sub-waves from the aperture. More mathematically, the calculation of the wavefield $u_1(x,y)$ at the point P_1 located at a distance z from the aperture, can be done using the Huygens-Fresnel equation derived using the first Rayleigh-Sommerfeld approximation [8, 9]:

$$u_1(x,y) = \frac{1}{i\lambda}\int_\Sigma u_0(x_0,y_0)\frac{e^{i\mathbf{k}.\mathbf{r}}}{|\mathbf{r}|}\cos(\mathbf{n},\mathbf{r})dx_0dy_0 \tag{2.18}$$

where $\mathbf{r}$ is the propagation vector from (x_0,y_0) to (x,y) and $\cos(\mathbf{n},\mathbf{r}) = \cos(\Theta)$ is the obliquity factor for a source located far away from the diffracting aperture plane Σ.

This equation can be simplified in the case of small diffraction angles Θ, also named

the paraxial approximation. This condition is almost always fulfilled in the hard X-ray regime because of the angles involved in the X-ray regime are small, i.e in the order or less than a few milliradians. Considering this approximation and noting $|\mathbf{r}| = r$, Eq. 2.18 can be simplified with:

$$\cos(\mathbf{n}, \mathbf{r}) = \frac{z}{r} \tag{2.19}$$

and using a Taylor expansion:

$$r = \sqrt{z^2 + (x - x_0)^2 + (y - y_0)^2} \tag{2.20}$$

At the first order approximation, we obtain:

$$r \approx z + \frac{(x - x_0)^2}{2z} + \frac{(y - y_0)^2}{2z} \tag{2.21}$$

Because $z >> (x - x_0)$ and $z >> (y - y_0)$, r can be approximated by z in the denominator of equation 2.18. Yet, such substitution is not permitted in the exponential factor as this one changes really quickly even for a fraction of radian. Substituting Eq. 2.19 and 2.21 in Eq. 2.18, we end up with the Fresnel diffraction formulae:

$$u_1(x, y) = \frac{e^{ikz}}{i\lambda z} \int_\Sigma u_0(x_0, y_0) \exp\left\{ i\frac{k}{2z}[(x - x_0)^2 + (y - y_0)^2] \right\} dx_0 dy_0 \tag{2.22}$$

Noticing that Eq. 2.22 is a convolution operation, one can express the electromagnetic field downstream the aperture using:

$$u(x, y) = \int\int_{-\infty}^{\infty} u(\xi, \nu) h(x - \xi, y - \nu) d\xi d\nu \tag{2.23}$$

where h is the convolution kernel:

$$h(x, y) = \frac{e^{ikz}}{i\lambda z} \exp\left[i\frac{k}{2z}(x^2 + y^2) \right] \tag{2.24}$$

In this case h is the impulse response of free space propagation: its use in the Fourier space permits to reduce the calculation of the field to the multiplication with the propagator $H(f, g) = \mathcal{F}[h(x, y)] = \exp[-i\pi\lambda z(f^2 + g^2)]$.

2.4.2 Far-Field

The far field regime or Fraunhofer approximation describes the limit of the Fresnel equation when the source and the observer are infinitely distant from the illuminated object. With X-rays, neutrons or electrons that have a very short wavelength, Fraunhofer diffraction patterns can be directly obtained by, for instance, observing a small aperture from a distance located a few meters away from it. In Eq. 2.22, if in addition to the Fresnel conditions, we consider a collimated beam and $z >> \frac{k(\xi^2+\nu^2)_{max}}{2}$, then the equation of the field can be written under the form [8]:

$$u(x,y) = \frac{e^{ikz}e^{i\frac{k}{2z}(x^2+y^2)}}{i\lambda z}\int\int_{-\infty}^{\infty} u_0(\xi,\nu)e^{-i\frac{2\pi}{\lambda z}(x\xi+y\nu)}d\xi d\nu \tag{2.25}$$

Aside from the multiplication phase factor in front of the integral, this expression corresponds to the Fourier transform of the aperture distribution. A criterion usually employed to judge the validity of the Fraunhofer approximation is to satisfy $z >> \frac{2D^2}{\lambda}$ where D is the aperture diameter. This distance corresponds to several meters in the hard X-ray regime for a characteristic aperture of a few tens of microns.

The far field regime is used in several X-ray techniques, including in X-ray crystallography [10], ptychography [11, 12] and coherent diffraction imaging [13]. All these techniques permit to achieve very high spatial resolution representation of an object structure because of the large scattering vectors measurable upon propagation. Again, as detectors are only sensitive to intensity, the phase retrieval problem remains the key issue which can be solved using different approaches [14, 15].

Although ptychography was reported as a usable technique for online metrology [16, 17], no experiment or any attempt was made to work in the far field regime during the course of this project. All the techniques explored in this manuscript used the near field regime, that is at quite short distance from the aperture.

2.4.3 The Talbot self imaging effect

One important effect arising from the Fresnel diffraction was discovered by Lord Talbot in the 19^{th} century [18]. When illuminating a periodic structure with a coherent quasi-monochromatic plane wave, perfect images of the structure are replicated at regular distances: they are called self-images. Sub-images having a multiple of the frequency

are also observable at fractional distances. This effect intervenes in many optical techniques using visible light and also in the X-ray regime as we shall see with the grating interferometer.

The Talbot effect occurs for both absorbing and phase objects. For a collimated beam and in the paraxial approximation, the standard Talbot distance is defined for a structured object with a period p by [18]:

$$Z_T = \frac{2p^2}{\lambda} \tag{2.26}$$

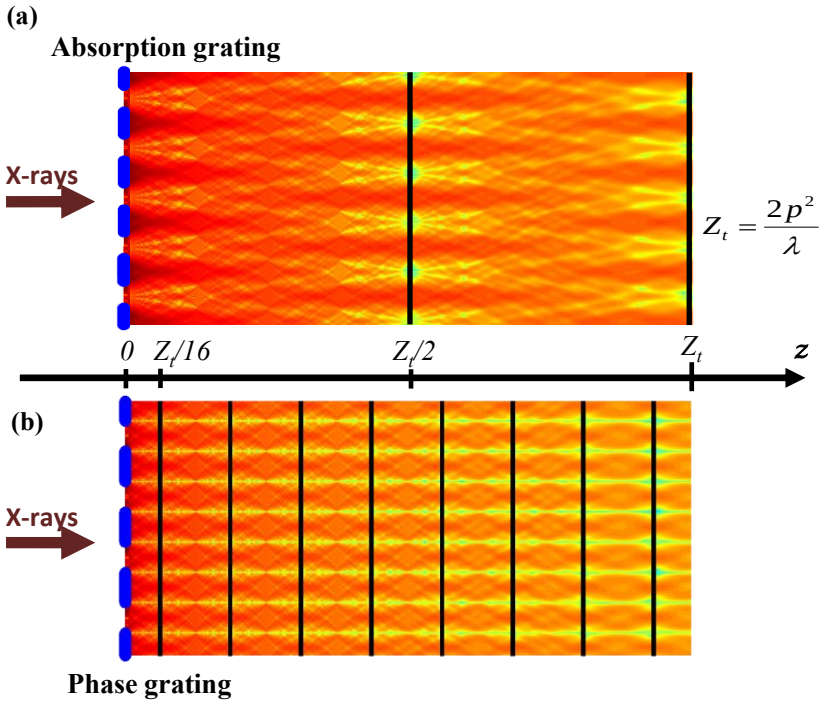

Figure 2.8: Simulation of a Talbot carpet for: (a) an absorption grating (b) a π-phase grating. One can notice the different bright planes where the periodic patterns are replicated for the absorption and phase grating.

In the X-ray regime, conditions to observe the Talbot effect are easily fulfilled and the phenomenon is often encountered. Theoretically, the two limit cases are usually distinguished, namely for an absorbing periodic object and for its phase equivalent. In reality, objects act as a superposition of these two situations. Let us consider here the common case of a periodic object with a duty cycle $\omega = 0.5$. For an absorbing structure, the diffracting pattern will be replicated every half Talbot length, and, doubled in frequency each time the distance Z_T is divided by a factor two. A Talbot carpet simulated for such an absorption grating is shown in Fig. 2.8.(a). For a phase object, the replication behavior of the pattern is also dependent on the phase shift

induced by the structure [19]. At an exact distance Z_T away from the periodic object, no contrast is observable. The self-images of the structure are only replicated at fractional orders of the Talbot distance. An illustration for a π phase shift grating is displayed in Fig. 2.8-(b).

In order to differentiate planes where a same spatial frequency is observed, fractional Talbot distances have been defined with:

$$Z_{Tn} = \frac{n}{m} Z_T \tag{2.27}$$

with n and m some integers. For instance, for a π-phase shift grating, $m = 16$ and the fractional Talbot order n is defined by: $Z_{Tn} = \dfrac{np^2}{8\lambda}$, $n = 1, 3, 5, ...$ At each distance Z_{Tn}, a periodic pattern of frequency $f = 2/p$ will be observable.

An abundant literature dealing with the Talbot effect and the fractional Talbot distances for various kinds of structures and different duty cycles, is available. The reader can find information on developments and mathematical derivations of the effect in Ref. [20, 21, 22, 19, 23].

During this project, the Talbot effect manifestation was encountered in several circumstances: the π-phase shift grating of the grating interferometer is one of them, and the speckle another case. Indeed, the Talbot effect is a general effect not restricted to the case of perfect periodic structure. The Fourier transform permits to decompose any pattern into a superposition of periodic structures, for which the Talbot effect applies individually. Hence, for a given distance, only certain spatial frequencies of an object can be sensed by phase contrast.

As an illustration of this Talbot effect for general objects, Fig. 2.9 [24] shows an image of Brownian particles recorded at a certain distance from the object and its corresponding spectrum. From the sample features, the spectrum was expected to be continuous with presence of most frequencies. However, one can observe rings in the amplitude spectrum. They reflect the amplification and annihilation of some frequencies by the Talbot effect. At a certain distance z, each scattering vector q from the object is modulated by the Talbot transfer function [24]: $2\sin^2 \dfrac{q^2 z}{2k}$. To recover all the spectrum information of an object, one needs to collect several images at different z positions as performed, for instance, with the holotomography technique (cf. Sec. 4.3).

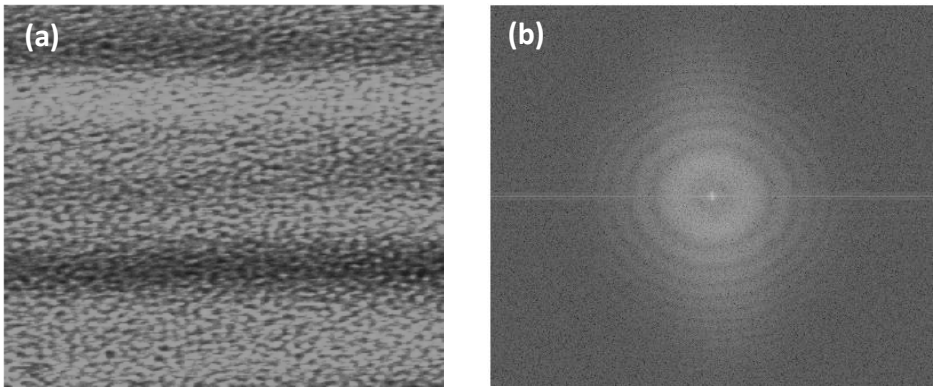

Figure 2.9: Influence of the Talbot effect on the spatial spectrum of a speckle pattern. (a) Recorded image of a speckle pattern, containing various spatial frequencies. (b) Module of the Fourier spectrum of the image: due to the Talbot effect, rings corresponding to specific frequencies are highly visible, alternated with spatial frequencies for which the corresponding images are invisible.

3 Synchrotron instrumentation

In this chapter are presented the instruments and the optics available at synchrotrons. The first section describes the beamline layouts and more specifically the two used during this project: the ESRF Instrumentation Facility BM05 and the Diamond Test beamline B16. The main purpose of this thesis being the online characterization of various synchrotron optical elements, the next section presents a short description of their principles. Since any data acquisition requires a detector, knowledge of its technology is important as well to understand the limitations and the errors it can introduce. The last section of this chapter shortly presents the laboratory based metrology instruments available and used for X-ray optics characterization at synchrotrons.

3.1 Synchrotrons Beamlines

3.1.1 The ESRF BM05 beamline

Most experiments performed at the ESRF were carried out at the Bending Magnet beamline BM05. This beamline is schematically represented in Fig. 3.1 and the specifications are more detailed in Ref. [25].

The X-ray photons of the beamline are produced by a 0.85 T bending magnet on a 6 GeV storage ring. The photon flux and spectrum of the source is continuous as described in Sec. 2.1.2: the peak flux is of $2.7 \times 10^{13} ph./s/mrad2/0.1\%BW$ with a spectrum varying from 6 to 60 keV and with a critical X-ray energy of 19.9 keV. The X-rays first pass through the front end and a first beryllium window at a distance of 23 m from the source. This one is used to isolate the high vacuum (pressure 10^{-10} hPa) of the storage ring from the in-vacuum section of the beamline (10^{-9} hPa) ending at ~ 24 m from the source with a second Beryllium window. Downstream this element, the

various monochromators and the beam pipes in the optics hutch are operated under a slowly flowing He-atmosphere.

All the experiments conducted during this project used monochromatic beams; the photon energy was selected, depending on the experiment, with either one of the two available monochromators:

- The Si(111) double crystal monochromator is located at 27 m from the source. The beam is reflected sequentially on two nearly perfect silicon crystals with a well polished surface, rendering a spectral selectivity of $\Delta E/E \approx 2.10^{-4}$, i.e the one of the Darwin width of the silicon 111-reflections. The two independent crystals are water cooled.

- The two-bounce multilayer monochromator is located at 29 m from the source. This monochromator consists of two silicon mirrors coated with Ru/B_4C layers. Its spectral selectivity is $\Delta E/E \approx 2.10^{-2}$ and, like the other monochromator, is water cooled.

Some attenuators can be inserted along the beam upstream these monochromators although rarely used for this work because of flux issues, and to avoid additional beam wavefront aberrations.

The X-rays enter the experimental hutch at 31 m from the source. Right after a pair of secondary slits selecting the beam coming from one or the other monochromator, a kapton window ends the He-filled beam pipe and the beam starts traveling in air. At this level a fast shutter allows short X-ray exposure times on the sample (down to 5 ms), and is also compulsory when using a CCD technology based detectors to avoid electronics reading errors.

The detector used was usually placed 8 m downstream the shutter, on a versatile granite based Multi-Purpose Platform (MPP). This station allows the mounting on three independent towers of the optics under investigation, diagnostic devices and detector. Each of the towers is equipped with a set of motors to allow various translation and rotation movements.

The Online Mirror Surfacing Station (cf. Sec. 10), when in use, was placed right before the (MPP) horizontal diffractometer, i.e $\sim$ 39 m from the source. The station was also equipped with a set of motors allowing the accurate positioning of the mirror

sample with respect to the X-ray beam for online metrology.

To reduce the photon absorption caused by the long propagation distance of the X-rays in air in the experimental hutch, pipes filled with flowing He were occasionally mounted between the Kapton window and the sample. One has to realize that each additional pipe introduces two additional Kapton windows along the beam path.

Several pairs of slits located at different positions along the beamline are available to clip the beam to a desired size.

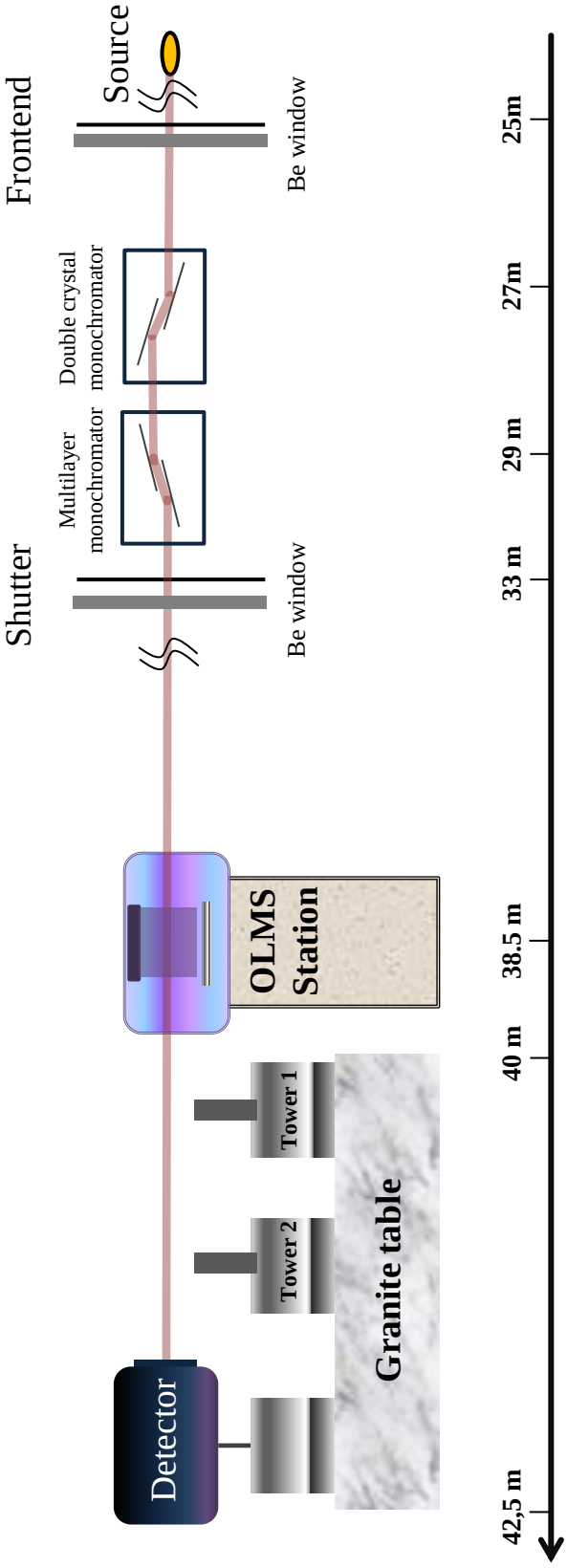

Figure 3.1: ESRF beamline BM05 sketch.

3.1.2 The Diamond Test beamline B16

Experiments at Diamond Light Source were conducted at the Test Beamline B16. This is a flexible and general purpose beamline where a variety of experimental configurations can be set up with relative ease. A schematic of the beamline optical layout is shown in Fig. 3.2 and further details can be found in Ref. [26].

On this beamline, the X-ray photons are produced by a bending magnet on the Diamond 3 GeV storage ring where the electron current is maintained constant, nominally at 300 mA, by operating the machine in a *top-up* mode. One special feature of the beamline is that no window separates the beamline and the storage ring, and all the permanent optical components of the beamline are at ultra high vacuum. The first and the only window (200 μm thick Be) is located 43m downstream from the source, and is used to separate the UHV of the beamline from the ambient atmosphere of the Experimental hutch. The X-ray beam exits from this Be window.

The beamline comprises two monochromators mounted in series – either one can be brought into the synchrotron beam to provide monochromatic X-rays of different bandwidths, or they can be used in tandem, when the monochromatic beam with a very high harmonic-suppression is generated. One monochromator is based on the more commonly used Si(111) crystals and configured as a double crystal monochromator (DCM), that provides a fixed-exit X-ray beam for all photon energies in the 4 - 30 keV range. The other monochromator, Double Multilayer Monochromator (DMM) is based on synthetic multilayers (Ni/B_4C for $<$ 8 keV and Ru/B_4C for 8 - 25 keV) and is also configured in a double bounce geometry. The Si DCM is located at 22 meters from the source and 25 m upstream from the optics table where the sample and analyzer used in the present project were mounted. The energy resolution of this monochromator is $\Delta E/E \sim 10^{-4}$ rendering a photon flux of 2×10^9 ph/sec at the sample position.

The multilayer monochromator has about two orders of magnitude larger spectrum bandwidth ($\Delta E/E \approx 2\%$) and provides much higher photon flux ($\sim$ 70 times) compared to the Si DCM.

A dynamically bent toroidal focusing mirror is also available in the optics hutch of the beamline and is able to provide a focused beam with high flux anywhere between 20 m downstream the mirror and infinity. Despite offering the possibility to increase the flux by a factor >100, this mirror degrades a lot the beam wavefront, restricting its use mainly for spectroscopy technique rather than imaging ones. Therefore, this

mirror was not used in the experiments described in this thesis.

A series of filters of different materials located between the source and the monochromator are available to reduce the photon flux and/or harden the beam if desired.

The experimental hutch of B16 has two experimental stations: a 5-axis diffractometer located at 44 m from the source and a versatile optics table located at $\sim$ 3 m downstream of the diffractometer. The main experimental station employed for the present project was the versatile optics table located 47 m from the source. This equipment is mechanically very robust and has three independent towers allowing 3 translations and 3 rotations each to samples and optical analyzers. The upstream diffractometer was also used sometimes to install some conditioning pre-optics for our experiments. A high level of automation and remote control is available on all Diamond beamlines, with motors and detectors being controlled through the EPICS and the GDA data acquisition software [27, 28].

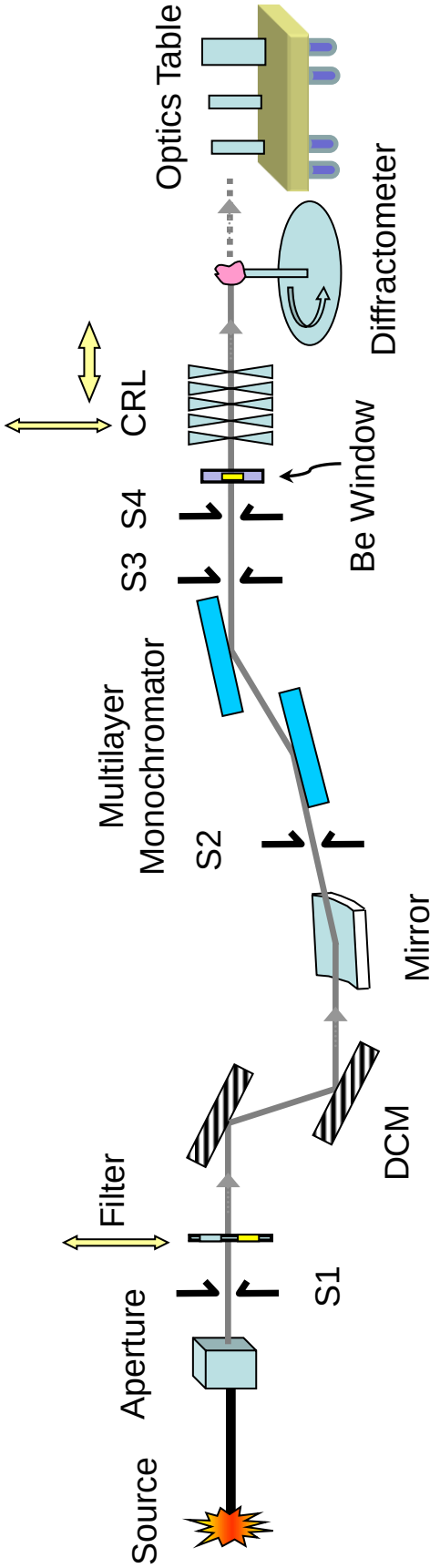

Figure 3.2: The Diamond test beamline B16 layout.

3.2 X-ray optical elements

This chapter provides a brief description of the various optics and elements used to handle synchrotron X-ray beams. Their utility varies from focusing, to maintaining vacuum or select the energy, but they are all introducing wavefront errors. Knowing their principle is essential for beam characterization but also for correction and optimization. Indeed, optics imperfections generate optical or wavefront errors in the working beam that degrade the quality of the sample data collection.

A large number of tables, sometimes biased, comparing the performance of X-ray optical elements can be found in the literature. Yet, the next section only presents the advantages of each optics. No attempt will be made to compare their performance. The purpose of this thesis is to measure optics for metrology purpose and, in this endeavor, their parameters were more important than their relative performance. Hence, only a brief description of the basic working principles of several kinds of optics is provided in the next sections.

The parameters used to describe the goodness of a focusing optics is usually the focal spot size and the irradiance gain.

3.2.1 Mirror

For X-ray mirrors to be efficient, they operate under total reflection, for instance at grazing incidence on a heavy metal, or at higher angle from the bandwidth produced by a multilayer coating alternating layers exhibiting a density contrast between them. Mirrors are achromatic optics presenting usually a large aperture while bent mirrors can have a short focusing distance. The most common application of mirrors is focusing; such optics have experimentally demonstrated their ability to reach the diffraction limit [29] whilst also offering a good efficiency.

The optimal shape of a focusing mirror is described by the ellipse having as foci the source and the focal point. A more complete mathematical description of the shape, slope and curvature of an elliptical focusing mirror is given in appendix B. The general equation of optics also applies for X-ray mirror and becomes:

$$\frac{1}{q} + \frac{1}{p} = \frac{1}{f} = \frac{2\sin\Theta}{R} \tag{3.1}$$

In this equation, p is the distance from the mirror center to the object, q the the one to the image, f is the focal distance, Θ the grazing incidence angle and R the mirror radius of curvature.

Figure 3.3 shows the two kinds of errors that affect the X-ray mirror performance. The surface roughness corresponds to the high spatial frequency errors from the perfect mathematical shape. They generate diffused scattered light that spreads the energy around the specularly reflected beam. Surface roughness can be characterized with Atomic Force microscopy or by grazing incidence X-ray scattering methods [1].

Errors over longer spatial periods are considered as shape errors (cf. Fig. 3.3.(b)). The mirror figure profile deviations from the perfect elliptical shape create focusing errors arising from the wavefront aberrations induced upon mirror reflection. The thesis work carried out at BM05 on the Ion Beam Figuring of mirrors was restricted to the measurement and correction of these kinds of errors.

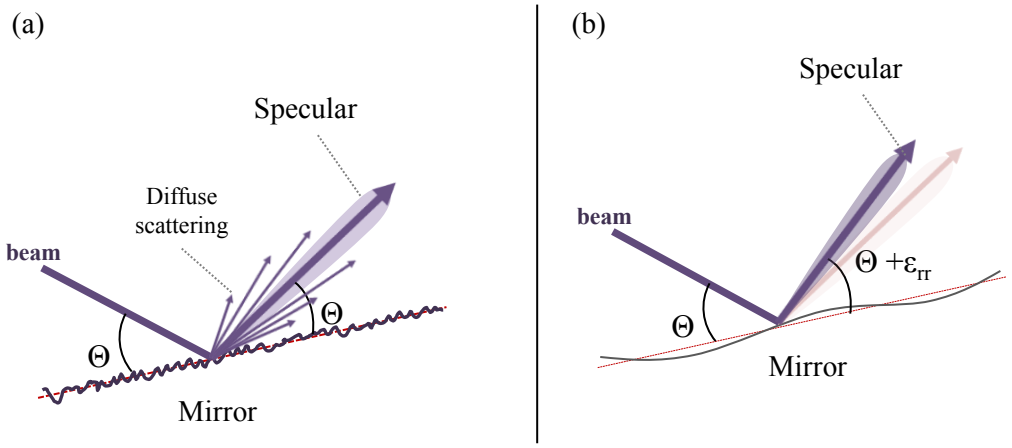

Figure 3.3: Factors of mirror performance degradations. (a) Micro roughness corresponds to deviations from the perfect ellipse at high spatial frequency. These errors are responsible for the diffuse scattering that reflects photons outside the desired specular direction. (b) Slope error corresponds to the long spatial periods that create focusing errors and optical aberrations

3.2.2 Compound Refractive Lens

As seen in Sec. 2.3, X-rays interact weakly with matter, the optical refractive index δ being very small and moreover $n < 1$. For these reasons, the design of X-ray converging lenses is unconventional when compared to visible ones. The lenses used with X-rays are transmission refractive systems. Contrary to visible light optics, a higher convergence is here obtained by increasing the thickness. Hence a X-ray Compound

Refractive Lens (CRL) is thinner on its axis and thicker on its edges. Because the effect of X-ray refraction is weak, a series of lenses must be stacked together to obtain a workable focal length [30]. Beryllium is usually the material of choice to produce CRLs as its low absorption enables the serial accumulation of many lenses whilst limiting intensity losses [31]. Nevertheless, as more lenses are stacked together, the effective aperture of the CRLs diminishes, sometimes making the transmitted photon flux become an issue. Synchrotron users appreciate the CRL for its ease of alignment (on-axis element). As the index of refraction depends on the energy ($\propto \lambda^2$), the X-ray refractive lens is a chromatic system.

The optimal focusing shape of a lens is an ellipse [32] that can be approximated in the apex region by a parabola (see Fig. 3.4):

$$y = \frac{x^2}{2R} = \frac{x^2}{2f\delta} \tag{3.2}$$

where R is the lens radius of curvature at the apex. When using a stack of 2N lenses, the focal length can be calculated using the relation:

$$f_{2N} = \frac{R}{2N\delta} \tag{3.3}$$

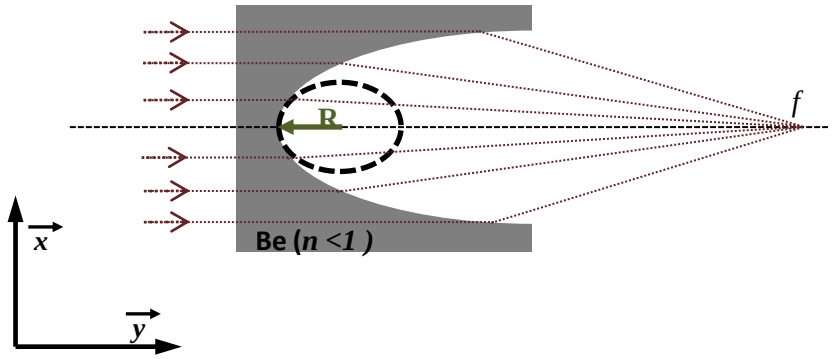

Figure 3.4: Single compound refractive lens geometry.

3.2.3 Fresnel Zone Plate

Fresnel Zone Plates are diffractive optics available in the visible domain since a long time [33] and adapted to the hard X-ray regime a decade ago when they demonstrated

good performance and efficiency at moderate energy (< 10 keV)) [34].

The Zone Plate principle is shown in Fig. 3.5: the light is concentrated in a focal point by means of concentric diffracting rings whose widths are arranged so that the rays that may pass trough the lens reach the focal point with the same phase (constructive interference). In addition to the FZP lens itself, a central stop placed on the optical axis stops the part of the beam which has not interfered with the lens (*zeroth* order) and an order sorter aperture is placed few millimeters upstream the focus to select the desired diffraction order. The smallest focal size achievable with FZP is imposed by the narrowest ring width producible. FZPs are often made with electron beam lithography technology permitting nowadays an outermost zone of ~ 20 nm.

The definition parameters of a FZP are usually the size of its narrowest ring Δr_n and its diameter D. From these parameters, one can derive the focal length for a given wavelength λ (chromatic optics):

$$f = \frac{\Delta r_n D}{\lambda} \tag{3.4}$$

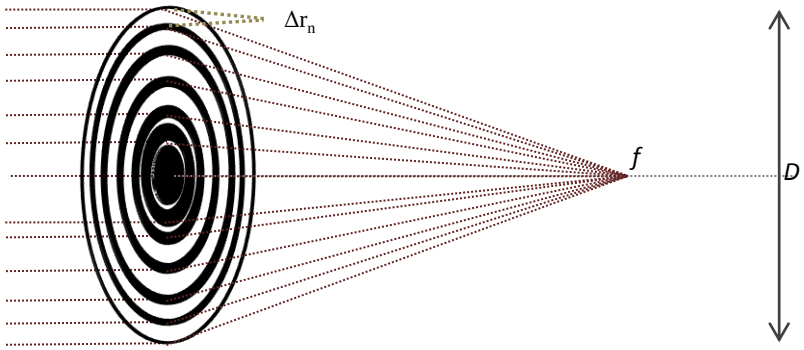

Figure 3.5: Fresnel Zone Plate principle: the incident rays are diffracted by the concentric rings with radius $r_n = \sqrt{n\lambda f}$. Thus, only the X-rays that present the same phase (up to a factor $n\lambda/2$) may reach the focal point.

3.2.4 Monochromator

The energy tunability is one major advantage of synchrotron sources. To select a particular photon energy from the large spectrum band delivered, monochromators are employed in the hard X-ray regime. Monochromaticity can be expressed in term of wavelength or energy bandwidth: $\Delta\lambda/\lambda$ or $\Delta E/E$.

The first kind of monochromator uses the Bragg diffraction from high quality crystals [35] (Fig. 3.6.(a)). These monochromators are often composed of pair of parallel crystals cooled with liquid nitrogen or water to maintain the direction of the incident beam (useful when using a long beamline). The typical bandwidth of a Si(111) monochromator, such as the ones used at ESRF and Diamond, is about $\Delta E/E \sim 10^{-4}$, which corresponds to a longitudinal coherence of $\sim 1\mu$m, calculated using the relation: $\lambda^2/\Delta\lambda$. In the case of the DLS B16 and the ESRF BM05, Bragg diffraction is obtained by reflection on the Si crystals. At higher energies (> 45 keV), when the absorption becomes weak, it is common to use Laue diffraction (transmission through the crystal) to limit the size of the crystals.

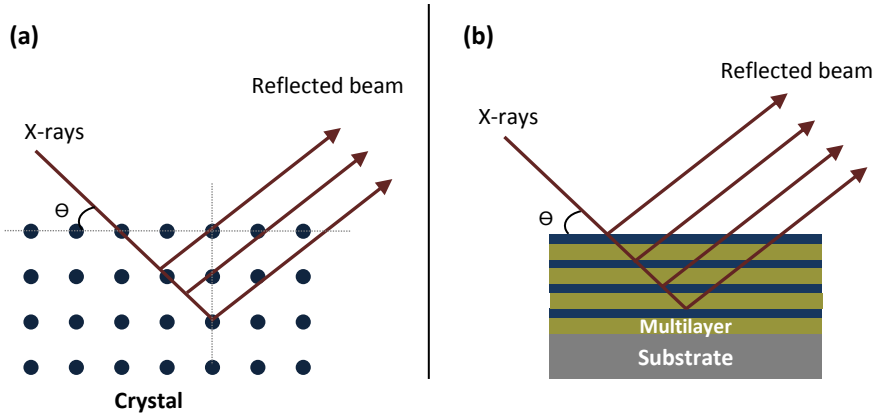

Figure 3.6: Monochromator operating in the kinematical approximation. (a) In a crystal based monochromator, the X-ray energy is selected according to Bragg's law. (b) In a multilayer monochromator, each high-density layer diffracts the X-rays, coherently for a specific energy according to a corrected Bragg's law.

The second kind of monochromator takes advantages of layers stacked with alternative density by deposition on a substrate [36, 37]; their effect is equivalent to Bragg reflectors with an intrinsic bandwidth 100 times wider as compared to a perfect crystal (Fig. 3.6.(b)). Typical multilayer monochromators such as the ones available at ESRF BM05 and Diamond B16 are produced by alternative sputtering of Ruthenium and Boron carbide layers $[Ru/B_4C]_{70}$ to act as a one-dimensional synthetic crystal. Each individual layer is a few nanometer thick. As for a crystal monochromator, a multilayer monochromator is usually made of a pair of reflective elements, each one being cooled.

The bandwidth of a multilayer monochromator ($\Delta E/E \approx 2\%$) being two orders of magnitude larger than the one of a Si(111) monochromator, the reflected flux is also increased by the same amount. When the energy selectivity was a crucial parameter, for instance when using a FZP or CRLs, the double crystal monochromator was chosen. Conversely, when flux was the main issue, the multilayer monochromator was given

favor.

For both kinds of monochromators, all surface and bulk imperfections are leading to wavefront and coherence damage upon double reflection of the beam. Additionally, the heat accumulated through photon absorption can, despite the cooling system, be an important cause of material distortion and wavefront aberration. Furthermore, when using a multilayer monochromator, the higher angle of operation as compared to total reflection makes the reflection more sensitive to the mirror substrate imperfections, thus generating phase errors resulting in contrast fringes.

3.2.5 Other optics

Among other focusing optics, one can mention kinoform lenses made from clever etching design to diminish the absorption in the optics without degrading its focusing performance [38]. Similarly, silicon or diamond compound refractive lenses can be produced from a single wafer with XUV lithography. None of these optics were employed or characterized because of their small aperture (< 50 μm) and the ultra brilliant source they require for getting a workable flux.

Although usually not considered as optical elements, windows located along the beam path act as dephasors that damage the wavefront. At third generation synchrotrons, windows transparent to x rays are used to maintain part of a beamline under vacuum or Helium and are made of Beryllium or Carbon. Despite the careful attention given to their polishing quality, in-depth defects still lead to the creation of optical aberrations and beam coherence degradation [39].

3.3 X-ray detectors

Two kinds of detectors for X-rays are distinguishable: integrating and counting detectors. One can find a deeper interpretation of these differences and their implications for the X-ray signal measurements in Ref. [7]. For most of our experiments, 2D high spatial resolution was the determinant requirement. CCD based imaging detectors coupled to scintillator and microscope optics were our choice detector.

CCD detector

Charge-coupled devices (CCD) are two dimensional integrator devices and the ones used with x-rays are not different. For X-rays, instead of direct illumination, these chips are coupled to a thin scintillator that converts the X-ray intensity into visible light, recorded then through the magnification of a visible microscope optics by the CCD.

At the ESRF, the traditionally employed CCD based detector is the FReLoN [40] (Fast Read out Low Noise) camera which has a chip with a 15 μm pixel size. It is used in combination with one of two different Peter optics and eye pieces. One optical system results in an effective pixel size of 5.8 μm while the second one is a microscope optics providing an effective pixel size of $\sim$ 0.8 μm. Despite the low efficiency provided by such system (indirect detection), the FReLoN camera was selected and appreciated for its low noise level and its then good electronics signal to noise ratio.

At Diamond light source, the choice of a CCD detector is offered between two cameras: an X-ray eye with a 6.4 μm pixel size or a PCO 4000 [41] camera, coupled to switchable Peter optics that provide different effective pixels size ranging from 0.18 μm to 1.8 μm.

Because of the CCD technology, these camera have to be used in combination with a shutter to avoid artifacts occurring when the chip is simultaneously collecting light and reading the electronic levels. Since visible optics is employed to obtain high magnification, such camera is not free from optical aberrations: the recorded images present distortions that can, and in some case must, be compensated for.

Diodes

Silicon diodes are employed at synchrotrons as current detectors : electrons excited within the Si crystal by the X-rays are ejected from their relaxed position to the continuum medium, creating a measurable pico Ampere order current, proportional to the X-ray photon flux.

One common use of such detector for online metrology is its combination with an absorbing object edge. Such experimental set up is often called knife edge technique. It consists of scanning an absorbing edge across the focal point of an optical system

to infer the beam width.

Others

Pixel detectors are more recent 2D photon-counting detectors that provide very large dynamics, although offering quite large pixels (~ 50 μm). These detectors are already widely used for either large field of view imaging, far field imaging or reflectivity experiments where dynamics and sensitivity are the most relevant parameters. However, in the course of this project, the limited spatial resolution they offer prevented their use.

It is worth mentioning several other kinds of X-ray detectors including gas detectors and scintillator-based system. Yet, apart from some alignment works, such detectors have rarely been used during this project.

3.4 Metrology laboratories

Modern synchrotrons are nowadays usually equipped with metrology laboratories dedicated to the characterization of reflective optics. They use a clean room environment with good temperature stability. As presented in Sec. 3.2.1, factors affecting the performance of mirrors are roughness and shape errors. Therefore, a metrology lab is usually equipped with instruments permitting the measurement of both. For the roughness characterization of a mirror surface polished for X-ray applications, devices such as Atomic Force Microscope (AFM) and micro-interferometers are employed. For characterizing the mirror shape, two main classes of dedicated devices are employed: Long Trace Profiler (LTP) or Nanometer Optical Measuring machine (NOM) and visible light interferometers. They all permit the characterization of slope and shape errors of planar or curved mirrors over spatial frequencies ranging from 1 mm^{-1} to 1 m^{-1}.

Visible light metrology tools, that benefit from several decades of development, are nowadays able to achieve sub-nanometer accuracy. Thus, data obtained from metrology labs were often used for comparison and validation of the at-wavelength developed methods. Nevertheless, this comparison finds its limits, especially at the sub micro-radian range accuracy, when the off-line optical characterization measurements cannot be made under real working conditions. That includes for instance a bulky optical

support or a thermal load condition that cannot be simulated within the clean room environment of an optical laboratory.

Surface profilometers

LTP and NOM are widespread instruments that can measure surface slopes in one direction with sub nanometer accuracy. The instruments have found interest in the X-ray community because meter long mirrors, even with an aspherical shape, can be characterized with a sub-microradian sensitivity and without employing any stitching process.

As shown in Fig. 3.7, a LTP system uses a pencil beam interferometer to measure the surface slope profile. Thanks to prisms, two sets of pencil beam pairs are created to shed light on the test surface and the instrument reference surface. While the two beams within a pair interfere with each other, the two pairs of beams do not interfere with each other. The reference flat is used to compensate for mechanical errors. The position changes of the beams falling onto a linear array detector permit to calculate the angular deviation of the light caused by the test surface. Further, an integration allows the reconstruction of the surface shape from the measured slope profile. Since the LTP probe beams are generated by visible laser light, the spatial resolution of the instrument is limited to a few millimeters.

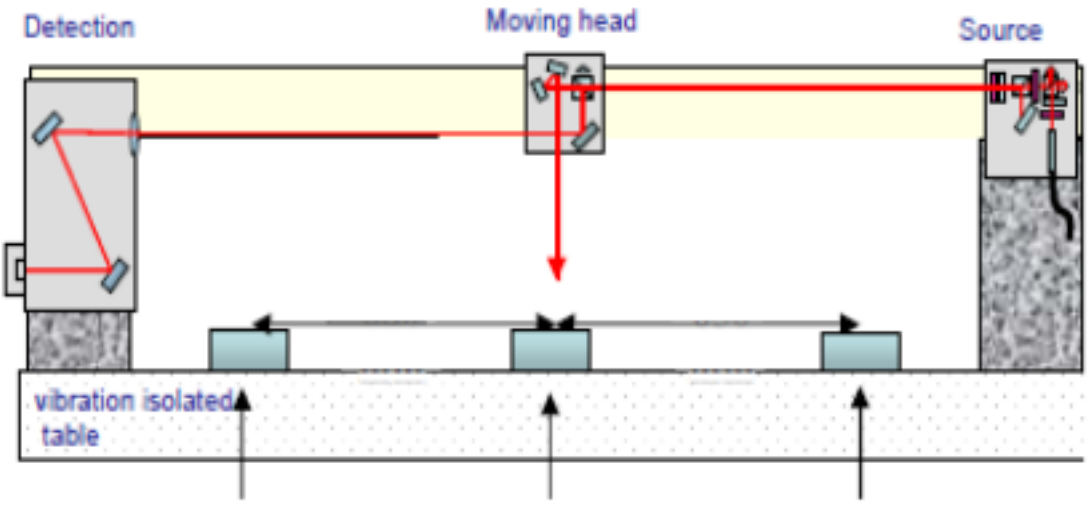

Figure 3.7: Schematic of the ESRF LTP

A NOM, as shown for instance in Fig. 3.8, has a slightly different concept: it uses a pentaprism located in the moving head. A collimated beam produced by a LED source and narrowed by slits is deflected perpendicularly by the scanning pentaprism, reflected from the surface under test and deflected again by the pentaprism towards an objective. The light recorded on a two dimensional CCD detector is used to recover the surface slope by monitoring the lateral displacement of the slit image on the CCD array.

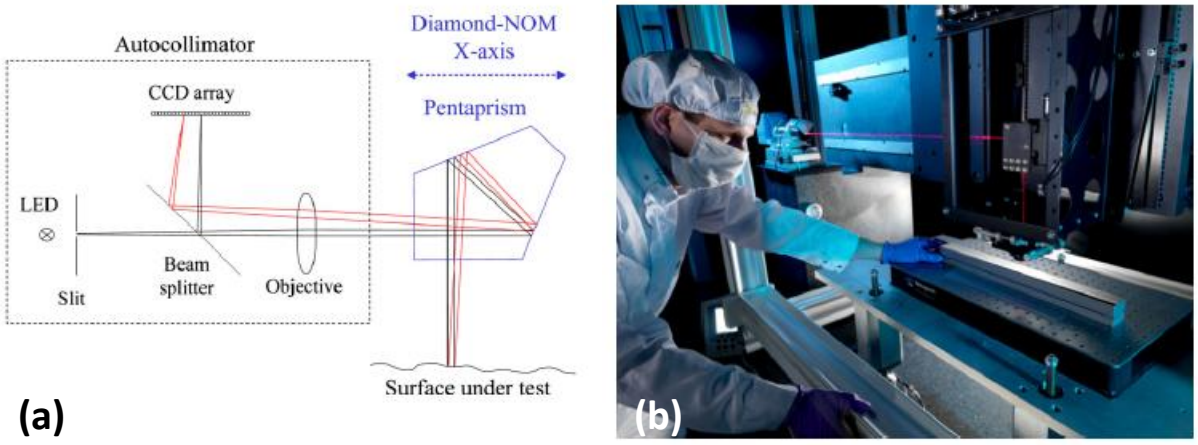

Figure 3.8: (a) Schematic of the Diamond NOM (cf. Ref. [42]) (b) Operator of the Diamond NOM in the clean room metrology lab.

The ESRF LTP [43] is a custom built instrument that has a precision on the slope error better than 0.2 μrad rms. The Diamond NOM, also a custom built instrument, provides sub-nanometer accuracy on mirror shape for mirrors up to 1.5 m in length [42].

Interferometers

Interferometers employed to measure optical shapes are usually of the Fizeau type. This arrangement uses a transmission reference object to create interferences, from which information on the shape difference between the test object and the reference are obtained [44]. Fizeau interferometers have the advantage of an light optical path identical for the test and reference beams, apart from the beam splitting surface of the transmission object. When measuring curved surfaces, it is necessary to tune the reference beam of the interferometer by substituting a spherical transmission to the flat transmission. This operation is required to compensate for the effect of probe beam decollimation induced by the surface under test. Because the number of transmission

spheres available to optimize the measurement is limited, Fizeau interferometers show limitations for measuring strongly focusing X-ray optics.

Fizeau interferometers provide a typical accuracy of a few nanometers over a 100 mm long surface. For larger optics, stitching methods are employed to recover the shape of the mirror over its full length. When measuring X-ray mirrors, these interferometers are appreciated over LTPs/NOMs because of the two dimensional map of the surface they provide instead of a one dimensional slope.

4 X-ray phase sensing techniques

4.1 Introduction

As exposed in the introduction, synchrotron beamline optics must keep pace with the remarkable advances in source technology, to constantly improve the optical surface quality. Every endeavor to measure and compensate for optical defects at the tolerance scale defined by the wavelength of operation is needed to avoid brightness and coherence losses along the synchrotron beamlines. Indeed, accurate surface metrology and in situ alignment are nowadays limiting the development of nanofocusing optics. To manufacture X-ray mirrors that preserve the beam coherence and the wavefront shape, it is important to benefit from metrology methods capable of assessing the surface quality in X-ray terms and under working conditions. Taking a deeper look into the measurements being performed, the needs can be different from beamline to beamline. Stringent requirements are encountered on beamline exploiting the coherence or focusing the beam to a nanometer size, wherein sub-micro radian measurement accuracy is necessary.

Yet, the wavelength of hard x rays, at the Angström (0.1 nm) level, can also be an asset. With such a short wavelength, the diffraction limit imposed by the probing light is much smaller than the one of visible light instruments. Theoretically, the mirror shape characterization at high spatial frequency using X-ray-based methods is expected to be superior to that of the traditional instruments presented in the previous chapter [9].

At-wavelength metrology is today regarded as a corner stone toward the achievement of diffraction limited X-ray optics. While several in-situ at-wavelength methods are already available and used at synchrotrons a number of them are still at an early development stage. Some specifications of X-ray mirrors with diffraction limited fo-

cusing performance are displayed in Table 4.1 [45]. These figures illustrate the level of requirements put on the metrology measurement accuracy. One must be able to sense a figure error smaller than 1 nm on the surface height and 0.1 μrad on the surface slope with a spatial wavelength shorter than 1 mm. Concerning roughness, the metrology must be able to assess Angström order inhomogeneity of the surface for spatial frequencies as high as 1/20 $n\text{m}^{-1}$.

Error category	Specification	Spatial Wavelength
Height Error	$\leq$ 2.0 nm rms	1 mm - 1 m
Slope Error	$\leq$ 0.25 μrad rms	1 mm - 1 m
Mid-Spatial Roughness	$\leq$ 0.2 nm rms	2 μm - 1 mm
High-Spatial Roughness	$\leq$ 0.4 nm rms	20 nm - 2 μm

Table 4.1: Surface specifications for X-ray mirrors.

Whilst X-ray characterization methods of optical surface roughness such as X-ray diffuse scattering are already mature [1, 46], some others for the measurement of the longer spatial wavelengths for figure error assessment and for beam phase sensing were limited for years to simplistic schemes, like the pencil beam technique [47, 48]. More advanced schemes and techniques started to be developed only less than ten years ago with new instruments such as the Hartmann sensor and the grating interferometer. In parallel, phase sensing has seen its interest growing exponentially with a large spread due to applications in phase contrast imaging.

Phase sensing is often performed measuring the wavefront $W(x, y, z)$, the surface defined by points of the beam having a constant phase $\phi(W) = cst$. As a matter of fact, the wavefront contains information on both the propagation direction of the light and the optical delay between rays. Several techniques have been developed to measure the wavefront and recover the beam phase. We describe briefly below the different kinds of phase sensitive techniques available in the X-ray regime.

4.2 Method categories

Scanning vs full field techniques

For instrumentation reasons, scanning methods were the first to be implemented and routinely used. X-ray microscopy was highly promoted around 1948 with the emergence of the mirror setup conceived by Kirkpatrick and Baez [49]. By concentrating

the photons into a narrow point and scanning an object across it, one can measure for each step the absorption and fluorescence signals, and then generate maps of the sample properties. Conversely, full-field imaging microscope renders simultaneously the information for all points or detector pixels. Its realization is done by placing the sample either upstream the focusing optics to benefit from an optimal depth of focus, or, few millimeters downstream the focal point to benefit from a large magnification factor. In full-field imaging techniques, two dimensional imaging detectors are employed as in traditional visible photography.

Despite offering the advantage of mapping both the absorption and the fluorescence signals from a sample, scanning techniques are limited by the X-ray optics focusing performance and require as many exposures of the sample as the number of points in the constructed map. Today, although X-ray scanning microscopes are still widely used, new methods put a strong emphasis on schemes that are tomography compatible and dose efficient by reducing the amount of sample exposures thus giving preference to full-field approaches.

Far-field vs near field techniques

In section 2.4, two different descriptions of light propagation were introduced. Each one holds for respectively short or long distances from the diffracting aperture.

An imaging technique operating in the near field is also called a real space method: images used within these methods mirror directly the illuminated object. Conversely, far field methods, or reciprocal space methods, record intensities corresponding to the square modulus of the sample Fourier transformed scattering function. Far field techniques have demonstrated the potential to image samples with a spatial resolution as high as a single nanometer. Coherent diffraction imaging is the most widespread far field imaging technique nowadays [50, 51, 52] but one can also mention ptychography [11, 53]. This last method is actually a hybrid one using simultaneously real and reciprocal space information. Far field techniques present the advantage to not require any specific optics but, on the other hand, have severe requirements on beam brilliance and coherence, fulfilled with the arrival of new X-FEL instruments, to reach their full potential.

Because no far field technique were used during this project no further description of

the coherent diffractive imaging and ptychography techniques will be given.

All techniques presented in the following parts of the manuscript fall into the near field category; the detector is located at a distance $z << D^2/\lambda$ where D is the characteristic beam aperture. With D of the order of 1 mm, any positioning of the detector within the few meters downstream the aperture is considered as near field. In the techniques presented, the signals of both the transmitted and scattered parts of the beam are recorded, in contrast to far field methods where the direct beam is rejected and only the scattered part with large scattering wave-vectors is used.

Deflection vs propagation methods

Phase sensing technique are either sensitive to the first or second derivatives of the beam wavefront: no direct measurement of the beam phase is possible. Propagation techniques (cf. 4.3.2) are sensitive to the Laplacian of the wavefront ΔW while deflection techniques measure its gradient ∇W. This makes deflection methods generally better suited to homogenous samples with a slowly varying optical index, wherein no sharp edges are present, whilst propagation methods can achieve high spatial resolution.

4.3 Available techniques

4.3.1 Crystal interferometry

The crystal interferometer was the first phase instrument proposed in the X-ray regime [54]. This device is directly inspired and is fully equivalent to the one used within the visible domain. Its principle is indeed the same: the beam is split into two branches thanks to single crystals and the separated beams propagate over an equal distance before interfering further in a plane downstream where a detector is positioned. The investigated sample is placed in one of the branches and the analysis of the interference pattern distortions from the reference one permits the recovery of the sample phase shift [9]. Such interferometer has been used for tomography [55] and showed interesting possibilities for soft tissue imaging. Nevertheless, the device has severe mechanical stability requirements that get even stronger when increasing the energy to investigate

thicker samples.

4.3.2 Propagation-based imaging

TIE and CTF based methods

Transport of Intensity Equation (TIE) based and Contrast Transfer Function (CFT) methods are two slightly different online propagation phase contrast imaging methods. These techniques are sensitive to the Laplacian of the wavefront, i.e. the wavefront second derivative. The setup does not require any optical element, only a detector placed at a short distance from the sample (near field): the recorded interferences resulting from sample edges diffraction are then used to reconstruct the full phase map of the sample [56, 57]. These techniques usually require the taking of images of the sample at different distances in order to record all spatial frequencies because of the Talbot effect [23]. However, under certain conditions and using specific algorithms, one can perform phase imaging from images recorded at a single distance [58, 59]. Langer *et al.* [60] have studied in details the difference between the TIE and CFT approaches, that are otherwise, similar in many aspects.

Analyzer-based imaging

Phase contrast imaging using the techniques of the previous section can be enhanced by the use of a crystal to study samples that are either homogeneous or present only a small phase shift. In this technique, a highly selecting crystal is oriented in such a way that the incident X-ray beam is reflected using the side (highest slope) of the crystal Darwin curve: the small deviation of the rays in the sample is thus translated into a variation of diffracted intensity. This method was demonstrated successful in the study of biological samples where natural phase contrast is small [61].

4.3.3 Deflection-based phase sensing technique

Pencil beam technique

The pencil beam was the first and probably still the most used phase sensing technique within synchrotrons [47, 48]. Despite being at first sight a bit crude, this technique was shown to be very efficient and easy to implement. The method requires a simple setup and works with incoherent light, making it usable on any beamline with a minimum of instrumentation. The technique consists of sequentially and spatially sampling the X-ray beam using a pair of slits. Looking at where the different generated beamlets fall on an imaging detector, one can retrieve the propagation direction of the photons at each point, which is also in optics the beam wavefront gradient. This technique is nowadays spread worldwide on beamlines to perform routine online metrology and alignment work.

Hartmann sensors

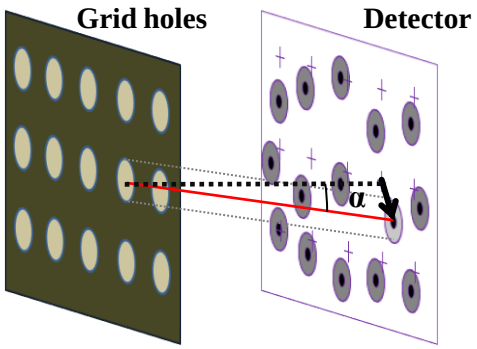

Figure 4.2: A Hartmann sensor: the beam is sampled with a grid of holes that permit to calculate the trajectory of the beam for each aperture position.

X-ray Hartmann [62, 63] sensors are directly inspired and adapted from the visible domain where such instruments have found great interest in adaptive optics. The instrument is equivalent in principle to the pencil beam technique: in a Hartmann sensor, all beamlets are created and analyzed simultaneously thanks to an absorbing grid replacing the scanning of a pair of slits. An X-ray mask with holes is placed in front of an imaging detector and, from previous calibrations, one can calculate the deviation of each beamlet from its expected position. This way, the propagation direction of the photons can be known for each grid hole position, and the beam phase reconstructed. This device is regarded with high interest within X-FEL facilities because it permits the wavefront error calculation from each image generated by each independent pulse.

However at synchrotrons, the instrument is a bit less attractive as the spatial resolution is limited by the spacing of the grid holes and the calibration can be tedious.

Coded apertures

Coded apertures can be seen as a specific combination of grating-detector. First developed for laboratory sources, the instrument works with incoherent illumination as no optical interference is used. The coded aperture technique uses two absorption gratings to sort out and detect the photons that are deviated by the sample [64, 65]: the recorded signal corresponds to the refracted part of the beam, i.e the wavefront gradient. At the early stage of development, the instrument was sensitive to the refraction in only one dimension. The progress of the instrument has permitted to overcome this limitation and refraction can now be measured simultaneously in the two orthogonal directions.

Grating interferometry

The grating interferometer was introduced in the hard X-ray regime ten years ago [66, 67] and the first experiments of such devices were conducted in parallel at the ESRF beamline BM05 and Spring-8 in Japan. It offers several advantages, among which a fine sensitivity and low requirements on coherence and mechanical stability. Being one important topic of this thesis, the method will be described in more details in the next chapter.

4.4 Development matters

When developing a new imaging technique and beyond the never ending search for higher sensitivity and better resolution, several parameters can be taken into account when working with X-rays, as developed below.

As already stated, one important aspect when setting up a new X-ray technique is to find a versatile one, i.e. that applies to a large number of applications, and preferably not restricted to, e.g., the case of the synchrotron source. Indeed, as most X-ray

laboratory sources are tube-based technology with a large emittance, one challenge is to find the technique or instrument that is tolerant with their larger source size and divergence compared to synchrotron source, as well as with the lower brilliance. That means the technique should not have strong requirements on longitudinal and transverse coherence in addition to be photon efficient. Grating interferometry and coded aperture are for instance two success stories of techniques ported from synchrotron to laboratory sources [68, 65].

Another point of interest for a new X-ray method is its applicability in the new X-FEL facilities, under construction or under commissioning worldwide. These new instruments aim at investigating, among other phenomena, the very short time scale domain or the imaging of non crystalline matter. In that endeavor, techniques able to bring information about the sample from a single X-ray pulse are regarded with the greatest interest. Indeed, 'beams' delivered by an X-FEL source consist of very intense short ($\sim$ fs) independent pulses that are expected to accumulate information about samples, that are even, in some experiments, destroyed by the traversing of the intense X-ray pulse itself [69]. Hence, each recorded pulse is unique from its generation and for the information collected when passing through the sample: that forces the data analysis to be done and corrected independently for each pulse before employing further statistical interpretation tools.

The last important point for biological imaging is the dose or number of photons absorbed by the sample exposed to X-rays. Although the topic receives little mention in this manuscript, the reader should be aware that important ongoing works are performed worldwide in an attempt to reduce the dose delivered to the sample when imaging it, especially for medical purpose [70].

Part II

Development of Methods

5 Grating interferometry

Since the inception of this project, the X-ray grating interferometer was regarded as a very promising candidate to perform online metrology. Previous work [71] already showed the potential of the device for metrology, that since, was employed at many synchrotron beamlines worldwide and more recently at the X-FEL [72]. The device was shown to be very stable mechanically whilst also benefiting from the maturity of the numerical processing methods imported from visible light interferometry [73, 74]. Nevertheless, further developments were still necessary for routine optics characterization.

In this chapter, the investigations carried out on X-ray grating interferometers (XGI) will be presented. In the frame of the metrology project, the core of the research was dedicated to the study of the sensitivity and spatial resolution of the device. The next sections will present the XGI working principles and the results of our investigations.

5.1 Principles

The X-ray grating interferometer is a device imported from the visible light domain [75, 76, 77] that became operable in the X-ray regime thanks to the successful production of X-ray gratings.

An X-ray grating interferometer (see Fig. 5.1) consists of two gratings and an imaging detector: the first grating, noted G_1, is a phase grating and the second one, noted G_2, is an absorption grating. The first one is used to split the beam in different directions corresponding to the grating diffraction orders, mainly the 0^{th} and +/-1^{st} orders. Then, these different beams interfere downstream creating a fringe pattern. The distortion of this pattern from a perfect one permits the recovery of the phase

distortion present in the incoming beam. According to the Talbot effect described in Sec. 2.4.3, the interferences of G1 are only visible at specific distances. Thus, the optimization of the signal to noise ratio of the data collected imposes to place the second grating at a distance corresponding to a maximum of fringe visibility of the interferences, *aka* Talbot distance.

Two kinds of interferometer are now available: the most wide spread is the 1D interferometer composed of gratings made of parallels lines, and since more recently, the two dimensional grating interferometer designed with two dimensional patterns [78]. Their operating principle however remains equivalent in concept.

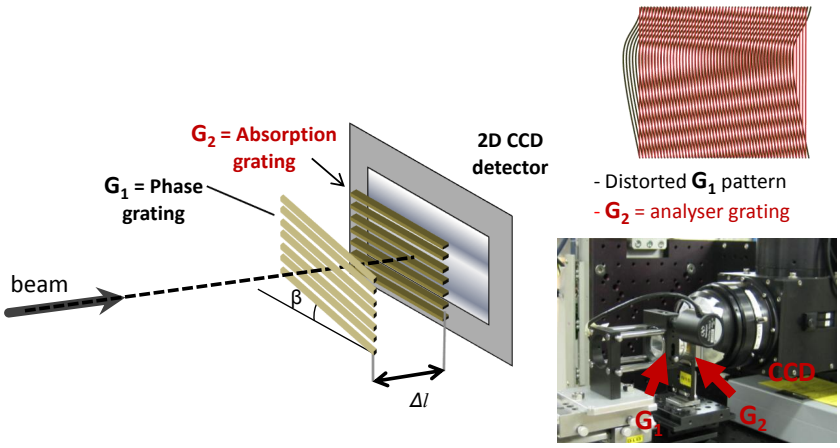

Figure 5.1: A 1D X-ray grating interferometer: a phase grating and an absorption grating with matching pitch are placed in front of an imaging detector at a distance Δl. The superposition of the small fringes created by the two gratings give rise to larger ones.

Depending on the relative angle β between the two gratings around the beam axis, interferometers can be used in two distinct modes. When the angle is set to $\beta = 0$, the interferometer is used in the so called phase stepping mode. Within this processing method, the two gratings are perfectly aligned generating a null fringe, i.e with no visible Moiré fringes, by aliasing of the two fringes periods. In this mode, several images are necessary for each projection phase recovery as it will be described in Sec. 5.3.

Conversely, when one grating is slightly rotated relatively to the other, i.e. $\beta \neq 0$, some Moiré fringes become visible in the recorded images. A Fourier analysis of the pattern permits the beam phase recovery for each single image, but sometimes at the cost of phase retrieval artifacts. This second processing method will be discussed in Sec. 5.4.

5.2 The gratings

X-ray gratings are nowadays produced by XUV lithography or white light laser on thin silicon or tungsten substrates or by electron beam writing followed by a wet etching process. One can find X-ray gratings with pitch ranging from 2 μm to more than tens of microns. Absorption gratings are produced the same way as phase gratings but have in addition their grooves filled with a heavy material using electroplating [79, 80].

The interference contrast of a grating depends on the phase shift it introduces and its duty cycle [81]. A complete description of the grating diffraction efficiency is provided in Ref. [82]. The Fresnel diffraction patterns obtained with gratings have been deeply investigated and described [83, 21]. The optimization of the signal to noise ratio obtained with a grating interferometer is achieved by maximizing the contrast of the Talbot pattern [19].

With a minimal grating substrate thickness of 50 μm, the double traditional grating arrangement can show significant absorption when working at low or moderate energy ($E \leq 8$ kEV). While the integration time can be increased to avoid the interference signal to noise ratio level, it is achieved at the cost of a greater dose for the sample. Setups with only one grating have been presented to avoid this drawback of particular importance when analyzing biological tissue [84].

Conversely, at higher energy, the efficiency of the grating can fall due to the weaker interaction of X-rays with matter. This creates a demand for gratings with very high aspect ratio capable of generating π or $\pi/2$ phase shift on highly energetic photons, such as the one employed for human body imaging [85]. An alternative approach has been attempted replacing the couple absorption grating/scintillator by a structured scintillator [86].

5.3 The phase stepping mode

Phase stepping is a wide spread category of methods within interferometry [87] consisting of taking several images while varying the phase of the beam interference from one image to the next by a known amount. Schemes with 3, 4, 5 and then n images were developed, bringing each time more accuracy and better robustness to noise and

shift miscalibrations [88].

For XGI metrology, the technique and algorithm employed during the project was the one described in Ref. [89]. It consists of scanning a grating by translating it over a distance of an integer number of grating periods and taking an image at each regular position. The phase is then extracted using a Fourier transform of the signal seen and recorded separately within every detector pixel during the scan. The motion of the scanned grating is obtained using a piezo stage permitting nanometer accuracy of the grating positioning.

In this mode, the gratings are oriented exactly parallel to each other and have pitches such that, when illuminated with the reference beam, the generated Moiré fringes have an infinite period, i.e close to the null fringe.

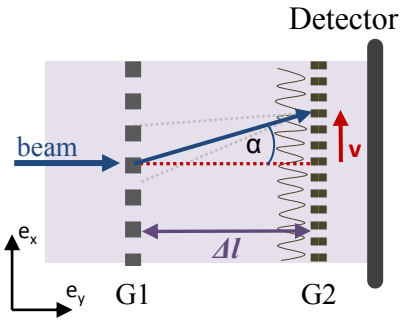

Figure 5.2: The deflection angle in the grating interferometer. The wavefront gradient of the beam translates into a deviation of the interference created by G1 and then into a modification of the flat pattern.

The recovery of the phase shift introduced by the presence of a sample is done using the mathematical derivation presented below. We denote Δl the intergrating distance, p_1 the pitch of the first grating, p_2 the one of the second grating, φ the phase of the beam, λ the wavelength and Φ the fringe phase extracted from a scan using the phase shifting method. Considering the projection of the problem on a basis $(\mathbf{e_x}, \mathbf{e_y})$ as sketched in Fig. 5.2, we have:

$$\alpha(x) = \frac{|\mathbf{v_x}(x)|}{\Delta l} = \frac{1}{\Delta l}\frac{\Phi_x}{2\pi}.p_2 \tag{5.1}$$

Then using the relation: $\alpha = \nabla W.\mathbf{e_x} = k^{-1}\ \nabla\varphi(x).\mathbf{e_x}$ [90] with k the wavenumber $k = \frac{2\pi}{\lambda}$, one can derive the grating interferometer equation:

$$k^{-1}\nabla\varphi(x).\mathbf{e_x} = \frac{\Phi_x(x)}{2\pi\Delta l}p_2 \tag{5.2}$$

Or:

$$\frac{\partial\varphi(x)}{\partial x} = \frac{p_2}{\lambda}\frac{\Phi(x)}{\Delta l} \tag{5.3}$$

When working differentially, the reference or flat field is removed to isolate the contribution of the incoming beam. For this, the phase Φ_{ref} calculated when no sample is in the beam, is subtracted to the one obtained in presence of the sample:

$$\frac{\partial\varphi(x)}{\partial x} = \frac{p_2}{\lambda}\frac{(\Phi_{sample}(x) - \Phi_{ref}(x))}{\Delta l} \tag{5.4}$$

This last equation is the common relation used in the literature for the description of the X-ray beam phase recovery with the XGI [91, 92, 93, 94, 95]. However, we will see, using two alternative approaches in section 5.6 and then Chapter 7, that Eq. (5.4) is actually an approximation.

As we shall see in Sec. 5.5, because of the tricky phase unwrapping problem, it is particularly important to use gratings with perfectly matching pitches, i.e tuned to the G_1 interference magnification.

The phase stepping mode is nowadays the most used for X-ray grating interferometry imaging and tomography [96, 97, 70].

5.4 The Moiré pattern analysis mode

The 'Moiré fringes' mode is the alternative working scheme to the phase stepping mode. This mode is obtained by setting a small angle β. In this case, Moiré fringes are generated by superposition of the effect of both gratings. When the interferences generated by G_1 in the plane of the second (analyzer) grating G_2 match approximately the pitch of the latter, large resolvable Moiré fringes are created by aliasing [98, 99]. Denoting d_1 the period of the interference created by G_1 in the plane of G_2 having a pitch d_2, the final Moiré fringes will have a period $\frac{|d_1 d_2|}{|d_1 - d_2|}$.

The phase of each image is recovered using a phase retrieval method. In interferometry the Fourier methods [100] are the most employed. Despite some small processing artifacts, the method is fast, easy to implement and quite robust. More sophisticated methods using adapted filter or wavelets can be also employed providing access to bigger calculation resources [101, 102]. Again, the fringe phase extracted from the image will be denoted Φ.

When using Takeda's method [100], one can remove the fringe modulation component by shifting, in the Fourier space, the spectrum peak to the center. This processing simplifies drastically the unwrapping process necessary for reconstructing the continuous phase map (cf. Sec. 5.5).

Because he XGI Moiré mode requires only a single exposure of the sample, this working mode is for instance suitable for the analysis of dynamic samples [103].

Two dimensional mapping of the local radius of curvature

The method to accurately calculate the wavefront curvature from XGI and without previous information on the beam characteristics is detailed in Ref. [99]. Although the mathematical development exposed therein is sufficient to calculate the averaged curvature over one direction, one can show that the mathematical derivation can be easily extended to a two dimensional map. Considering the parameters defined in Fig

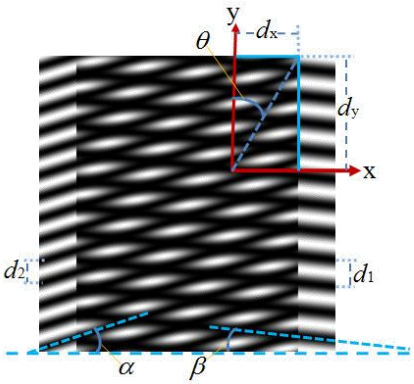

Figure 5.3: Moiré fringes formation from tilted grating.

5.3, the intensity patterns of periods d_1 and d_2 created by respectively by G1 and G2 can be written as:

$$\begin{aligned} I_1 &= a\cos^2\left[\frac{\pi}{d_1}(y\cos\beta + x\sin\beta)\right] = a\cos^2 A \\ I_2 &= b\cos^2\left[\frac{\pi}{d_2}(y\cos\alpha + x\sin\alpha)\right] = a\cos^2 B \end{aligned} \tag{5.5}$$

Using the same method as in [98, 99], the total recorded intensity is:

$$\begin{aligned} I &= I_1 \times I_2 = ab\cos^2 A\cos^2 B \\ &= \frac{ab}{4}\left[1+\frac{\cos(2B+2A)}{2}+\frac{\cos(2B-2A)}{2}+\cos 2B+\cos 2A\right] \end{aligned} \tag{5.6}$$

In this equation, only the third term, denoted I_m, contributes to the large observable Moiré fringes:

$$\begin{aligned} I_m \approx \cos(2B-2A) &= \cos\left[\frac{2\pi}{d_1}(y\cos\beta + x\sin\beta) - \frac{2\pi}{d_2}(y\cos\alpha + x\sin\alpha)\right] \\ &= \cos\left[\frac{2\pi}{d_2}\left((\gamma\cos\beta-\cos\alpha)y-(\sin\alpha-\gamma\sin\beta)x\right)\right] \end{aligned} \tag{5.7}$$

with the period ratio $\gamma = \dfrac{d_2}{d_1}$. The periods of the resolved Moiré fringes in the basis $(\mathbf{x},\mathbf{y})$ are:

$$\begin{aligned} d_{m_x} &= \frac{d_2}{\gamma\sin\beta-\sin\alpha} \\ d_{m_y} &= \frac{d_2}{\cos\alpha-\gamma\cos\beta} \end{aligned} \tag{5.8}$$

Using $d_{m_y} = \tan\Theta.d_{m_x}$, the average inclination Θ of the fringes in an image calculated using the fringe phase, $\tan\Theta = \dfrac{\gamma(x,y)\cos\beta-\cos\alpha}{\sin\alpha-\gamma\sin\beta}$, and combining Eq. 5.8 with 5.7, one can calculate the orientation of the fringes calculated from the recovered phase through the fringes angle Θ_m:

$$\gamma^2 = \left(\frac{d_2}{d_{m_x}}+\sin\alpha\right)^2 + \left(\tan\Theta\frac{d_2}{d_{m_x}}+\cos\alpha\right) \tag{5.9}$$

As explained in Ref. [99], the inclination angles α and β can be retrieved by performing a rotation scan and fitting the extracted values of d_{m_x} to the reorganized equation depending on only one angle:

$$1+\frac{d_2^2}{d_{m_x}^2}(1+\tan\Theta^2)+2\frac{d_2}{d_{m_x}}(\sin\alpha\tan\Theta+\cos\alpha)-\gamma^2=0 \tag{5.10}$$

$$1+\frac{d_2^2}{d_{m_x}^2}(1+\tan\Theta^2)+2\frac{d_2}{d_{m_x}}\left(\cos\beta(\tan^2\Theta-1)\right)-1-\gamma^2=0 \tag{5.11}$$

After the recovery of the angular parameters, one can calculate the $\Theta_m(x,y)$ value for each pixel using the Moiré fringe phase Φ. Considering the surrounding pixels of (k,l), the local fringe orientation is equal to: $\Theta_m(k,l) = \arctan\left(\dfrac{d_{m_x}}{2\pi}\dfrac{\Phi(k,l+1)-\Phi(k,l)}{S_{pix}}\right)$

where S_{pix} is the detector pixel size. When the grating pitches are chosen such that $\gamma(x,y) = 1 + \dfrac{\Delta l}{R(x,y)}$, for instance when $p_1 = 2p_2$ and G_1 is a π-phase shift grating, one can eliminate the γ parameter and derive the beam curvature in the direction perpendicular to the grating lines:

$$\boxed{R_x(x,y) = \frac{\Delta l \cos\beta(1 - \tan\Theta_m(x,y)\tan\beta)}{\tan\Theta_m(x,y)(\sin\alpha - \sin\beta) + (\cos\alpha - \cos\beta)}} \tag{5.12}$$

This equation allows to calculate the beam local curvature at each detector pixel position. When removing the carrier frequency in the Fourier space, the spatial resolution of the technique is limited by the fringe spacing, otherwise it is limited by the shear (cf. Sec. 5.6).

5.5 Phase unwrapping

The problem of phase unwrapping arises whenever a profile is measured with an interferometry system and the fringe phase is extracted using non fringe tracing methods [100]. As the phase recovery methods often use trigonometric (arctan or arccos) functions, the measured angular phase map $\Phi_{2\pi}(x,y)$ produces pixels folded into a $[-\pi : \pi]$ interval:

$$\Phi_{2\pi}(x,y) = [\Phi(x,y) + \epsilon_0(x,y)] \mod 2\pi \tag{5.13}$$

where $\Phi(x,y)$ is the total phase at a given point and $\epsilon_0(x,y)$ the measurement error. Hence, for phase maps having a dynamic range higher than 2π, the measured phase values become discontinuous and exhibit indefinite values of integral multiples of 2π. To obtain a continuous phase distribution, i.e. a distribution that conforms to a physical surface, phase unwrapping processes are necessary in all directions (cf. Fig 5.4).

More precisely, the unwrapping process consists of determining to which pixels multiples of 2π should be added to produce a phase map as much continuous as possible. In the last decades great interest was devoted to phase unwrapping, owing to numerous applications in the fields of interferometry, magnetic resonance imaging and synthetic aperture radar interferometry. Nonetheless, phase unwrapping remains today an active research area of digital image processing. Whilst the unwrapping problem is easy to understand, it is a very difficult problem to settle because of the following difficulties:

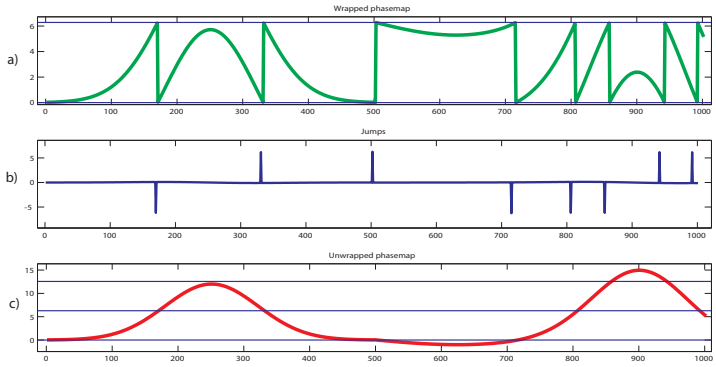

Figure 5.4: a) Phase profile with discontinuities generated from the extraction method. (b) Location of phase jumps. (c) Corrected phase profile with full range values.

- noise can produce jumps between pixels that are not real (artefacts)
- when the phase gradient becomes important, the algorithm may identify a jump and add 2π to the value of the surrounding pixels while it should actually be kept as it is to preserve the correct physical gradient.
- unwrapping methods are usually very sensitive to error propagation and accumulation

Whatever the unwrapping approach used, including the methods from the graph theory [104, 105, 106], Fourier methods [107, 108] and genetic algorithms [109], it will, most of the time, only produce an estimation of the solution. For metrology purpose, the preferred methods are the ones that do not modify the phase value (apart from a factor multiple of 2π), i.e that do not smooth or change the shape of the phase. Thus, basic and graph category methods are usually the methods of choice.

Generally speaking, robust unwrappers require long processing times using digital computers contrary to fast phase unwrappers highly sensitive to noise.

5.6 Study of the shear effect

This section is a reprint of a short paper made for the proceedings of the international workshop on X-ray and Neutrons Phase Imaging with Gratings held in 2011 in Tokyo. Although not offering a straight solution to the problem, this short con-

tribution describes one important limitation when using the grating interferometer for at-wavelength metrology, especially for characterizing reflective optics. The paper also gives a more exact method to derive the XGI equation for data acquired using the phase stepping mode (cf. Sec. 5.3, Eq. 5.4).

Shearing interferometer spatial resolution for at-wavelength hard X-ray metrology

Sebastien Berujon, Hongchang Wang, Eric Ziegler and Kawal Sawhney

Grating interferometers are very attractive tools to perform at-wavelength metrology as they are able to measure wave front gradients with tens of nanoradians sensitivity with a low sensitivity to mechanical vibrations [79, 71, 95, 110, 99]. The ideal on-line X-ray metrology tool should be able to resolve spatial frequencies up to values affecting the X-ray performance of the optics. In the case of X-ray reflective optics characterization, the small grazing incidence angle of the incoming X-ray beam is reducing the beam aperture by a factor of several hundreds with respect to the mirror length, so that wave front sampling is becoming a severe issue. To increase the spatial resolution of the X-ray grating interferometer, one would be tempted to decrease the pitch grating and the detector pixel size. However, in the conventional way of using a phase grating, the shear effect limits the accessible spatial wavelength range. Indeed the shear, defined in the plane of the phase grating by the distance between two interfering rays in the plane of pattern recording, limits the resolvable wave front feature size.

The shear is defined by the two rays of different diffraction orders interfering in the plane of the second grating, noted G2 (see Fig. 5.5). For example, when using a phase grating introducing a π phase shift, the interferences in the plane of G2 are mainly produced by the -1 and 1 diffraction order, making the shear scaling as [76]:

$$s = 2\frac{\lambda}{p_1}Z_t \tag{5.14}$$

where p_1 is the pitch of the first phase grating. To maximize the contrast the inter-grating distance, noted Z_t, is often set to a value corresponding to a partial Talbot order $Z_t = np_1^2/8\lambda, n = 1, 3, 5, ...$

The variation of the phase $\delta\varphi$ of the interferences generated in the plane of G2 is equal to the wave front difference in the plane of G1 from any point separated by the shear

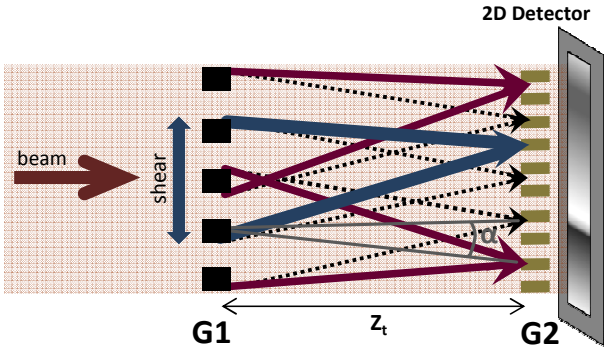

Figure 5.5: Illustration of the shearing distance. The shear is defined as the distance separating two rays in the plane of G1 that interfere in the plane of G2.

amount [90]:

$$\Delta W(x) = W(x + \frac{s}{2}) - W(x - \frac{s}{2}) = \frac{\delta\varphi}{2\pi}\lambda \tag{5.15}$$

This wave front difference can be approximated to the average wave front slope over the shear length:

$$\Delta W(x) = s\frac{\partial W(x)}{\partial x} + \varepsilon(x) = \frac{\delta\varphi}{2\pi}\lambda \tag{5.16}$$

where $\varepsilon(x)$ is derived from the Taylor expansion for a central finite difference:

$$\varepsilon(x) = \sum_{k=1}^{\infty} \frac{W^{2k+1}(x)}{(2k+1)!} s^{2k} \tag{5.17}$$

When working with a π phase shifting grating, the error in the approximation is then proportional to the third derivative of the wave front multiplied by the shear square distance. This value can usually be neglected in the case of a smooth wave front or when the detector pixel size is many times larger than the shear value [111]. Working with a grating inducing a phase shift different from π, e.g. with a phase shift of $\pi/2$, can reduce the shear distance as the interferences are created by the ± 1 and 0^{th} order. However the approximate finite difference used in Eq. 5.15 is no longer centered and the approximation error is then function of $s' = s/2$ and $\partial^2 W(x)/\partial x^2$.

Note that when neglecting $\varepsilon(x)$, the general interferometer equation can be retrieved from equation 5.14 and 5.16:

$$\alpha(x) = \frac{\partial W(x)}{\partial x} \simeq \frac{\delta\varphi}{2\pi}\frac{p\lambda}{4p_1} \tag{5.18}$$

$$\frac{\partial\phi(x)}{\partial x} \simeq \frac{p_1}{\lambda}\frac{\delta\varphi}{2\delta l} \tag{5.19}$$

where α is the local propagation direction of the photons. The shearing transfer

function can also be translated in the Fourier space by [112]:

$$\mathcal{F}[\Delta W(x)](\xi) = exp(i\pi\xi s)\mathcal{F}[W(x)](\xi) - exp(-i\pi\xi s)\mathcal{F}[W(x)](\xi) \tag{5.20}$$

$$\mathcal{F}[W'(x)](\xi) = T(\xi)\mathcal{F}[W(x)](\xi) \tag{5.21}$$

where:

$$T(\xi) = \frac{2isin(\pi\xi s)}{s} \tag{5.22}$$

From this last equation we see that the shearing transfer function acts as a low pass filter of the wave front spatial frequencies. For spatial frequencies such that $s < \xi$, aliasing effects can occur.

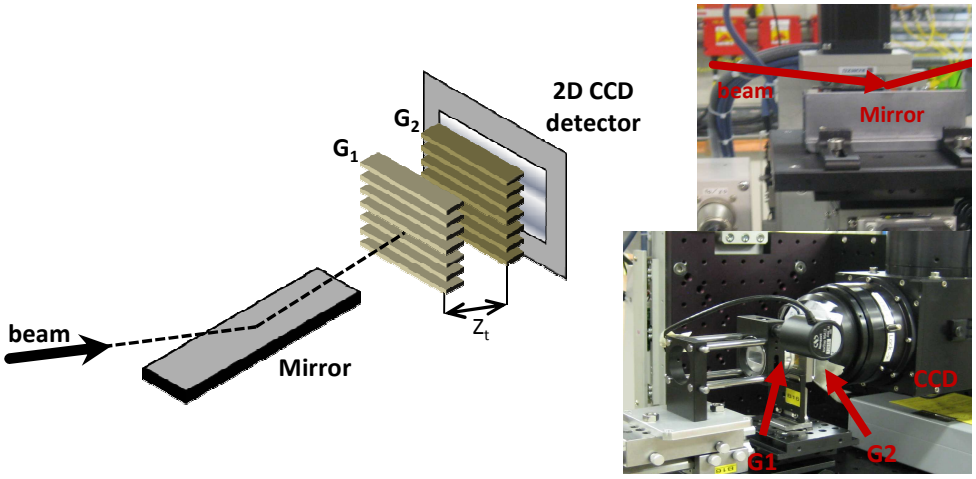

Figure 5.6: Setup of the experiment

The online characterization of a flat reflective optics was conducted at Diamond Light Source Test beamline B16 [26]: the wave front of a hard X-ray beam after reflection on a silicon substrate was measured using the grating interferometer at different Talbot order distances, hence different shear amount (Eq. 5.14). X-rays with an energy of E = 14.5 keV ($\Delta E/E \sim 10^{-4}$) were produced by a bending magnet on a 3 GeV storage ring, located at 50 m from the sample under study. The gratings had a pitch of $p_1 = 4\ \mu m$ for the first phase grating and $d_2 = 2\ \mu m$ for the second absorbing grating. The setup of the experiment is displayed in Fig. 12.6. The detector was a CCD detector with indirect illumination rendering a pixel size of 0.9 μm. The sample under study was a 100 mm long flat mirror made of silicon. The grazing incidence angle of the incoming beam onto the mirror was of $\Theta_{inc} = 0.1$ deg.

The two gratings were first aligned parallel to each other. Then a phase stepping scan was performed collecting 32 images when moving the first grating by a total amount of $2p_1 = 8\mu m$. This stack of image allowed to accurately recover the phase of the Moiré

fringes $\delta\varphi$ recorded by the detector [89]. From equation 5, the wave front slope was calculated and the slope error derived after removal of the linear trend.

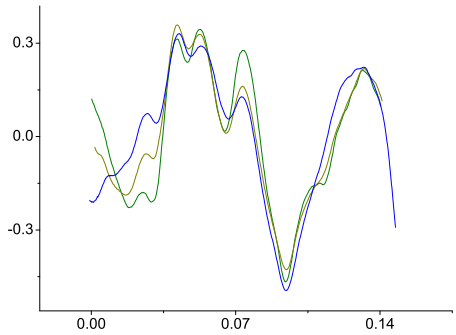

Figure 5.7: Illustration of the shear effect. The same measurement operated at different distances render a slope error profile which is getting smoother as the shear distance increase.

Figure 5.7 shows the calculated wave front slope error from the collected data for different Talbot order distances, that correspond to different shear distance. The shearing distance in our experimental configuration was linearly increased as described by Eq. 5.14, from 7 μm for the 7^{th} order to 13 μm at the 13^{th} order. From Eq. 5.18, it is evident that a better sensitivity is obtained when increasing the inter-grating distance. We also observed that a larger inter-grating distance and then a larger shear distance allows one to reduce the sensitivity of the device to the surface defects of the first grating [113]. However, the drawback of increasing shearing distance is observable by comparison of the four different curves: the higher spatial frequency features disappear as one would expect, letting only the larger features of the mirror slope error for larger shear distance. In that case, the spatial resolution on the wave front is limited by the shear distance. Due to the grazing incidence angle used, the corresponding spatial resolution of the technique on the mirror is decreased by a factor $1/sin(\Theta_{inc})$. As a consequence (Nyquist theorem), slope error defects smaller than 4 mm in the longitudinal direction can not be resolved when working at the 7^{th} Talbot distance order and above.

For metrology purpose, grating interferometers show limitations on the achievable spatial resolution: the shear effect limits the size of the wave front features that can be resolved. One would be tempted to work at lower order to reduce this shear distance, but this would be at the cost of a higher sensitivity to noise. One way to divide the shear consists of changing the phase shift induced by the grating and of working at a different Talbot order distance. Nevertheless, this configuration is also made at either the cost of a decrease in contrast and/or of unwanted contribution of

the second derivative to the measured wave front gradient.

5.7 Comments

As seen in this chapter, one important limitation of the device for metrology purpose is the shear that limits the spatial resolution. The choice of intergrating distance sets a trade off between the sensitivity of the device and its resolution. For some advanced schemes exploited with visible light [112], their extrapolation in the X-ray regime is difficult and no real solution has yet been found. One of the best solutions one can think of is the replacement of the phase grating by an absorption one. Such modification of the XGI would make it usable for the *zeroth* diffraction order to create a structured pattern, in a manner similar to the first Ronchi interferometer. This technique would be also comparable to the coded aperture technique currently developed. The drawback of using two absorption gratings is an important flux decay that would have to be compensated by a longer integration time.

Further in this manuscript will be presented some applications of the XGI to optics characterization and micro sensing using the presented working modes.

6 The X-ray Speckle Tracking technique

This chapter is dedicated to an original technique developed in the course of this thesis project. This new X-ray phase sensing method was inspired from the work of R. Cerbino on a phenomenon recently described in the X-ray regime: the near field speckle. The background, some theoretical aspects and applications of such kind of speckle is briefly presented in the first part. Next, the method is explained through a reprint of the paper describing the method.

6.1 X-ray speckle and near field speckle

6.1.1 Background

Starting from the 1960s with the invention of the laser, techniques using random intensity patterns, named speckle, have been deeply investigated and developed. They are now widely used in scientific and industrial applications such as imaging or metrology. A speckle pattern consists of intensity contrast features arising from the mutual interference of coherent radiation that is randomly scatterered. It can be described as the sum of random phasors:

$$I(Q,t) \propto S_c(Q,t) \propto |\sum e^{iQR_j(t)}|^2 \tag{6.1}$$

The statistical scatterers can either be particles in suspension, transmissive diffusing light objects or rough surfaces from which light is scattered.

There are numerous techniques using speckle including interferometric holography and

electronic speckle pattern interferometry (ESPI) in the field of metrology [114, 115] and stellar speckle astronomy and speckle imaging in the field of astrophysics [116].

Although speckle can be considered as a mature field of optics, it was only introduced in the X-ray community a few years ago with the technique of X-ray Photon Correlation Spectroscopy (XPCS). This technique is an adaptation of the Photon Correlation Spectroscopy and Dynamic Light Scattering techniques used in visible light. It allows the investigation of dynamics of systems and size distribution profiles of particles through statistical analysis.

Correlation of speckle in the near field

In most speckle based techniques, the relevant parameter of interest is the transverse correlation length that can be predicted with the Van-Cittert theorem [117]. The knowledge of this coherence length is of great importance for the treatment of the speckle pattern, either to use it as an information carrier or to suppress it when the effect is considered as noise. In the new XST technique, the wavefield correlation length that matters the most is the one upon propagation. Indeed, we will show that the correlation of the wavefield, and then the speckle pattern, upon propagation permits to use the speckle grain shapes as 'needles' matching the ray trajectories.

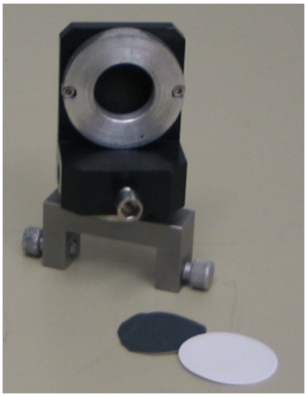

Figure 6.1: Membranes used to generate speckle in a X-ray beam

The normal in-depth correlation length Δz of speckle was investigated and described for visible light by Leushacke and Kirchner in [118] and shown to be in the order of $\Delta z \approx \lambda(z/D)^2$ where D is the aperture of the diffuser and z the distance of the observation plane from it.

However, at the beginning of this century, Giglio *et al.* showed that the observable speckle in the near field had properties different from the previously described one in the far field [119, 120]. Near field speckle (NFS), i.e at very short distances from a scattering object, are correlated in depth over a much longer distance. This implies that the speckle grains do not change in size and shape upon propagation. X-ray NFS is easy to obtain in the X-ray regime due to the very short wavelength of the photons: the distances involved are much larger than in the visible regime and the near field

assumptions can hold true for several meters beyond an aperture. The theoretical properties of the correlation of light in this region was mathematically described by R. Cerbino [121] and the experimental description for hard X-rays presented a couple of years later [24].

Apart from the XST technique, a couple of other techniques take advantage of NFS.

6.1.2 Other use of the X-ray NFS

Complex fluids investigation

Colloids in fluid can be investigated at synchrotrons using techniques such as small-angle X-ray scattering (SAXS) and XPCS [122]. Henceforth, near field X-ray speckle is offering a new solution for the study of colloidal suspensions in dense, optically turbid and/or absorbing media. The idea of investigating colloids fluids with X-ray NFS is motivated by the larger range of scattering wavevector accessible, especially on the lower end, where the scattering is difficult to isolate from the strong direct beam [24, 123].

Probing the coherence beam properties with speckle from Brownian particles

The idea of characterizing the transverse coherence of an X-ray beam using Brownian particles was introduced in the original paper of R. Cerbino *et al.* introducing X-ray NFS [24]. The concept was then put into practice for the first time in the following year [124] on an X-ray undulator beam by Alaimo *et al.*. The experiment consisted of imaging at various short distances a sample containing Brownian particles. Next, the images were processed using Fourier transforms and statistical calculation, allowing the recovery of the transverse coherence lengths in the plane of the sample.

I take here the opportunity to mention that, in Ref. [124], the data analysis did not take into account the contribution of a focusing mirror, thus explaining the curious results obtained that authors interpreted as the presence of an undulator made of two parts. Similar measurements performed at the ESRF BM05 showed a bump comparable to the one observed by Aliamo *et al.* despite the absence of a focusing mirror and of an undulator.

6.2 The X-ray Speckle Tracking technique

6.2.1 Introductory remarks

The following section is a reprint of the paper presenting the developed X-ray speckle tracking technique published in the journal *Physical Review Letters* and entitled Two-Dimensional X-Ray Beam Phase Sensing. Despite a long review process, only few modifications were brought to the manuscript. Meanwhile, a competitive group set an analogous technique in the principle [125]. From the comparison of the two method descriptions, the reader may notice several differences in the approach, in particular regarding the location of the membrane, the description of the speckle features, the working modes and the achievable accuracy.

6.2.2 First paper

Two-dimensional X-ray beam phase sensing

Authors: *Sebastien Berujon, Eric Ziegler, Roberto Cerbino and Luca Peverini*

We present a new method to analyze quantitatively the wave front of a partially coherent x-ray beam. The technique is based on the use of two-dimensional speckle patterns combined with digital image correlation algorithms and offers a pixel size resolution, a high accuracy, and a reduced sensitivity to mechanical vibrations thanks to a very simple setup. The requirements on transverse and longitudinal coherence are also low. Finally, we show how the method can be used for phase contrast imaging applications by a single sample exposure process.

For both beam metrology and phase contrast imaging purposes, the X-ray phase sensing techniques are the subject of investigations worldwide. Indeed, several X-ray techniques based on the coherence properties of the beam, are strongly affected by the local beam characteristics, limiting their performance or degrading their result quality. Thus, the development of tools able to characterize the wave front with accuracy in the order of the X-ray wavelength is required. In parallel, thanks to a high power of penetration, the X-ray photons are able to probe the inner structure of materials. Hard X-ray imaging techniques sensitive to the phase are then the object of special

efforts, as they permit to image thick samples or samples presenting a low absorption.

Currently, various techniques such as pencil beam deflectometry, shearing interferometry, Hartmann wave front sensing and transport of intensity equation (TIE) based methods are available to record and analyze quantitatively the phase of an X-ray beam wave front, or more precisely its derivative. Among them and apart from the basic pencil beam technique, the grating interferometer (GI) [66] is the most widely used advanced instrument due to its accuracy and low requirement on mechanical stability. Nevertheless, the device still suffers one weakness: it is able to measure the wave front gradient in only one direction at a time despite ongoing work [78]. Based on a different principle, the Hartmann sensor [63], does not have this problem: it is able to derive wave front slopes in both directions from a single acquisition. On the other hand, it presents a limited resolution and requires a delicate calibration. TIE based techniques [126] are simple to set but include complex calculations of the data which can suffer from analysis artifacts. Concerning qualitative X-ray phase contrast imaging, the most widespread techniques are presently grating interferometry [91], coherent diffraction imaging [11] and propagation-based techniques [56]. However, they all share the same problem that they require several exposures of the sample to reconstruct one phase image.

The X-ray speckle tracking technique (XST) overcomes these limitations, offering a 2D gradient in a single measurement, a pixel size resolution and an accuracy equivalent to the one of the instruments mentioned previously. The setup is reduced to a minimum, requiring only a random phase object and a 2D detector to resolve the high-spatial frequency features contained in the object. A solid membrane, easy to align and with low sensitivity to vibrations, produces a random intensity pattern (speckle) that is static. By recording this random pattern two times in planes located at two different distances from the membranes or in the same plane at two different time intervals, the ray paths or their evolution can be tracked using a digital image correlation algorithm (DIC) capable of subpixel accuracy (cf. Pan [127]). The validation of the method has been realized on a synchrotron bending magnet source at beamline BM05 of the ESRF. The fact that it works with a multilayer monochromator proves that the longitudinal coherence requirement is low.

The XST method can be understood as a high spatial frequency intensity modulation of the wave front using motionless speckle to trace the geometrical path of the light passing through each pixel of the detector. The key idea is represented in Fig. 6.2: each image subset contains a distinct speckle pattern, that acts as a singular marker,

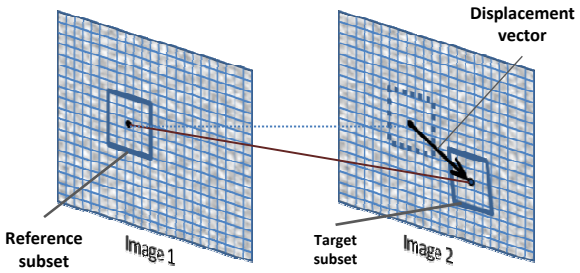

Figure 6.2: DIC principle. The position of a speckle subset of few pixels is tracked from one image to the next using a cross correlation criterion.

and can be numerically tracked between images taken at different times or in different planes in space.

The use of speckle can be found in many X-ray techniques, such as X-ray photon correlation spectroscopy and coherent diffraction imaging. Contrary to those methods, the XST technique uses the near field speckle also present in the X-ray regime as demonstrated by Cerbino et al. [24]: these speckle grains have the property to not change in size and shape over a distance along the propagation direction that is inversely proportional to the wavelength and therefore is much larger for X-rays than for visible light [121]. With X-rays, the distance between planes (Fig.6.2) becomes large enough to use numerical algorithms to follow the speckle trajectories. Indeed the curvature of the near field speckle trajectories coincide with the curvature of the beam. In practice, the distance z over which speckles of size d can be tracked in depth, is not limited to the deep Fresnel region as described by Cerbino ($z_{NF} < dD/\lambda$, where D is the transversal coherence size and λ the wavelength) but can go until $z = D^2/\lambda$, corresponding to the transition between the Fresnel and far field regimes [117]. Above that distance, the distortion of the tracked subsets becomes too important comparatively to the robustness of the algorithms employed. An additional effect that we can naturally benefit from is the divergence of the X-ray beam: for a beam of divergence α, the near field distance is increased by a factor $1/(1 - \alpha d/\lambda)$ and the geometrical magnification of the speckle pattern is small enough to obtain usable correlation coefficients in the numerical algorithms. Hence, the tracking gives excellent results over a range that can vary from several centimeters to many meters, depending on the X-ray energy, the size of the scattering objects and the beam divergence, as we shall demonstrate with the examples below. To produce a speckle pattern, we used membranes with dephasing objects smaller than the transverse beam coherence but large enough to be resolved with our detector. These membranes, e.g. biological filtering membranes or abrasive paper, are thermally stable under monochromatic X-ray beam.

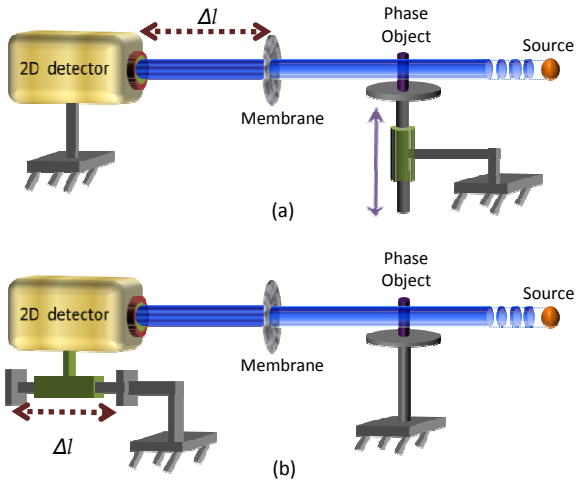

Figure 6.3: Two possible configurations. In configuration (a), the sample is removed to obtain a reference beam and work differentially, while in configuration (b) two shots are taken at different distances from the membrane to act as a Hartmann sensor, the sample remaining in the beam.

Two configurations are presented in Fig. 6.3. In each case, only two speckle images are acquired, allowing the monitoring of the ray path for each pixel using the DIC algorithms. One should understand the fundamental difference between those configurations. The scheme in Fig. 6.3.(a), labeled "differential configuration", uses a reference speckle image plus another image with a phase object introduced in the beam path. When using this setup, the displacement vectors calculated give information about the wave front distortion introduced by the phase object only. The alternative setup in (b), labeled "absolute configuration", uses two images taken at different planes in space. In this latter case, calculation from the two speckle images will give access to the quantitative wave front at one of the image planes, comprising the distortion to the wave front induced by the elements present along the beam path: optical elements, windows, etc... Anyhow, the displacement vector can be compared in both setups to the one used in a Hartmann sensor, i.e. the shifting of a spot from its theoretical position.

The DIC algorithms [127] are usually used to describe the distortion of a material under mechanical strain. The so-called mapping function is commonly employed, to define the motion of a subset centered on a given pixel $P_{ini} = (x_0, y_0)$ in the unitary base $(\boldsymbol{x}, \boldsymbol{y})$:

$$\begin{aligned} x'_0 &= x_0 + \xi(x_0, y_0) \\ y'_0 &= y_0 + \tau(x_0, y_0) \end{aligned} \tag{6.2}$$

where $\xi(x_0, y_0)$ and $\tau(x_0, y_0)$ reflect both the translation of the target subset as well as

its distortion from the reference subset in (x_0, y_0). The DIC scheme is usually a two steps procedure. The first one is the calculations of the displacement vectors of the subsets with pixel accuracy. Those results are then used as an input for the second step in which a subpixel accuracy algorithm is applied. Indeed, these algorithms are able to calculate displacements with a reproducibility of a hundredth of a pixel when providing an initial guess within one pixel radius from the final solution.

Among the algorithms able to calculate the displacement vector of a subset within a one pixel accuracy [127], the zero-normalized cross-correlation (ZNCC) is the best choice. The ZNCC criterion evaluates a similarity factor between a subset of M points in the reference image f and a target subset centered on (α, β) in a second image g:

$$C(\alpha,\beta) = \sum_{x=-M}^{M}\sum_{y=-M}^{M}\left[\frac{\left[f(x,y)-\overline{f}\right]\left[g(x',y')-\overline{g}\right]}{\Delta f \Delta g}\right] \tag{6.3}$$

where $\overline{f}$ and $\overline{g}$ are the mean value of the subsets and Δf and Δg their respective standard deviation. Then, for each subset around a given pixel, the displacement vector is the one that verifies $\boldsymbol{\nu} = \overrightarrow{(P_{ini}, P_{max})}$ where $P_{max} = (\alpha_0, \beta_0)$ and $C(\alpha_0, \beta_0) = \max_{(\alpha,\beta)} C(\alpha, \beta)$. This correlation criterion being the least sensitive one to spatial and temporal intensity variations in the beam, offers the best choice in terms of robustness. This allows one to perform wave front analysis and imaging downstream a moderately absorbing sample. For the second step, several DIC algorithms with subpixel accuracy have been developed over the last few decades (cf. [127]). In the following experiments, for time consumption issue, we used the MATLAB© peak finder algorithm that, like the other algorithms of its class, does not consider the deformation of the subset, treating only the rigid translation of the subset $\boldsymbol{\nu}$ and:

$$\begin{aligned}\xi(x_0, y_0) &= \boldsymbol{\nu}.\boldsymbol{x} = \nu_x \\ \tau(x_0, y_0) &= \boldsymbol{\nu}.\boldsymbol{y} = \nu_y\end{aligned} \tag{6.4}$$

While this is enough to characterize the first order gradient of the wave front using Eq.6.5, taking the subsets distortion into account would provide additional information about the second derivative of the wave front, i.e. the wave front curvature [128].

Once the ray paths have been calculated, the phase recovery is done in both configurations, using the relationship linking the local angular deviation of the beam, i.e. the wave front slope, to the gradient of the phase in both directions:

$$\Theta_n \simeq \frac{\nu_{x,y}}{\Delta l} = \frac{\partial W(x,y)}{\partial n} = \frac{\lambda}{2\pi}\frac{\partial \phi(x,y)}{\partial n}, n \in \{x, y\} \tag{6.5}$$

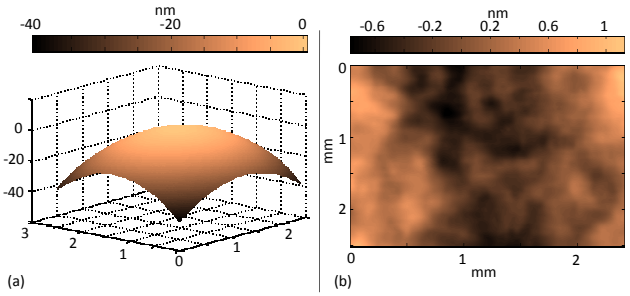

Figure 6.4: (a) Reconstruction of the ESRF BM05 wave front after double reflection on Si(111) monochromator.(b) Wave front departure from a perfect spherical wave front.

The attainable accuracy depends directly on the resolution d_{pix} of the 2D detector, and on the working distance Δl between two image planes or between the membrane and the detector according to the configuration used (Fig. 6.3). The smallest deviation that can be measured is given by: $\Theta_{min} = d_{pix} \times \delta_{CCC}/\Delta l_{max}$ where δ_{CCC} is the pixel accuracy of the Cross Correlation Criterion. In the experimental setup we used, $\delta_{CCC} \leq 0.05$ pixel, $\Delta l_{max} = 200\ mm$ and $d_{pix} = 0.8\ \mu m$, leading to a theoretical accuracy of $\Theta_{min} \sim 0.1\ \mu rad$, which is already as good as the current GI and Hartmann instrument. A further gain in accuracy of one order of magnitude would already be reachable using a smaller pixel size detector, and/or by placing the detector further away from the membrane.

A series of experiments were conducted at beamline BM05 of the ESRF, where the X-rays are produced by a bending magnet on a 6 GeV electron storage ring. The working energy was set to $E = 17keV$ ($\lambda = 0.073\ nm$) either with a multilayer monochromator ($\Delta E/E = 10^{-2}$) or with a double flat Si(111) monochromator ($\Delta E/E = 10^{-4}$). With the experimental station placed at 40 m from the source, the transverse coherence length is approximately 9 μm horizontally and 25 μm vertically [129]. The divergence of the beam is 2.4 $mrad$ horizontally and 180 μrad vertically. The beamline specifications are detailed in Ref. [25].

A first simple illustration of the method, using the scheme of Fig. 6.3.(b), is given in Fig. 6.4: (a) is the reconstruction of the beam wave front after the Si(111) monochromator. Slits were used to set the beam size to $2.5 \times 2.5\ mm^2$. The field of view of the camera permits to analyze the beam with a micrometer resolution over several square millimeters. The wave front error from the perfect spherical wave front is shown in Fig. 6.4.(b). We can observe that, over the full aperture, the wave front error is much larger than the wavelength. However, the dephasing over any area of size $9 \times 25\ \mu m^2$ (coherence area) is never larger than $\lambda/2$.

	Calc. distance
Direct Beam 40.5 m	40.7 m
Bent mirror f = 350 mm	352 mm
Monolithic mirror f = 60 mm	60.5 mm

Table 6.1: Comparison between direct length measurements and their determination by the present technique.

Using the same configuration, we compared the wave front derived from the XST technique when various optical elements were inserted in the beam. The 2D detector was mounted on a precision translation stage with a reproducibility of 1 μm. The X-ray energy was defined with a multilayer monochromator. An abrasive paper made of SiC powder with a mean grain size of 5 μm was placed at 34 m from the source, i.e. 6.5 m upstream from the detector. For the direct beam measurement, images of the speckle pattern produced by the abrasive paper were imaged at two different positions separated by a distance $\Delta l = 200\ mm$. The coupling of a Frelon CCD camera to an optical system (indirect illumination) was equivalent to using a detector with a pixel size of 0.8 μm (effective pixel size). From these two images, the wave front was numerically reconstructed [130] and fitted to an ellipsoid. The same procedure was repeated after insertion of either a dynamically-bent mirror or a monolithic focusing mirror. This time the effective pixel size was of 5.8 μm, the membrane was situated around the focal point of the mirror and $\Delta l = 120\ mm$. The calculated values for the wave front curvature are presented in Table 6.1; they are in good agreement with the experimental conditions. As phase information can be collected for every pixel, 2D phase imaging becomes realizable. Phase imaging is of great interest for sample with low absorption, e.g. made of light materials, or sample made of different materials with similar attenuation coefficients. For this experiment, the scheme in Fig. 6.3.(a) was used with the sample placed on a translation stage and a fixed cellulose acetate membrane with a pore size of 0.8 μm located 600 mm downstream to generate the speckle pattern. The 2D detector arrangement had an effective pixel size of 0.8 μm and was placed $\Delta l = 940\ mm$ downstream from the membrane. The sample situated at a distance of 40.5 m from the source, consisted of a PMMA cone introducing a phase gradient. The cone radius was 4 mm and the opening angle $\vartheta = 140$ deg. The complete field of view of the detector was illuminated. The tip of the cone and the detector were both centered with respect to the beam. Sequentially, a first exposure was acquired with the sample present; a second one was acquired after sample removal. The displacement vectors were then calculated for every pixel and the wave front reconstructed. Absorption, estimated to be $\beta \approx 10^{-10}$, had no effect; nevertheless the displacements of the speckle allowed a perfect reconstruction of the cone (Fig. 6.5). At a distance of 940 mm, the radial displacements of the speckle subsets in the cone, equal

to 0.41 pixel, correspond to an angular deviation of 0.35 μrad. From the expression linking δ to the wave front gradient $\frac{\partial W(x_{ij},y_{ij})}{\partial x} = \delta \times tan((\pi - \vartheta)/2)$, we obtain $\delta = 9.6 \times 10^{-7}$ which is in very good agreement with the refractive term of the optical index for PMMA at 17 keV [131].

When imaging a low absorbing sample, one can get direct access to the absorbtion map by simply dividing the two images recorded. However, an important point to take care when imaging strongly absorbing sample or when using very low flux, is to have a minimum of counts per pixel to ensure trustable correlation calculations in the DIC algorithm. Moreover, one has to be aware of the size limit of the phase objects that can be resolved; at the position of the membrane, the features of the wave front need to be larger than the speckle grains to not disturb too strongly the speckle pattern. A simple way to overcome this limit and gain resolution, is to insert an optical focusing element into the beam and adjust the membrane and sample positions to obtain the required speckle size and sample features through magnification.

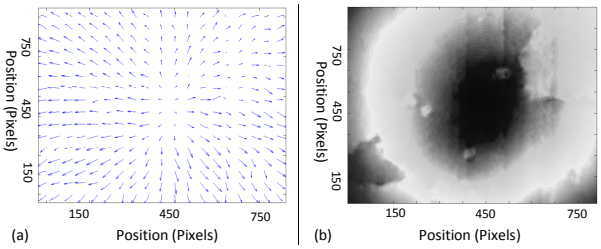

Figure 6.5: Displacement vector field at center(a) and phase-map reconstruction of the cone sample(b). The blurs in the phase map correspond to phase accidents that are due to the presence of micro air bubbles in the glue of the sample holder.

Since the beam passes through the membrane with almost no absorption and only one exposure is required for the sample, the sketch shown on Fig. 6.3.(a) is dose efficient, therefore suitable to the analysis of biological tissues for which the dose absorbed is an issue.

In conclusion, we have exposed the basis and some illustrations of an efficient technique for accurate quantitative two dimensional phase sensing of a partially coherent X-ray beam. The presented examples open perspectives for the XST method at synchrotron and X-FEL sources, for instance in bio-imaging and inverse ray tracing. The optical simplicity of the experimental configuration may seem to be tempered by the extensive need for computing time. This is actually not a true limitation considering that the used algorithms are perfect candidates for parallel implementations on, for example, some of the new GPU clusters available on the market.

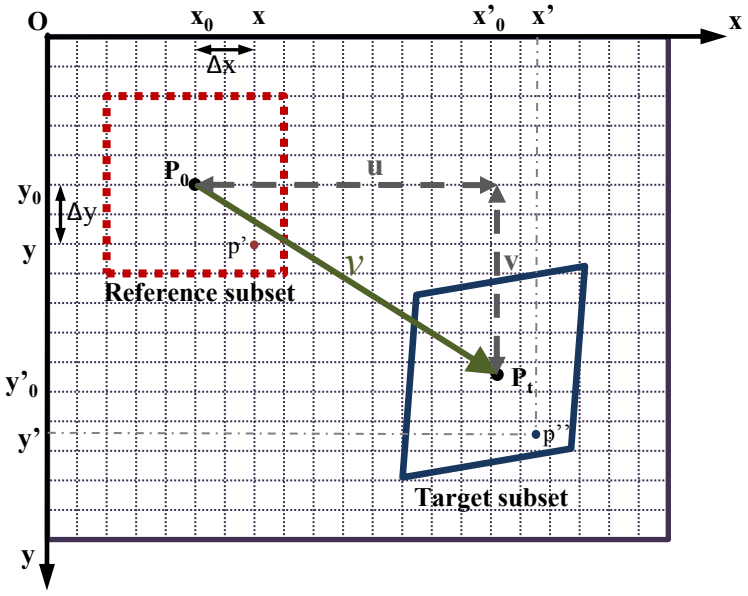

Figure 6.6: Digital image correlation geometry consideration.

6.2.3 Wavefront local curvature

In the previous paper, only the rigid translation of the subsets was considered in the peak finder DIC algorithm, and we used:

$$\xi(x_0, y_0) = u \quad , \quad \tau(x_0, y_0) = v \tag{6.6}$$

However, as already mentioned, the consideration of the subset distortions provides additional information on the local higher derivatives of the wavefront. For instance, in order to extract the local curvature in the pixel (i, j) defined by $\kappa_{ij} = \frac{1}{R_{ij}} \approx \nabla^2 W$, one has to consider the second order subset distortion [127]:

$$\begin{aligned} \xi(x_0, y_0) &= u + u_x \Delta x + u_y \Delta y \\ \tau(x_0, y_0) &= v + v_x \Delta x + v_y \Delta y \end{aligned} \tag{6.7}$$

In this set of equations, $\Delta x = x_i - x_0$ and $\Delta y = y_j - y_0$ are the distances from the subset center P_0 to a point p' of the subset. The coefficients noted u_x, u_y, v_x and v_y are the first-order displacement gradients of the reference subset, and u_x and v_y can also be seen as the magnification M_{ij} of a subset between images.

To extract the subset distortion coefficients characterized by the coefficient $\{u_x, u_y, v_x, v_y\}$, more advanced tracking algorithms, like the ones of the Newton-Raphson category, can be employed.

Using the relation $M_{ij} = 1 + \dfrac{\Delta l}{R_{ij}}$, the local curvatures in the $(\mathbf{x}, \mathbf{y})$ base of a subset centered in $P(x_i, y_j)$, becomes then:

$$\kappa_{ij}^{x} = \frac{u_x - 1}{\Delta l} \quad , \quad \kappa_{ij}^{y} = \frac{v_y - 1}{\Delta l} \tag{6.8}$$

6.2.4 Detector distortion

The detectors used in this project to record the images were based on the CCD technology, the camera using indirect illumination, a scintillator converting the X-rays into visible light. Despite the good quality of the visible light microscope objective employed to image the scintillator, distortion still occurs from this optics. To characterize it and then correct for this unwanted effect, one can use the XST technique to calculate the imaging system distortion.

The idea is two take two images of the same speckle pattern but translating the detector by a small quantity $\mathbf{t}$ between the two acquisitions. The expected transformation between the images is therefore a rigid translation of all subsets and for a distortion free detector we shall have $\mathbf{v_{ij}} = -\mathbf{t}$, $\forall\{i, j\}$.

For a very small displacement $\vec{t}$, the local distortion factor of the calculated wavefront gradient (γ_x, γ_y) in the basis $(\mathbf{x}, \mathbf{y})$ is :

$$\begin{cases} \gamma_{x_{ij}}, = \dfrac{\mathbf{v_{ij}}.\mathbf{e_x}}{\mathbf{t}.\mathbf{e_x}} \\ \gamma_{y_{ij}}, = \dfrac{\mathbf{v_{ij}}.\mathbf{e_y}}{\mathbf{t}.\mathbf{e_y}} \end{cases} \tag{6.9}$$

In the differential mode, because the local detector distortion is locally small (<2 % even in the corners) and the displacement vectors $\vec{v}$ have a maximum amplitude of a few pixels, the error induced by the detector distortion on the measurement can be neglected. However, this distortion will have to be taken into account for restoring the original image shape.

When working in the absolute mode, the subsets in two images corresponding to the same speckle may be located in area of the detector field of view sufficiently distant from each other to call for a compensation of the detector distortion induced by the detector.

In this context, new array detectors free from distortion can be seen as natural solutions to this problem.

6.3 Broader comments

Deflection based techniques (DBT) are phase sensitive methods that calculate local angles α in the near field to recover the corresponding local gradient of the wavefront W through the basic equation: $\alpha = |\nabla.W|$ [9]. For this reason, among others [132], they differ from the propagation based ones that are sensitive to ΔW, that is the second derivative of the wavefront, in other words its curvature.

As seen previously, DBT includes the grating based methods, such as shearing interferometry, Hartmann and coded aperture devices, and from now on the speckle tracking methods. These techniques all share the principle of wavefront modulation with features whose spatial frequencies are high in comparison to the ones of the object under investigation, in order to retrieve the local deflection angle.

Since the making up of the XST technique, alternative techniques made also a number of significant advances. At this stage it may be interesting to put the XST techniques in perspective with its competitors, although some aspects were already mentioned previously.

Until recently X-ray shearing interferometers [132, 91, 99, 133, 92], based on phase and absorption gratings [79] and the use of coherent light to generate interferences could only measure the wavefront gradient in one direction because of the challenging fabrication of 2D gratings. This issue being now overcome [94, 95], devices can now measure the phase gradient in two directions within a single scan. Advantages of such a device include the possibility of operating with a laboratory source [68], the ability of providing a scattered phase map [134] and finally the possibility of using a second analyzer grating. The latter is of great interest when using a large detector pixel size and hence a large field of view, because it creates large interference fringes that translate the irresolvable small fringes created by the phase grating in a resolvable pattern [134].

A mode where the two gratings are not parallel as described in Sec. 5.4, also permits to recover the beam phase in a single image [103]. However, although this mode is

suitable for time resolved experiments, i.e for the study of dynamic samples, it still suffers from several processing drawbacks. Another way of achieving quantitative single shot imaging consists of removing the second grating in combination with the use of a more resolving detector [135]. New schemes were also realized showing how to minimize the dose delivered to the sample when performing grating interferometry tomography [70]. Other work [136] showed a way of weakening the constraint of precise positioning of the second grating by widening the spectral bandwidth. Regarding microscopy applications, it is worth noticing that the shear effect inherent to this device will always limit the spatial resolution to values of several micrometers, whereas this effect is not experienced when working with a pixel size larger than the shear distance [91, 133, 71, 75].

Instead of using the grating diffraction effect, coded aperture [64, 65] and Hartman instruments [63, 62] put the effort on tracking the propagation direction of beamlets created by some absorbing grid patterns. Great progress has been realized with these devices, both on the hardware (grating and detector) and on the processing methods. Thanks to a pre-calibration, they are also able to provide quantitative phase analysis from data acquired from a single exposure.

As mentioned earlier, the XST technique presented [137] in this chapter also falls in the deflection angle category. Beyond its advantages of using a simple setup without any grating, as also mentioned by Morgan *et al.* in some approaching parallel development [125], the technique is perfectly suited to the study of a dynamic sample. Here, neither the shear effect, nor the aperture separation distance are factors limiting the spatial resolution. Moreover, membranes producing statistically uncorrelated speckle of any size can be found on the market. Hence, a detector with improved resolution will readily allow resolving smaller spatial features of the sample. Another perspective for improving the technique would consist of replacing the phase object with an object with similar spatial features but presenting some (small) absorption, in order to match the degree of coherence available. Such substitution would permit the use of the technique with a laboratory source and access a greater community of users and applications.

The field of DBT being presently very active, referencing recent advances made by other groups within the past year was necessary for a fair evaluation/comparison of the various techniques and to clarify the complementary aspects of our method with alternative approaches. This section emphasizes the point that the XST technique can address applications requiring high resolution as we shall see in Sec. 12.2 (down to the nanometer scale) and is well suited to the study of dynamic samples. It is also

underlines that grating interferometers are better suited to applications involving a large field of view, considering their ability to detect features at a scale below the one of the detector thanks to the analyzer grating and the scattering effect [138, 139, 140]. Finally coded aperture and assimilated methods, thanks to the incoherent light they use, can find many applications with laboratory sources for single shot imaging [141].

7 Unification of the methods: a generalized scheme

7.1 Introductory remarks

This chapter introduces a new method that will make a cross-over between the XST and XGI approaches. It can be understood as a generalization of the XGI. The key idea is to consider a speckle pattern as being the superimposition of a series of fringe patterns with multiple spatial frequencies, as depicted by the Fourier transform. More mathematically advanced processing would permit the recovery of the phase and of scattering maps in a way similar to the XGI. Like XST, this imaging method works either differentially to suit the study of a transmission sample or optics, or in absolute mode when characterizing the phase state of an X-ray beam.

This method is also based on speckle, i.e a pattern seen as a sum of random phasors. Yet, the XST technique and the new generalized scheme are different in approach although they both fall in the deflection technique category as sketched in Fig. 7.1. The quantity measured within XST and the new generalized scheme are not fully equivalent as represented by the angle α in Fig. 7.1.(a) and (b). For the XST technique (Fig. 7.1.(a)), the measured angle is located in the plane of the wavefront modulator and corresponds to the propagation direction of the light. By contrast, in the XGI and generalized schemes, the measured angle is located in the plane of the detector as we shall see in the next section. While this latter quantity is only an approximation for the light propagation direction, it holds true for small angles, which is the case for the X-ray regime.

The rest of this chapter is a reprint of the paper entitled "X-RAY MULTI MODAL IMAGING USING A RANDOM PHASE OBJECT", published in the journal *Physical Review A*

and describing the method together with some examples of applications.

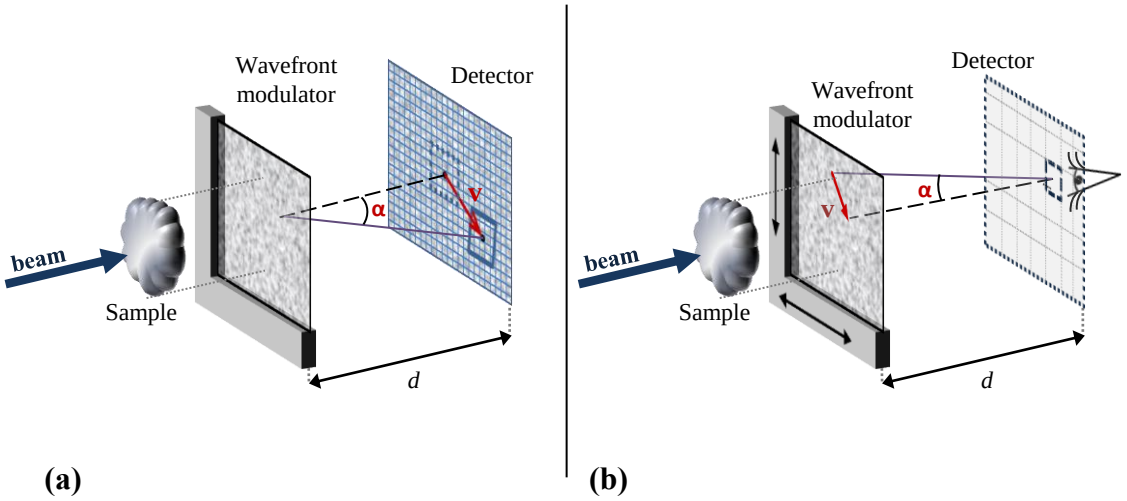

Figure 7.1: Fundamental difference between the XST technique (a) and the generalized scheme (b).

7.2 Second paper

X-RAY MULTI MODAL IMAGING USING A RANDOM PHASE OBJECT

Authors: *Sebastien Berujon, Hongchang Wang and Kawal Sawhney*

We demonstrate an extension of the X-ray grating interferometer three modal imaging method to a generalized stepping scheme using a phase object with small, random features. The method allows the recovery of the absorption, scattering and two dimensional phase image of the sample from a raster scan of the phase object. An additional extension of the method to recover the effective wavefront curvature is also described. The technique provides fine sensitivity, high spatial resolution and has only low requirements on spatial and longitudinal coherence of the X-ray beam. Imaging modes and processing methods are explained, and an experimental demonstration of the technique is provided by imaging a feather and the quantitative characterization of a compound refractive lens.

7.2.1 Introduction

Imaging has been one of the main applications of x rays since their discovery. Whilst the highly penetrating nature of x rays is commonly used to reveal the interior of material objects, the scientific community has also exploited the short wavelength of x rays to image sample features down to the nanometer scale. To achieve high spatial resolution or image light material, new X-ray imaging techniques exploiting the phase of the waves were developed over the two last decades [132]. One such technique is X-ray grating interferometry.

The use of X-ray grating interferometers (XGI) has quickly spread following the adaptation of the device from visible optics [75, 76] to hard x rays [66, 91, 132] and the demonstration of coherence mapping. Today, a large community takes advantages of this device using both synchrotron and laboratory sources [68, 92]. Indeed, its imaging capabilities make it very attractive: in addition to an absorption map of the sample, it also provides the phase shift and the scattering map induced by the sample [134] on an X-ray beam.

The phase shift corresponds to both the delay and the local angular deflection on the photon beam propagation by the sample. Recovering this valuable information directly permits the deduction of the refractive index δ of the sample. Such information is of particular interest for low-Z materials where the value of δ is many orders of magnitude larger than the absorption factor β of the optical index $n = 1 - \delta - i\beta$.

For many years grating interferometers were limited to the measurement of the phase gradient in only one direction due to the technical challenges in fabricating two dimensional gratings. However, the issue has recently been overcome [94] allowing the recovery of the two directional phase map in a single scan. A few researchers also reported the possibility of using XGI in a magnification geometry in an attempt to improve the spatial resolution of the device for imaging purposes [142, 110].

The idea of mapping the scattering properties of an object came out only a few years after the extension of the grating interferometer to the X-ray regime [134]. The principle is to calculate the local reduction of the coherence which arises from small angle scattering in the sample. The mapping of this scattering effect is also sometimes called dark-field image and reflects the degree of inhomogeneity at the nanometer scale inside the sample.

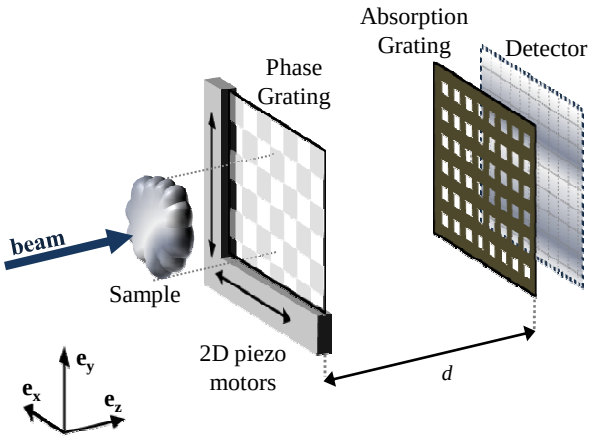

Figure 7.2: Schematic of a two dimensional X-ray grating interferometer. Gratings are placed in an X-ray beam downstream from a sample to create an interference pattern. The distortion of this pattern from the one obtained when no sample is inserted into the beam, permits the recovery of the phase shift induced by the sample.

A schematic of an XGI is shown in Fig. 7.2. The grating interferometer is also sometimes called the 'shearing interferometer' because it relies on a phase grating to split or 'shear' the beam into two diffracting orders. The two parts of the beam then interfere further downstream from the phase grating, creating a fringe pattern. The position and amplitude of these interference fringes allow the calculation of the phase shift and absorption of the sample. Often the pixel size of the detector is larger than the grating period, and placing a second absorbing grating with a tuned pitch in front of the detector creates larger resolvable Moire fringes due to the aliasing effect. For accurate phase retrieval, the XGI is usually used in a scanning mode where several images are acquired whilst moving one of the gratings relative to the other in a plane transverse to the beam. In interferometry such a process is called phase stepping [87]. From these images, Fourier methods are used to recover the beam gradient through the fringe phase calculation.

The fabrication of the XGI's gratings is a technical challenge [79], especially when the gratings are designed to work at high energy. The grating lines are required to have a period of a few microns to achieve good sensitivity and spatial resolution of the device. At the same time, the aspect ratio needs to be very high to induce a phase shift large enough to produce a workable contrast, leading to line depths ranging from 15 μm to more than 100 μm when designed to introduced π phase shift at high energy [85]. These gratings are usually made by electron beam writing or XUV lithography and wet etching on silicon substrate. The second absorbing grating has its lines filled with heavy elements such as gold deposited by electroplating. Hence, the grating pitch limits the spatial resolution of the interferometer, whilst the absorption of the device at lower X-ray energies may sometimes be an issue. Finally, as one might expect, the

quality of the grating can affect the results [113].

In spite of the advantages of the XGI, researchers are still exploring and developing improved or derived methods [143, 64]. These efforts are motivated by the desire to image matter at ever higher spatial resolutions whilst diminishing and minimizing the X-ray dose delivered to the sample.

A new X-ray beam phase sensing technique has recently been developed for imaging and metrology purposes: this technique [137, 125] relies on the use of X-ray near-field speckle [24] combined with cross-correlation algorithms. In addition to several other advantages, the technique has been shown to provide a few tens of nanoradians sensitivity in the measurement of wavefront gradients, and spatial resolution on the micron scale. Despite promising possibilities for imaging using the differential mode, in which the contribution of the sample on the phase of the X-ray beam is isolated, the technique suffers from several drawbacks, including: measurements are limited by the magnification of the speckle upon propagation whilst using the absolute mode to recover the effective phase of the beam; the spatial resolution of the technique is limited by the size of the speckle grains; and finally scattering maps are not accessible, unlike with XGI.

We propose a generalized method, derived from the XGI that uses any phase generated pattern or speckle rather than a periodic grating. Here a simple membrane with random features replaces the phase grating. Using a complete mathematical description of the stepping scheme, we show that the requirement of a grating with a perfectly known pitch, as employed in the XGI, is not essential. The method provides the two dimensional beam phase gradient, employs a simple setup, and achieves higher spatial resolution than the current XGI devices. It is also shown that the XGI is a special case of the generalized method presented.

7.2.2 Theory

Basis

The concept of this paper is to consider a sample as a time invariant system represented as a transfer function h, which is linked to the optical index n of the sample. For the following, we consider a monochromatic beam propagating through a sample in the

z direction of a frame $(\mathbf{x}, \mathbf{y}, \mathbf{z})$ and with transverse coherence lengths of the order or smaller than the sample features. Placing an imaging detector downstream of the sample, the intensity collected I_{det} at a point $T = (x_0, y_0)$ will be equal to the square modulus of the probing wave u_0 convoluted with the optical transfer function $h_T(x, y) = h(x_0, y_0, x, y)$ [5, 8]:

$$\begin{aligned} I_{det}(x_0, y_0) &= |u(x_0, y_0)|^2 \\ &= \left| \iint_{-\infty}^{+\infty} h(x_0, y_0, x, y) u_0(x, y) dx dy \right|^2 \\ &= \iiiint_{-\infty}^{+\infty} h_T(x_1 - x_0, y_1 - y_0) h_T^*(x_2 - x_0, y_2 - y_0) \\ &\quad < u_0(x_1, y_1) u_0^*(x_2, y_2) > dx_1 dy_1 dx_2 dy_2 \end{aligned} \tag{7.1}$$

One approximation is made for the following treatment: the small transverse coherence length of the beam is neglected and the field correlation function $\langle u(x_1, y_1) u^*(x_2, y_2) \rangle = I_0(\frac{x_1+x_2}{2}, \frac{y_1+y_2}{2}) \psi_0(x_1 - x_2, y_1 - y_2)$ is taken as incoherent illumination. This means that $\psi_0(x_1 - x_2, y_1 - y_2) \approx \kappa \delta(x_1 - x_2, y_1 - y_2)$ with δ representing the Dirac distribution. Whilst this approximation for the width of the function ψ_0 does not affect the beam phase sensing, the partial coherence of the X-ray beam will be responsible for some edge contrast in the absorption image. Denoting $\mathscr{F}$ as the Fourier transform operator, Eq. 7.1 can be then written using the convolution theorem and the two functions $\mathscr{F}[|h|^2] = H$ and $\mathscr{F}[|u_0|^2] = \tilde{I}_0$ [5, 8]:

$$\begin{aligned} I_{det}(x_0, y_0) &= \kappa \iint_{-\infty}^{+\infty} |h_T(x - x_0, y - y_0)|^2 I_0(x, y) dx dy \\ &= \mathscr{F}^{-1} \left[\kappa H(x_0, y_0, \xi, \nu) . \tilde{I}_0(\xi, \nu) \right] \end{aligned} \tag{7.2}$$

The way to recover the optical transfer function h of the sample is to feed the system

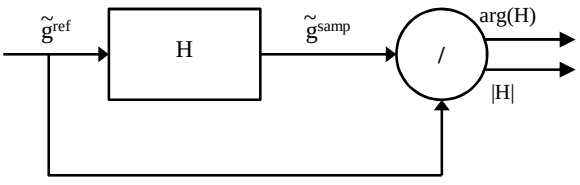

Figure 7.3: Processing representation

with a reference signal $|u_0|^2$, which is a two dimensional (2D) pattern, and compare this with the signal collected at the exit of the system. Figure 7.3 schematically describes this scheme which is a common problem in physics and signal processing. More precisely, it consists of estimating the transfer function $H(x_0, y_0, \xi, \nu) = H_T(\xi, \nu)$ of the sample which is applied to the reference signal, and to do so for each pixel T determined by the index pair (k, l):

$$H_{kl} = \frac{\tilde{g}_{kl}^{samp}}{\tilde{g}_{kl}^{ref}} \tag{7.3}$$

where the operator $\sim$ denotes the Fourier transform of the function $\tilde{g} = \mathscr{F}[g(x, y)](\xi, \nu)$. The functions $g^{ref}(x, y)$ and $g^{samp}(x, y)$ respectively describe the 2D optical intensity recorded when the sample is out of the beam(flat field reference) and when the sample is introduced into the beam. These functions reflect physical recorded signals and are then bounded by a finite subspace Γ of size $\Gamma_x \times \Gamma_y$. Thus, the Fourier transform is treated in the following in the exponential Fourier series limit:

$$\tilde{g}(\xi, \nu) = \frac{1}{\Gamma} \int_{\Gamma} g(x, y) e^{-i2\pi(\xi x + \nu y)} dxdy \tag{7.4}$$

with $\xi = p/\Gamma_x$, $\nu = q/\Gamma_y$, $(p, q) \in \mathbb{Z}^2$ the set of integers.

We show how to recover $|H|$, which represents the absorption and decrease of coherence brought about by the sample, and also demonstrate that the argument $arg(H)$ relates to the beam gradient.

Stepping scheme

Instead of considering a grating producing interference, consider a phase object with high frequency features creating local phase shifts on a partially coherent wavefront. As with many propagation based contrast imaging techniques [23, 144, 126], the object will create interference contrast after propagation over a short distance z due to the local curvature of the beam. This phenomena can be described by the Transport of Intensity Equation [145]:

$$\frac{2\pi}{\lambda} \frac{\partial I}{\partial z} = -\nabla.(I \nabla \varphi) \tag{7.5}$$

with λ the wavelength. In Eq. 7.5, I is the recordable intensity and ∇ represents the transverse nabla operator in the plane $(\mathbf{x}, \mathbf{y})$ perpendicular to the beam propagation

direction z. The phase of the beam is φ, and a surface defined by $\varphi(x, y, z) = cst$ is the wavefront W.

When interferences arise from spatially uncorrelated features, it creates a random interference pattern called speckle [117]. With hard x rays and up to a certain propagation distance, a more specific form of speckle is obtained: the 'near field speckle'. This kind of speckle, used here, has been demonstrated to be closely related to the form and structure of the scattering object [24].

The experimental setup consists of mounting a phase object with small features, downstream of a removable sample, on a piezo motor that allows translation in the two transverse directions of the X-ray beam. Likewise, a 2D detector able to resolve the near-field speckle pattern is placed into the beam. In this manner one can perform the so-called stepped two dimensional raster scan of the phase object. In the following, each scans consists of $M \times N$ points, defining a surface Γ of the high frequencies phase modulating scanned object.

Performing such scans, one records image stacks defining a 4 dimensional signal, which is used for the recovery of the transfer function. Indeed, performing two similar raster scans, one with the sample in the beam, and the other without the sample, one obtains two sets of 2D data for each pixel: (k, l): g_{kl}^{samp} when the sample is in the beam; and g_{kl}^{ref} when the sample is removed (this is often referred to as the flat field reference).

The average intensity μ, the standard deviation σ and the energy ε collected in a recorded pattern g in a given pixel are defined by:

$$\begin{aligned} \mu &= \frac{1}{\Gamma}\int_{\Gamma} g = \tilde{g}(0,0) \\ \sigma &= \sqrt{\frac{1}{\Gamma}\int_{\Gamma}(g-\mu)^2} \\ \varepsilon^2 &= \sum_{-\infty}^{+\infty}|\tilde{g}|^2 = \int_{\Gamma}|g|^2 \end{aligned} \tag{7.6}$$

Absorption imaging

An absorption image is defined as the ratio of the number of photons falling on a pixel of the detector with and without the sample present in the X-ray beam. Retrieval of

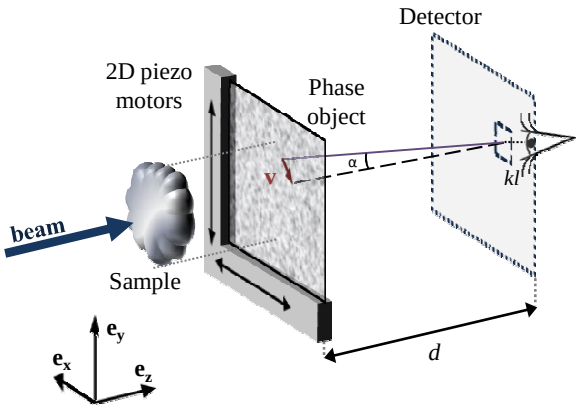

Figure 7.4: Schematic of a generalized stepping imaging setup. A phase object with small features is mounted on a 2D piezo motor beyond the sample, and a highly resolving detector is placed at a distance d. The 2D raster scans of the scattering object allows one to calculate the scattering vector v for each pixel when the sample is introduced into the beam.

the attenuation A image is calculated by taking the ratio of the energy collected in each pixel in the scans:

$$A(k,l) = 1 - \frac{\varepsilon_{kl}^{samp}}{\varepsilon_{kl}^{ref}} \tag{7.7}$$

Because the x rays are only partially coherent, most of the recorded signal comes from non-interfering, background light. Using the approximation $\varepsilon \approx \mu$, one can retrieve the formulae based on the use of the Fourier transformed signals:

$$\begin{aligned} A(k,l) \approx 1 - \frac{\mu_{samp}}{\mu_{ref}} &= 1 - \frac{|\tilde{g}_{kl}^{samp}(0,0)|}{|\tilde{g}_{kl}^{ref}(0,0)|} \\ &= 1 - |H(0,0)| \end{aligned} \tag{7.8}$$

Phase imaging

In the hard X-ray regime, due to the weak interaction of the photons with matter, deflection angles induced by the refraction are usually very small, i.e. much less than a degree. When an object is introduced into the X-ray beam, the propagation direction of the light will be slightly changed, and the speckle pattern recorded will be modified relative to its reference 'version' when no sample was present. This idea is the basis of many deflection angle technique such as the Hartmann sensor [62], the X-ray Speckle Tracking technique [137], or the XGI [90] in which wavefront gradients are measured through displacement of intensity modulation pattern. The deflection angle α is equal to the wavefront gradient $\alpha = |\nabla W|$, and the transverse local shift $\mathbf{v}$ of the pattern

will be equal to [73]:

$$\mathbf{v} = d.\nabla W = d\frac{\lambda}{2\pi}\nabla\varphi \tag{7.9}$$

where d is the propagation distance from the reference phase objet to the detector. Hence, the recovery of the shift $\mathbf{v}$ between recorded signals as shown in Fig. 7.4 can lead to the knowledge of α and the local beam phase.

Here, the recovery of $\mathbf{v}$ is achieved using Eq. 7.3 by separating the amplitude and phase of the transfer function H:

$$\tilde{g}_{kl}^{samp} = H_{kl}.\tilde{g}_{kl}^{ref} \quad = |H_{kl}|.\tilde{g}_{kl}^{ref}.e^{-i\delta\Phi_{kl}} \tag{7.10}$$

In this expression, the argument of H, $\delta\Phi(\xi,\nu) = \arg(H(\xi,\nu))$ is, according to the shift theorem, the delay between the two signals g^{ref} and g^{samp}. A traditional method to derive this phase component is to use the 2D cross-correlation operation with the two recorded signals. Dropping the pixel subscripts for the sake of clarity, and separating the orthogonal components of $\delta\Phi(\xi,\nu) = \delta\Phi_x(\xi) + \delta\Phi_y(\nu)$, we have:

$$\begin{aligned} g_{samp} \star g_{ref} &\Leftrightarrow \tilde{g}^*_{samp}.\tilde{g}_{ref} \\ &= |H(\xi,\nu)|.|\tilde{g}_{ref}(\xi,\nu)|^2 e^{-i(\delta\Phi_x(\xi)+\delta\Phi_y(\nu))} \end{aligned} \tag{7.11}$$

where $\star$ denotes the correlation operator, and $*$ the complex conjugate. Using the phase fn the exponential part of this last equation, one can deduce $\mathbf{v}$ using the shift theorem:

$$\mathbf{v} = \frac{\delta\Phi_x(\xi)}{2\pi\xi}\mathbf{e_x} + \frac{\delta\Phi_y(\nu)}{2\pi\nu}\mathbf{e_y} \tag{7.12}$$

And finally combining Eq. 7.9 and Eq. 7.12, one can calculate the beam phase gradient in the two orthogonal directions:

$$\begin{aligned} \frac{\partial\varphi}{\partial x} &= \frac{k}{d}(\mathbf{v}.\mathbf{e_x}) = \frac{k}{d}.\frac{\delta\Phi_x(\xi)}{2\pi\xi} \\ \frac{\partial\varphi}{\partial y} &= \frac{k}{d}(\mathbf{v}.\mathbf{e_y}) = \frac{k}{d}.\frac{\delta\Phi_y(\nu)}{2\pi\nu} \end{aligned} \tag{7.13}$$

where in this set of equations k stands for the wavenumber $k = 2\pi/\lambda$. In practice, for a better accuracy in Eq. 7.12, one uses the frequencies (ξ_{max}, ν_{max}) corresponding to the peak of maximum cross-spectral power $\max_{(\xi,\nu)>0}(|H(\xi,\nu)|.|\tilde{g}_{ref}(\xi,\nu)|^2)$. In Eq. 7.11, one can also note that $\delta\Phi = \Phi_{samp} - \Phi_{ref}$ with $\Phi_{samp} = \arg(\tilde{g}_{samp})$ and $\Phi_{ref} = \arg(\tilde{g}_{ref})$.

After calculating the local phase gradients for each pixel, the global reconstruction of

the beam phase can be performed by simultaneously integrating the two transverse gradient maps [130, 146].

Darkfield imaging

The darkfield image, sometimes called the scattering image, is a map of the local decrease of coherence of the beam induced by passing through the sample [134]. With the XGI, the variation of coherence in the section of the beam illuminating a given pixel is calculated by taking the ratio between the fringe amplitude of the sample scan and the reference scan, normalized by the absorption.

From a more general perspective, the partial beam coherence variation affects the amplitude of the interference created by the wavefront modulation pattern [5]. In other words, the coherence effect translates into the standard deviation of the recorded intensity pattern. Hence, to quantitatively map the coherence decrease C due to the sample scattering properties, one can calculate the ratio of the signal standard deviations between the two scans. Furthermore, this ratio has to be normalized by the absorption to account for the lower number of photons falling on the detector when the sample is inserted in the beam. The values of interest for the two signals are then the normalized standard deviation μ/σ, aka coefficient of variation, which leads to the expression of the scattering factor:

$$1 - C = \zeta_{kl} = \frac{\mu(g_{kl}^{ref})}{\mu(g_{kl}^{samp})} \frac{\sigma(g_{kl}^{samp})}{\sigma(g_{kl}^{ref})} \tag{7.14}$$

From the definition of σ in Eq.7.6 and dropping once again the subscript kl for the sake of clarity, one can write:

$$\begin{aligned} \zeta^2 &= \frac{\mu_{ref}^2}{\mu_{samp}^2} . \frac{\int g_{samp}^2 - \mu_{samp}^2}{\int g_{ref}^2 - \mu_{ref}^2} \\ &= \frac{\mu_{ref}^2}{\mu_{samp}^2} . \frac{\epsilon_{samp}^2 - \mu_{samp}^2}{\epsilon_{ref}^2 - \mu_{ref}^2} \end{aligned} \tag{7.15}$$

Measurement of the effective local wavefront curvature

It is sometimes necessary to know the effective second derivative of a wavefront beam, i.e its local curvature. From Eq. 7.5, the beam phase second derivative is responsible for the creation of interference in a coherent beam. While this phenomena is used in some propagation techniques sensitive to ΔW, for other applications it can lead to unwanted interference contrast or optical distortions.

As described for the X-ray speckle tracking related technique [137], one can identify different modes when working with near field speckle. A differential working concept has been described so far, which allows us to isolate the optical transfer function of the sample. Now, to recover the absolute second derivative one used the cross correlation operation between signals collected simultaneously in different pixels. This process has the advantage of not requiring a reference signal and then, when used as such, can be used to monitor the quality of a probing beam.

When performing a raster scan of a surface Γ of a membrane much larger than the pixel size of the detector, the patterns recorded in nearby pixels are very similar. Each pixel will see the same pattern but at different times, as depicted schematically in Fig. 7.5. If we consider a perfectly collimated beam (Fig. 7.5.(a)), the collected signals in two different pixel (k, l) and $(k + r, l + s)$ of size S_{pix} are connected by:

$$g_{k+r,l+s}(x, y) = \Upsilon_{kl}(r, s) g_{kl}(x - rS_{pix}, y - sS_{pix}) \tag{7.16}$$

where Υ accounts for the difference of both intensity and coherence in the probing beam at the position of the pixels. We choose to ignore this factor because it accounts for an amplitude modulation factor that does not distort the signal shape.

Similarly, for a non-collimated beam, with different local ray propagation directions, Eq. 7.16 becomes from Fig. 7.5.(b) with $\chi = \chi_x.\mathbf{e_x} + \chi_y.\mathbf{e_y}$ the delay between the signals recorded in the two different pixels:

$$g_{k+r,l+s}(x, y) = g_{kl}(x - \chi_x, y - \chi_y) \tag{7.17}$$

Expanding χ from Eq. 7.16 and using the Fourier shift theorem, we obtain:

$$\begin{aligned} \tilde{g}_{k+r,l+s} =& \tilde{g}_{kl}(\xi, \nu) \times e^{-i2\pi S_{pix}(\xi r + \nu s)} \\ & \times e^{-i2\pi(\xi(\chi_x - rS_{pix}) + \nu(\chi_y - sS_{pix}))} \end{aligned} \tag{7.18}$$

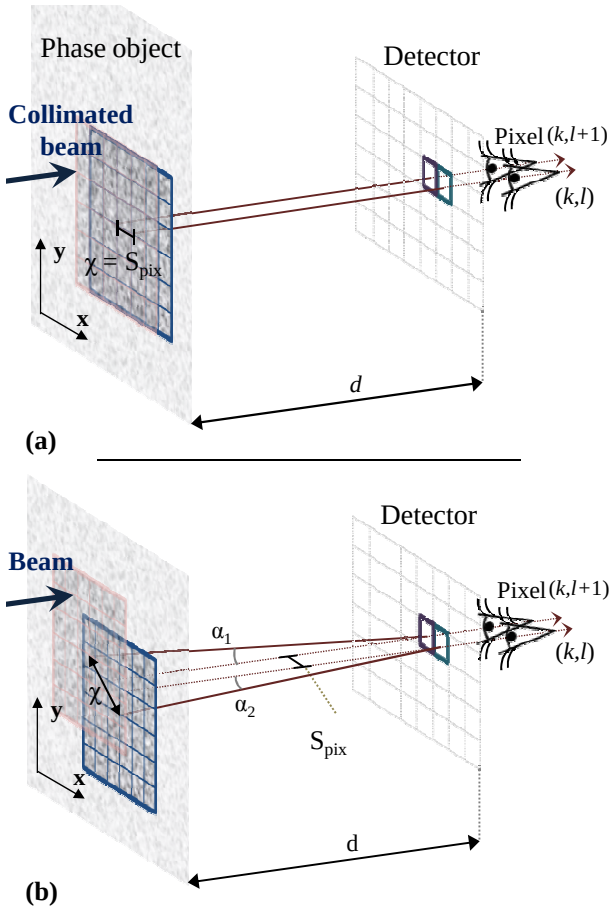

Figure 7.5: (a) The blue (dark gray) and the red (light gray) area on the phase object represent the pattern seen by two different pixels when scanning this object in a collimated X-ray beam: in this case the pixels are adjacent and $(r, s) = (1, 0)$. (b) A similar sketch for the case of a non collimated beam. The distance χ is defined as the offset between the similar part of the recorded pattern.

While the term in the first exponential matches the distance on the detector separating the considered pixels, the second is related to the local curvature of the beam. Indeed, as we have from Fig. 7.5.(b):

$$|\chi| = S_{pix}\sqrt{r^2 + s^2} + d.(\alpha_2 - \alpha_1) \tag{7.19}$$

Noting $\chi' = \chi - S_{pix}\sqrt{r^2 + s^2} = \chi - \delta S_{r,s}$ and as for small angles $|\nabla\alpha| = \nabla^2 W(x, y) \approx 1/R(x, y)$:

$$R \approx \left(\frac{\delta\alpha}{\delta S_{r,s}}\right)^{-1} \tag{7.20}$$

By projection on the transverse vectors $(\mathbf{e_x}, \mathbf{e_y})$, the orthogonal local radii are:

$$R_x \approx \frac{d.rS_{pix}}{\chi'_x} \quad , \quad R_y \approx \frac{d.sS_{pix}}{\chi'_y} \tag{7.21}$$

Thus, calculating the shift between signals collected in two nearby pixels, and using the cross correlation algorithm, one can recover the local second derivative of the beam. Compared to the X-ray speckle tracking technique in absolute mode, this new method is not limited by the magnification of the beam when the distortion of the speckle pattern between images becomes too large. This means that using this stepping mode, larger propagation distances d can be used, providing improved angular sensitivity.

The grating case

Grating interferometry is a special case of the technique presented here, where the random probing pattern is replaced with a well known and regular pattern, allowing simplified Fourier analysis [91, 89]. For instance, consider the case of the 2D gratings with pitches in the order of 2 to 8 microns for the first phase grating G1 [94]. Approximating the square profile of the grating lines to a sinusoidal shape, the intensity distribution of the pattern produced by the grating interferometer and recorded by the detector in pixel (k, l) can be approximated to:

$$g_{kl}(x, y) = B_1 \cos\left(\frac{2\pi}{P}x + \Phi_x\right) \times \cos\left(\frac{2\pi}{P}y + \Phi_y\right) + B_2 \tag{7.22}$$

with B_1, B_2, Φ_x, Φ_y and P some constants associated to each (k, l). From the transform defined by Eq. 7.4 :

$$\tilde{g}_{kl}(\xi, \nu) = \sum_{(p,q)\in[\![-1,0,1]\!]^2} a_{pq}\delta\left(\xi - \frac{p}{P}, \nu - \frac{q}{P}\right) \tag{7.23}$$

were δ denotes now the dirac distribution and where $a_{p,q}$ are complex numbers. One can also note that $a_{0,0} = \mu$. Hence for phase imaging, the cross-correlation operation of Eq. 7.11, reduces in Fourier space to:

$$\begin{aligned} g_{samp} \star g_{ref} \Leftrightarrow \tilde{g}^*_{samp} \cdot \tilde{g}_{ref} \\ = \sum_{(p,q)\in[\![-1,0,1]\!]^2} a^{ref}_{p,q} a^{samp}_{p,q} * \end{aligned} \tag{7.24}$$

Denoting $\Phi_x = \arg(a_{1,0})$, $\Phi_y = \arg(a_{0,1})$, the two components of the transverse displacement of the projected pattern with respect to the reference are:

$$\begin{aligned} \mathbf{v}_x &= \frac{(\Phi^{samp}_x - \Phi^{ref}_x)}{2\pi} \times P \\ \mathbf{v}_y &= \frac{(\Phi^{samp}_y - \Phi^{ref}_y)}{2\pi} \times P \end{aligned} \tag{7.25}$$

Equation 7.25 is similar to Eq. 7.13 when using a single spatial frequency $\xi = \nu = \frac{1}{P}$. Finally, we retrieve the traditional general phase grating interferometer equation in the plane of G1 [94]:

$$\nabla\varphi \cdot \boldsymbol{e_{x/y}} = \frac{2\pi}{\lambda}\nabla W \cdot \boldsymbol{e_{x/y}} = \frac{P}{\lambda}\frac{(\Phi_{x/y}^{samp} - \Phi_{x/y}^{ref})}{d} \tag{7.26}$$

When using a second absorbing grating G2 with the same orientation as G1, and with a pitch P' very close to P, by the aliasing process, the frequencies of the fringes in one image are rescaled [74]. The superposition of the two patterns created by G1 and G2 generates a new pattern with a larger fringe period equal to $\frac{|P'-P|}{PP'}$, but does not affect the phase distortion induced by the beam. The use of a second grating is motivated by two advantages: it removes or simplifies the phase unwrapping process necessary when employing a single grating; and a detector with larger pixels can be used, enabling usually a larger field of view.

Concerning dark-field imaging with the grating interferometer, the application of formulae 7.15 to the spectrum of the patterns recorded with the XGI, directly leads to the directional scattering imaging formulae already present in the literature [94]:

$$\zeta_x = \frac{\mu_{ref}}{\mu_{samp}}\frac{|{a_{1,0}}^{samp}|}{|{a_{1,0}}^{ref}|} \quad , \quad \zeta_y = \frac{\mu_{ref}}{\mu_{samp}}\frac{|{a_{0,1}}^{samp}|}{|{a_{0,1}}^{ref}|} \tag{7.27}$$

and equivalently for the diagonal directions.

Spatial resolution and sensitivity limitations

When using a grating interferometer combined with a high resolving detector, the spatial resolution of the device is limited by the shear distance [91, 133]. It is defined, in the plane of G1, by the distance separating two photons interfering in the plane of the detector. In near field speckle, because all the spatial frequencies of the spectrum contribute to the phase contrast, with an energy transmission predominance in the lower frequencies, the shear effect does not become a limitation when working with random patterns [117]. While the contrast from a phase grating is obtained through the interferences of the zeroth and first diffraction orders, for near field speckle the contrast is instead obtained from the self interference scheme [24]. The spatial resolution of the proposed method is then limited by the detector.

However, higher derivatives of the wavefront can also have an effect on the spatial

resolution of the system. As showed in Fig. 7.4, the measured angle α of the technique is defined in the plane of the detector. So, when the wavefront gradient is strong, the vector $\mathbf{v}$ becomes larger than a detector pixel and limits the local spatial resolution. While a short distance d avoids a large vector $\mathbf{v}$, it can also affect the wavefront phase sensitivity. One solution to this resolution limitation is to scan the detector instead of the membrane, which requires high-resolution, heavy-duty motion stages. Such a method would actually be an over-sampled version of the XST technique [137] where the quantity measured is equivalent to the one obtain with the Hartmann sensor.

The choice of the average speckle grain size is not strict providing that the detector can resolve the features: it only has a small influence on the accuracy of the cross-correlation algorithms that are employed [127]. In any case, various scattering membranes made of small phase objects are commercially available, for instance as biological filters.

Concerning the angular sensitivity $\delta\theta$ of the deflection measurement, it varies with d and with the smallest measurable vector $\mathbf{v}$. Denoting S_{scan} as the piezo scan step, and δs as the sub-step accuracy achievable in the cross-correlation process, the angular sensitivity is $\delta\theta = \delta s S_{scan}/d$. This relation shows that one can optimize the sensitivity of the method either using a larger propagation distance and/or recording images within scans of smaller steps.

Nevertheless, if one opts for diminishing the scanning step size or increasing its number, it should be kept in mind that the number of recorded images increases at a square law rate, equivalently to the 2D XGI. An alternative to this 2D scan image number increase is that when the propagation distance or expected deflection of the wavefront is small, one can use the stepping scheme by performing only two orthogonal scans as with a 1D XGI [147]. This approximation has shown good efficiency when the pattern shift is a fraction of the speckle grain size. The rate of increase law makes the 1D grating interferometer of great interest. Indeed, such a device projects and separates the 2D gradient onto two orthogonal components, rendering the required image number law increasing at a $\mathcal{O}(2n)$ rate. This law should be compared to the $\mathcal{O}(n^2)$ images law necessary with the 2D XGI or the presented generalized scheme when increasing the steps number for noise robustness and accuracy.

7.2.3 Experimental Application

A set of experiments were performed at the Test beamline B16 at Diamond Light Source where the X-ray are produced by a bending magnet on the 3 GeV storage ring [26].

Numerical implementation aspects

The numerical implementation of the theory described in this paper is a straightforward translation of the equations to discrete space: well known numerical recipes have been used for the implementation of the technique on a standard desktop computer. Considering each pixel (k, l) independently, the intensity signal collected during the scan will describe a 2D pattern $g_{kl}(x_m = mS_x, y_n = nS_y)$ with $(m, n) \in [\![0, M-1]\!] \times [\![0, N-1]\!]$ and (S_x, S_y) are the piezo motor scan steps in the two transverse directions. The calculation of the signal delay described by Eq. 7.11, necessary for the calculation of the beam local phase shift, can be performed either in real space or Fourier space. In Fourier space, discrete Fourier transforms are typically performed using the Fast Fourier Transform algorithm which significantly reduces the number of operations and thereby the calculation time. Spectral leakage that can arise from the transformation can be reduced by previous zero padding of g. This signal can be then expressed from its 2D Fourier series:

$$g(x_m, y_n) = \frac{1}{MN} \sum_{p,q=0}^{M-1,N-1} a_{p,q} e^{\left[i2\pi\left(\frac{pm}{M}+\frac{qn}{N}\right)\right]} \tag{7.28}$$

and the corresponding arguments of $a_{p,q}$ can be used for the recovery of the phase, as with the XGI. However, it can be more interesting to perform the operation described by Eq. 7.11 in the real space, with sub-step accuracy [127]. This processing method becomes of particular interest when the wavefront gradient is strong, because it allows one to avoid the unwrapping process that can sometimes become problematic.

Setup

A double multilayer monochromator, located 22 meters from the source, was used to select x rays of an energy $E = 15\ keV (\Delta E/E \approx 10^{-2})$ which illuminated samples located at a distance of 50 m from the source. Samples were mounted on a multi-

translation and rotation station that allowed easy alignment and removal from the X–ray beam. Another stage on the optics table had several biological filtering membranes mounted on it. Membranes were fixed on a two dimensional translation piezo motor capable of displacements with nanometer accuracy. Finally, the last stage of the optics table was occupied by the detector. The camera was a CCD detector imaging an X-ray scintillator through a microscope objective, resulting in a pixel size of 0.9 μm. Care was taken to ensure that the resolution of the detector was sufficient to resolve the speckle features in each image. A schematic of the experiment is shown in Fig. 7.4.

Characterization of a 2D CRL

Differential wavefront slope

The technique described in Sec. 7.2.2 was first applied to the characterization of a 2D compound refractive lens (CRL) to evaluate the quantitative accuracy of the method and for comparison [148, 95]. The CRL under test was a single Be refractive lens with an ellipsoidal shape and a design radius at the apex of $R = 200\ \mu m$. The theoretical focal length $f = R/2\delta$ of this lens is 66 m [6]. Two orthogonal wavefront gradients induced by the CRL were derived using two sets of 16x16 images acquired while scanning a cellulose acetate membrane of 1 μm size pores. The results are shown in Fig. 7.6. The focal lengths derived from the measurements are 65.98 m in the vertical, and 64.87 m in the horizontal plane. While there is very good agreement with the theoretical value in the vertical plane, the values differ by 1.5% in the horizontal. Whilst considering if such level of error is acceptable, one should remember that the bandwidth of the monochromator was of $\sim 2\%$.

In Fig. 7.6, one can see that no speckle pattern is present in the wavefront gradient maps, as they are only used as information carrier.

Absolute wavefront curvature

To illustrate the efficiency of the method explained in section 7.2.2, the local radius of curvature of the beam after passing through the Be CRL is plotted in Fig. 7.7. Despite the high quality of the lens, the wavefront slope of the transmitted beam is not monotonous due to imperfections in the incoming beam, especially in the vertical direction where phase defects from the multilayer monochromator are visible. These results show the feasibility and validity of the method as a quantitative absolute wave-

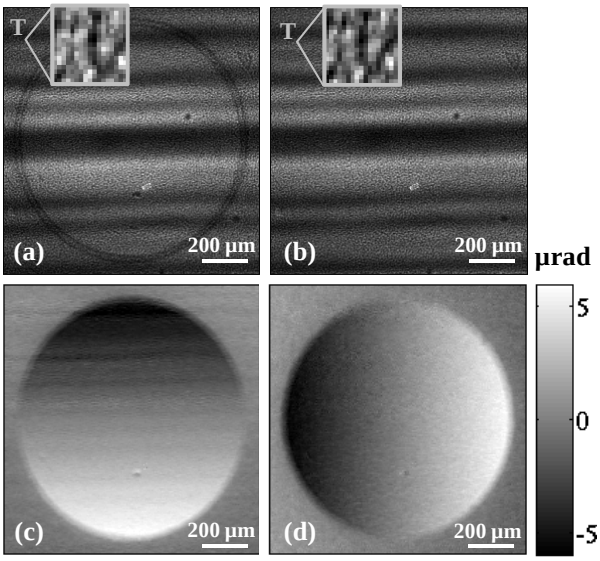

Figure 7.6: Differential characterization of a 2D CRL. (a)-(b) First image of the scan respectively with and without the sample inserted in the beam. The bounded squares show the patterns recorded in each of the scan in the pixel marked T. (c) Horizontal and (d) vertical differential wavefront slopes.

front measuring tool, which could be used for metrology purposes.

Imaging of a feather

As a 'real' sample illustration case, the three modal imaging of a bird feather was performed using this technique. The setup was identical to that employed for the characterization of the CRL in section 7.2.3. The propagation distance remained at $d = 520$ mm. Two raster scans of 32x32 images were recorded, moving a scattering membrane made of cellulose acetate with 1 μm pore size. Absorption, phase and scattering images were retrieved from the collected data and the results are displayed in Fig. 7.8. From the small visible details, one can get an idea of the spatial resolution of the system (pixel size = 0.9 μm) and the fine sensitivity of the method for phase contrast imaging.

7.2.4 Conclusion and Perspectives

We have demonstrated, theoretically and experimentally, the extension of the three modal imaging scheme from a grating interferometer to a more generalized method that allows the use of any phase objects. The grating case has been showed to be a special case of this general scheme. The proposed technique offers better spatial resolution

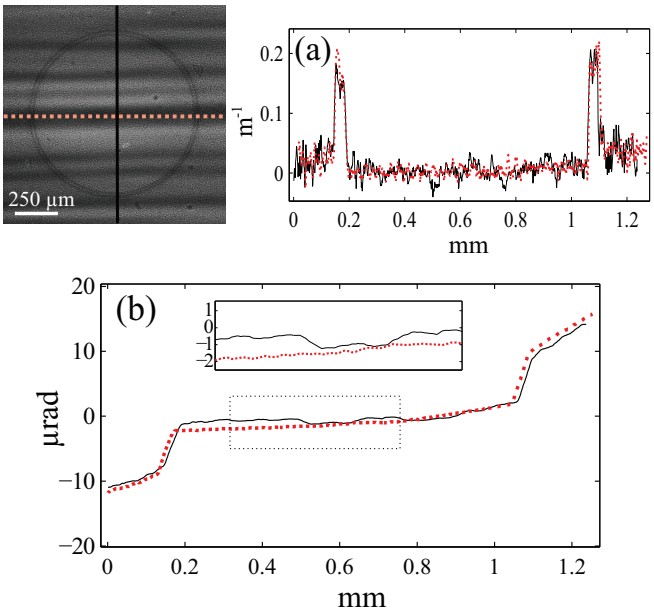

Figure 7.7: (a) Effective second derivative of the X-ray beam wavefront after propagation through the CRL. (b) Effective wavefront slope obtained by integrating the measured beam's second derivative. The inset shows the effect of the multilayer monochromator phase errors on the amplitude of the fringes. The dashed and plain lines show respectively an horizontal and a vertical cut across the CRL.

compared to the XGI, and does not require an X-ray grating, which can be expensive and difficult to purchase for high energy experiments. However, as previously exposed, the XGI and notably the 1D case, still offers noticeable advantages such as a smaller number of required exposures and a capability to work with a larger field of view.

As a future development, one can already think about using the method in a magnifying geometry to access nanometer resolutions. Indeed, as one can find grains of any size to generate speckle, the achievable resolution when using a magnifying optic is expected to be pushed down near the diffraction limit. In parallel, the advantage of this technique is that it can be used for very strong gradients, as the unwrapping process can be totally avoided by performing cross correlation in real space. Another idea is to replace the phase object that generates the speckle by a statistical absorption object in order to use the technique with a totally incoherent X-ray beam. We expect that this technique find many applications for micro phase contrast imaging and can be soon exploited in a tomography process to render 3D object.

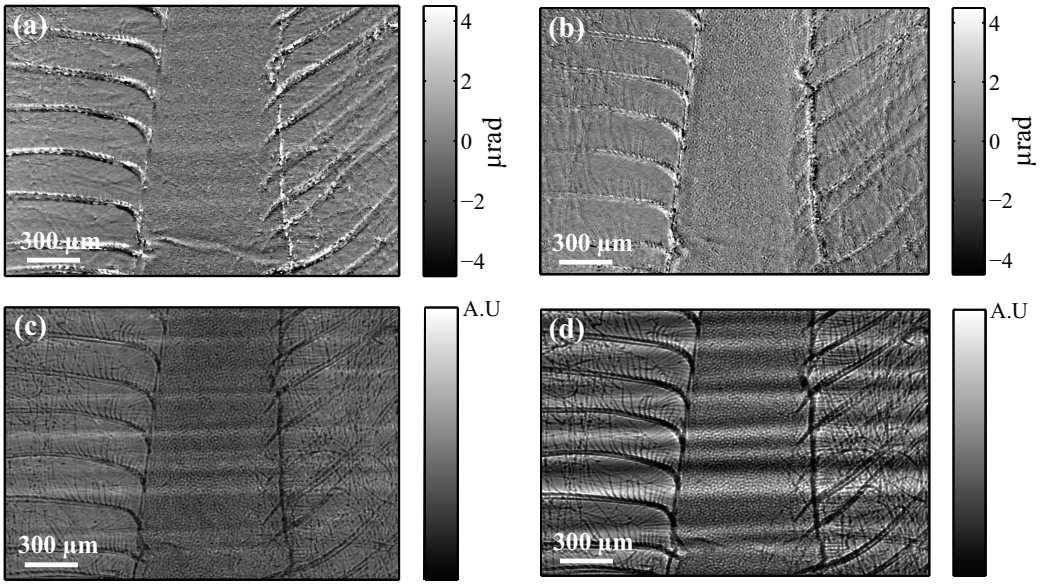

Figure 7.8: (a) Vertical and (b) horizontal differential wavefront gradients. (c) Scattering image. (d) Absorption image. One can see in the absorption and scattering images horizontal stripes due to the multilayer monochromator instabilities.

8 Advanced deflectometry with gratings

8.1 Introductory remarks

The next section is a reprint of the paper entitled Grating based at-wavelength metrology of hard X-ray reflective optics published in the *Optics Letters*.

The technique presented herein relies on the deflectometry principle employed for 3D mapping with visible optics for quite a long time [149, 150]. These techniques have been deeply investigated and enhanced in the 80's thanks to the expansion of modern computing [151, 152, 88, 153, 154, 155, 156]. Their principle is based on the projection of fringe patterns with gratings, to measure through Moiré fringes analysis, the angle of deflection induced in an optical system. Many of these schemes and algorithms are today routinely used to characterize optics but also to map 3D objects [74, 73].

When implementing such technique on X-ray reflective optics, the main difficulty lies in the grazing incidence that must be used to obtain the total reflection of X-rays on the surface. Likewise, X-ray grating manufacturing is a technical challenge, especially for absorption gratings. For the experimental technique presented in the next section, an absorption grating with grooves filled with nickel was employed: the quality of the deposition is much better with such lighter elements than with, for instance, gold leading to the generation of better quality fringe patterns.

The measured quantity with the following method is comparable to the one obtained with LTP instruments, i.e. the tangential slope. Similarly the sagittal slope is not accessible. Though, the measured mirror focuses photons in only one dimension, the presented online method can provide the 2D map of the tangential mirror gradient.

While, in theory, the method is expected to give access to better spatial resolution and sensitivity, one can still question the several micro-radians discrepancy between the LTP and online measurements. This actually underlines the need in online metrology for an efficient temperature stabilization system and a non strained mounting, equivalently to what can be found in metrology labs.

8.2 Third paper

Grating based at-wavelength metrology of hard X-ray reflective optics

Authors: *Sebastien Berujon and Eric Ziegler*

A mean of characterizing the tangential shape of a hard X-ray mirror is presented. Derived from a group of methods operating under visible light, its application in the X-ray domain using an X-ray absorption grating allows recovery of the mirror shape with nanometer accuracy and sub-millimeter spatial resolution. The method works with incoherent light, does not require any a priori information about the mirror characteristics and allows shape reconstruction of X-ray reflective optics under thermal and mechanical working conditions.

Metrology techniques and instruments capable of characterizing hard X-ray optics are of paramount importance in the development of optics operating at the diffraction limit needed to image matter at the nanoscale [157]. Indeed, with a wavelength four orders of magnitude smaller than the one of visible light, an aberration-free wavefront calls for an optics with a quality enhanced by the same order of magnitude, and, for the development of a metrology method capable of characterizing such optical surfaces. Metrology is usually performed with visible light using instruments such as long trace profilers (LTP) and interferometers [43]. Nevertheless, in the production of hard X rays nanofocusing optics, information on the effective performance of the optics can only be provided by at-wavelength metrology techniques [158, 159, 160]. Various techniques have been proposed for the online characterization of reflective surfaces, based so far either on coherent iterative methods [161] or derived from measurements of the wavefront gradient [91] to accurately determine the beam phase error after mirror reflection. However, for a professional in mirror surfacing, direct information on the distribution of surface slopes as provided by the laboratory instruments, remains the

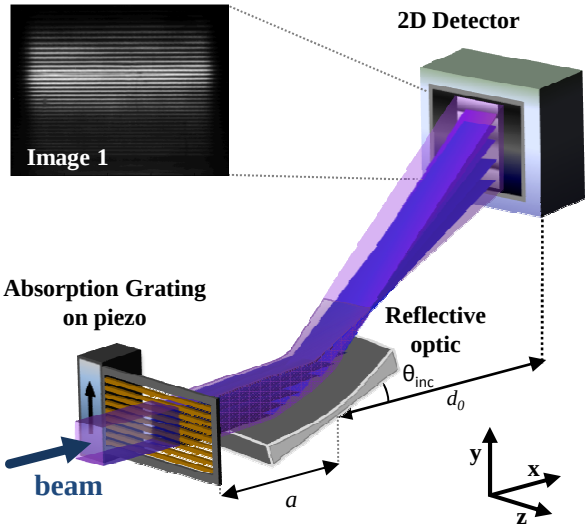

Figure 8.1: Sketch of the experiment. An absorption grating is placed at a short distance a from the mirror while an imaging detector is placed upstream at $d_0 \gg L$. An example image of the structured light produced by the grating after reflection on a mirror is also displayed.

most pertinent quantity of interest for improving X-ray optics.

Here, we propose an improved version of the moiré deflectometry techniques first described by Kafri in the 80's [151, 152, 162] and largely investigated, developed and used since then [153, 163, 164]. To our knowledge, despite the fact that wavefront metrology is often performed at various synchrotrons using grating interferometer [91], no surface mapping method has ever been presented in the hard X-ray regime. The technique presented uses an X-ray absorption grating complemented by some basic considerations on X-ray deflection techniques [47] further enhanced using specific mathematical treatments. The method provides access to the tangential slope of the surface with a sub-millimeter sampling resolution, i.e. one order of magnitude better than instruments such as LTP. Moreover, it is applicable in the case of strongly focusing optics. The technique was demonstrated during an experiment at the ESRF beamline BM05.

The setup used is sketched in Fig. 12.1. The investigated reflective optics was aligned into the X-ray beam at a distance $R = 40.6$ m from the bending magnet source. For our experiment, the sample under study was an uncooled silicon mirror produced by the *Zeiss* company with a length $L = 50$ mm and a strongly focusing shape ($f = 60$ mm). The incidence angle Θ_{inc} was precisely calibrated using the X-ray beam with $\Theta_{inc} = 0$ when the optical surface has its two longitudinal edges aligned with the photons propagation direction. To use the total external reflection effect of the X-rays on the silicon, the mirror was then tilted by a few milliradians. A 2D CCD detector with indirect illumination and a pixel size $S_{pix} = 5.8$ μm was placed at a distance

$d_0 = 807$ mm, i.e much further downstream the optics focal plane. Choosing a large distance d_0 optimizes the sensitivity to the measured deflection angles. In the case of a focusing optics, the sampling resolution also substantially increases with this distance, thanks to a magnification effect. An X-ray absorption grating was mounted on a piezo-electric driven translation stage in front of the reflective optics. The constant-space grating was realized in a silicon wafer by soft X-ray lithography [85]. The grating lines were spaced with a pitch $p = 4.8$ μm and the grooves filled with Nickel for absorption. More generally, the grating pitch must be adapted to get a resolvable pattern in the plane of the detector: a too small pitch will lead to an unresolved moiré pattern while a large pitch will decrease the angular sensitivity of the device. Although diffraction would make a negligible background noise, it was set to a minimum by minimizing the distance a. For our experiment, the photon energy was set to a value of 12 keV using a double multilayer monochromator. In this case the relative energy bandwidth was of a few percents. However, as the method uses incoherent light, a modification of the bandwidth would not affect the result, but only the intensity level at the detector.

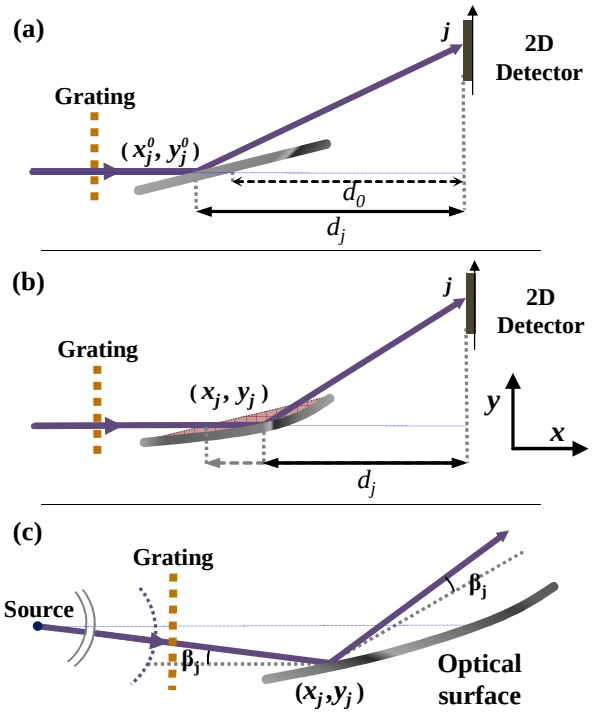

Figure 8.2: Geometrical considerations.

The grating was scanned using the piezo actuator in the direction perpendicular to the grating lines and an image was recorded for each position of the grating. A stack of 64 images was generated over a scan length five times longer than the grating period. Because the grating used was constant along the z axis direction, the problem was considered invariant along the mirror sagittal direction and restricted to the two dimensional plane defined by the basis $(\mathbf{x}, \mathbf{y})$ having its origin attached to the mirror surface center. The phase Φ_j of the projected fringes was then recovered for each detector pixel of row j using the method explained in Ref. [89].

The mathematical retrieval of the mirror slope was done iteratively. Given that no a priori knowledge about the mirror shape is provided to the method, the first step of the profile recovery is made on the initial assumption that the surface is flat, as displayed

in Fig. 8.2.(a). In this first approximation, the height and abscissa positions of a point on the mirror surface would be then linearly linked. This means that before falling onto a detector pixel of row j, any photon that crossed the grating was reflected at a point of the optical surface having a height y_j and an abscissa x_j^0. These coordinates are respectively equal to:

$$y_j = \frac{\Phi(j)}{2\pi} p \quad \text{and} \quad x_j^0 = \frac{\Phi(j)}{2\pi} \frac{p}{\tan(\Theta_{inc})} \tag{8.1}$$

From these two relations, the surface slope at a given point is calculated, in the approximation of the small X-ray angles involved, with [47]:

$$Sl_0(x_j^0) = \frac{1}{2} \frac{Y_j^{det} - y_j}{d_0 - x_j^0} \tag{8.2}$$

where $Y_j^{det} = j \times S_{pix} + \vartheta$, the height position of the pixel in row j on the detector with $\vartheta = 2d_0 \cdot \Theta_{inc}$.

So far, the mathematical relation 8.2 can be compared to the one of the pencil beam technique [47]. However, as it does not take the curvature of the mirror into account, our method uses an additional iterative step to correct for the error this approximation induced. The approach is illustrated in Fig. 8.2.(b). In first approximation, it was considered that a ray with a height y_j falls on the surface at a position $x_j = y_j / \tan(\Theta_{inc})$. In reality, the ray also travels across the area colored in red before hitting the optical surface. This red area corresponds to the contribution of the curved surface as compared to a flat one. When working at grazing incidence with hard X rays, this contribution corresponds to an error on the abscissa location of many millimeters for an optics with a sag of a few tens of micrometers.

The proposed iterative step of our method solves this issue using a fixed point method in which the mirror slope $Sl_n(x_j)$ of iteration n is calculated using:

$$Sl_{n+1}(x_j^{n+1}) = \frac{1}{2} \frac{Y_j^{det} - y_j}{(d_0 - x_j^{n+1})} \tag{8.3}$$

where x^{n+1} is obtained through the inversion of the height mirror function h_{n+1} assumed to increase monotonically and calculated with the previous slope:

$$h_{n+1}(x) = \int_0^x Sl_n(X)\, dX \Rightarrow x_j^{n+1} = h_{n+1}^{-1}(y_j) \tag{8.4}$$

From the Banach fixed point theorem, the convergence of the method to the true position of x_j is ensured if the iterative function h_{n+1} is k-Lipschitz with $k < 1$ [165]. This translates into the hypothesis conditions that the mirror shape is defined by a continuous function and its derivative, i.e its slope, majored by k. However, because the mirror reflection of the hard X-ray photons operates only at grazing incidence angle, this last condition will always be satisfied.

Lastly, the divergence of the incoming probe beam has to be considered and accounted for. In this aim, the wavefront at the grating plane is assumed to be spherical with a radius R: considering the small aperture of the optical system < 0.3 mm and the low optical aberrations of the beam provided by a third generation synchrotron X-ray beamline, this assumption corresponds to an error below 0.1 μrad. Hence, the beam wavefront W at the grating plane has a tangential slope $\nabla W \cdot \boldsymbol{y} \approx y/R$. As shown in Fig. 8.2.(c), the calculated mirror slope $Sl_{calc}(x_j)$ has then to be corrected by the quantity $Sl_{corr} = y_j/R$ for each calculated point and iteration n.

The mirror total slope profile was calculated and the slope error profiles from the perfect ellipse defined by the parameters ($p = 51.59$ m, $q = 59$ mm, $\theta = 6.31$ mrad) derived from scans recorded at different grazing incidence angles are plotted in Fig. 8.3. For comparison, the mirror profile derived from measurements acquired with a classical LTP [43] metrology instrument is displayed.

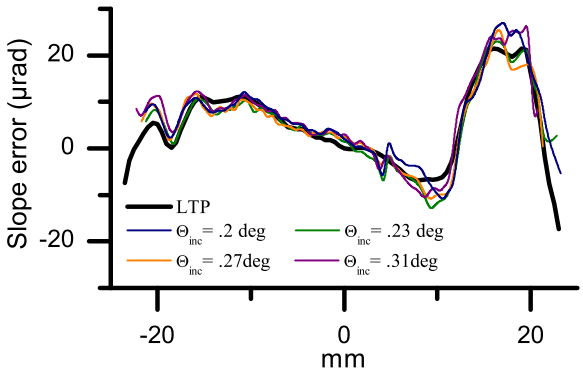

Figure 8.3: Mirror slope error measured with LTP and X-ray grating profilometry for different incidence angles.

The deviation between the LTP and the online measurements does not exceed few microradians for any of the measured cases: this small amount already confirms the very good agreement of our method with the metrology laboratory tools, while further comparison has to be tempered by the measuring conditions. Indeed several parameters may affect the measured data such as the thermal, mechanical stability (mirror clamping) or the footprint of the LTP probe beam (≈ 3 mm). The largest deviations,

observed on the mirror borders, may be due to edges diffraction effects and to a lower reflected photons flux resulting from higher incidence angle values on the mirror focus side.

The theoretical sensitivity δ_{Sl} of this geometrical method depends on the propagation distance, the grating pitch as well as the sensitivity of the phase recovery method and $\delta_{Sl} = (\Phi_{min}.p)/d_0$. Some work [89] demonstrated that the phase Φ_{min} can be recovered with an accuracy better than one hundredth of a period, leading in our case to a sensitivity below 60 nrad. However, the slope error profiles obtained from measurements performed at different incidence angles differed by $\sim$ 2.6 μrad rms while it is less than 1 μrad rms for the central part of the mirror. This discrepancy can be partially attributed to the varying thermal load when the incidence angle is getting higher. Due to space constraints, the propagation distance was limited to $d_0 = 807$ mm. However, enlarging this distance would improve both sampling resolution and sensitivity.

It is important to recall that the presented technique does not put any requirement on the coherence properties of the X-ray source, since the contrast of the recorded moiré fringes is only due to the use of the *zeroth* diffraction order of the grating.

In conclusion, we expect the X-ray moiré deflectometry technique to be used for accurate online mirror characterization. Using the present experimental stage, the sensitivity is comparable to the one provided by light metrology instruments, with the additional advantage of a better sampling resolution and the possibility of optics characterization under working conditions. This technique will open up perspectives, for instance, in the optimization of adaptive optics or correction of reflective optics.

Part III

Applications

9 Transmission optics characterization

In this chapter are described some applications of the previously presented methods for the characterization of diffractive and refractive transmission optics.

9.1 2D CRL characterization with XST and XGI

This section is based on some work published in the *Journal of Physics: Conference Series* as contribution to the conference on Synchrotron Radiation Instrumentation held in 2012 in Lyon.

Authors: *Sebastien Berujon, Hongchang Wang and Kawal Sawhney*

We describe here the characterization of a two dimensional focusing compound refractive lens (CRL). The characterization was performed by both XST and XGI techniques in equivalent configurations and the results were compared.

The CRL was made of Beryllium and had a parabolic shape with a design radius of curvature R = 200 μm at the apex. The CRL, the metrology components (grating or membrane) and the detector were mounted on the three different motorized stations of the B16 versatile table, allowing for each one, six degrees of freedom. The detector used was based on a PCO 4000 camera. Because the measurement of the displacement vector ν depends directly on the detector sampling grid, the effective pixel size was accurately measured as $P_{ix} = 0.9$ μm. The membrane used was made of cellulose nitrate with a pore size of $\sim$ 5 μm size. The distance between the membrane and the detector, as schematically shown in Fig. 9.1, was chosen to be $\delta l = 455$ mm. The

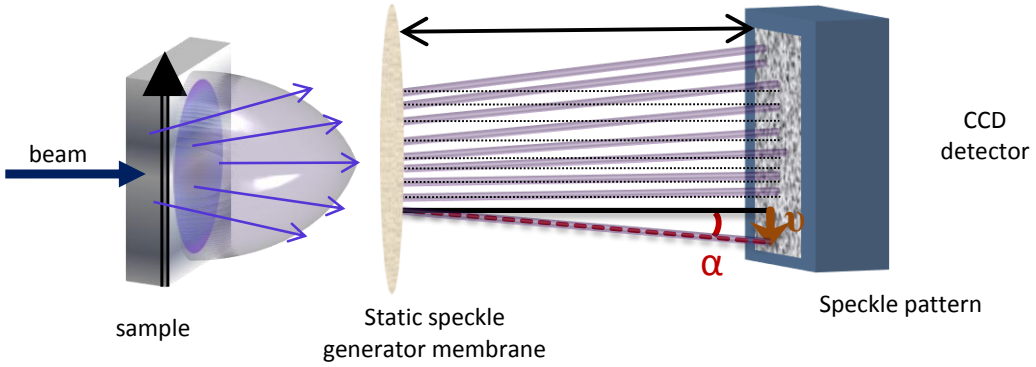

Figure 9.1: Sketch of the 2D CRL characterization principle.

beam energy was set to 15 keV using the Si 111 double crystal monochromator of the beamline. It was possible to remove the CRL out of the beam to measure the influence of the beamline optics on the wavefront.

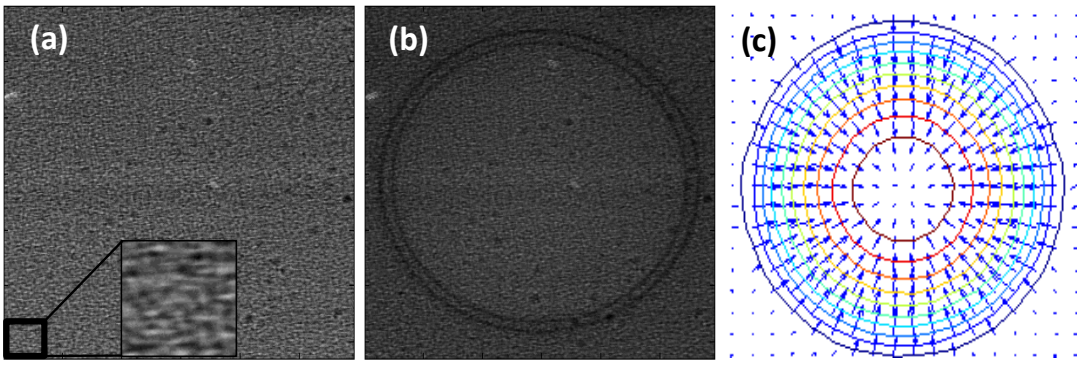

Figure 9.2: (a) Reference image with a zoom of a small area of speckle pattern. (b) Sample image. (c) Displacement vector field plot.

The XST technique was applied by recording two images, with and without the CRL in the beam (see Fig. 9.2 (a) and (b)). A sub-pixel accuracy zero normalized cross-correlation algorithm was then employed to calculate the displacement vector for each pixel from the two images of size 1200x1200 pixels (see Fig. 9.2 (c)). The wavefront gradient and the wavefront were calculated using the method described in 6.2.2. The reconstructed wavefront is shown in Fig. 9.3.(a) and the vertical central line of the wavefront gradient is displayed in Fig. 9.3.(b). For comparison, the wavefront distortion was also measured using a 1D grating interferometer. The methodology employed for the CRL characterization is similar to the one described in [95, 148]. In this experiment, two sequential phase stepping scans to measure the gradient in the two orthogonal directions transverse to the beam were performed in exactly the

same equivalent configuration as when performing the XST technique. The integrating distance was set to the 7th Talbot order of phase grating (π phase shift) with 4 μm pitch. The measured wavefront gradient of the vertical central line derived by the XGI technique is also displayed in Fig. 9.3.(b) for comparison.

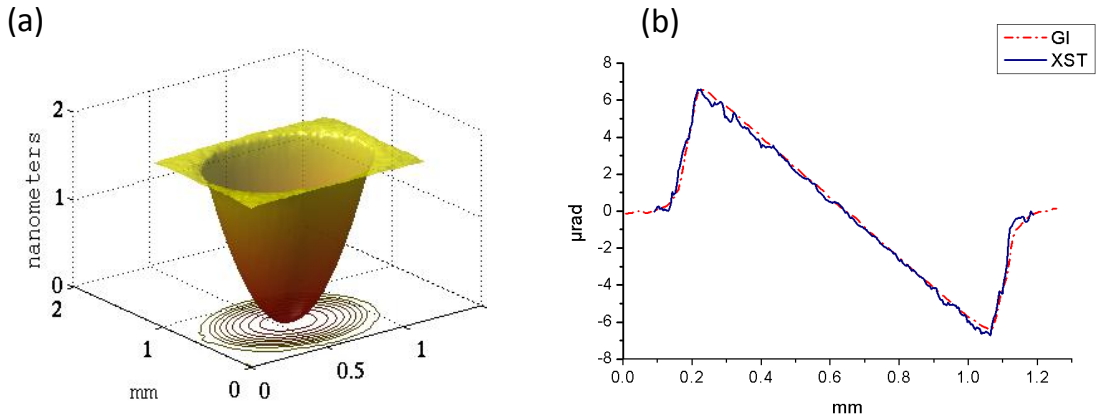

Figure 9.3: (a) Wavefront reconstruction from XST data. (b) Wavefront gradient measured with the grating interferometer and with the XST technique.

The results from XGI and XST techniques agree well with each other. The radius of curvature of the lens at the apex was calculated to be of 195 μm using linear fitting from XST data, which is close to the theoretical value of 200 μm. Using the above experimental parameters, the angular sensitivity of the XST method is expected to be: $S_\alpha = \frac{\epsilon_{CC} P_{ix}}{\delta l} = 60$ $n$rad when taking the cross-correlation algorithm accuracy ϵ_{CC} as equal to 0.03 pixel, which is more than reasonable. This sensitivity is corroborated by the standard deviation value of the wavefront gradient in an area of known constant phase which was below 45 $n$rad. Considering the micrometer size spatial resolution, this corresponds to a wavefront accuracy better than $\lambda/100$. Because of the experimental constraints, the distance Δl was chosen as equal to 455 mm, but an increase of this distance would further improve the angular sensitivity. The sharpness of the features of the XST measurements compared to the XGI data is due to the higher spatial resolution of the method; working at the 7th Talbor order with the XGI, the spatial resolution is of $\sim$ 14 μm, while the sampling rate of the XST technique is in the order of a few micrometers.

9.2 1D CRL characterization with XST

Mono dimensional Beryllium focusing lenses have recently become available from Lengeler *et al.* [31, 166]. Prototype lenses manufactured for NSLS-II, Brookhaven were tested at Diamond beamline B16. The experiment aimed at evaluating the possibility of correcting beam astigmatism by rotating the lens along the Ω axis (vertical axis for vertical focusing lens), as shown in Fig. 9.4. The lens characterization was done using both the XGI [167] and the XST technique in differential mode presented here.

The CRL had a radius of curvature at the apex of $R = 500\ \mu$m, rendering a focal length of $f = \dfrac{R}{2\delta_{Be}} = 165$ m at the used energy of $E = 15$ keV ($\Delta E/E \sim 10^{-4}$). The CRL was mounted on the optics table of the beamline experimental hutch and a speckle membrane was placed at a short distance from it. The PCO 4000 camera was then used to record the speckle images when the CRL was removed out of the beam path, and, when the CRL was inserted into the beam with various orientation angles Ω. The CRL focal length was calculated from the extracted wavefront gradient derived with XST for each rotation angle, and the values fitted to a sinusoidal function as shown in Fig. 9.4. The goodness of the fit confirms the validity of the model. The results show that a fine tuning of the astigmatism can be performed by ajusting the orientation angle of the 1D-CRL with respect to the incident beam. Such compensation is of great interest when focusing beams from non stigmatic beams or optics.

9.3 Replacement of a beryllium window

During the ESRF shutdown in the winter of 2011, a beryllium window of the BM05 beamline was replaced by a new one. This beryllium strip is located at the exit of the optics hutch to separate the parts of the beamline operated under vacuum and helium. The previous one had been in place for more than 10 years and had been subject to a high intense X-ray dose, which might then have damaged its original quality.

The opportunity was taken to measure the wavefront before and after the window replacement to evaluate the effect of this replacement especially on the wavefront low spatial frequencies. For this, the XST technique in the absolute mode was applied in equivalent conditions before and after the window replacement. The calculated

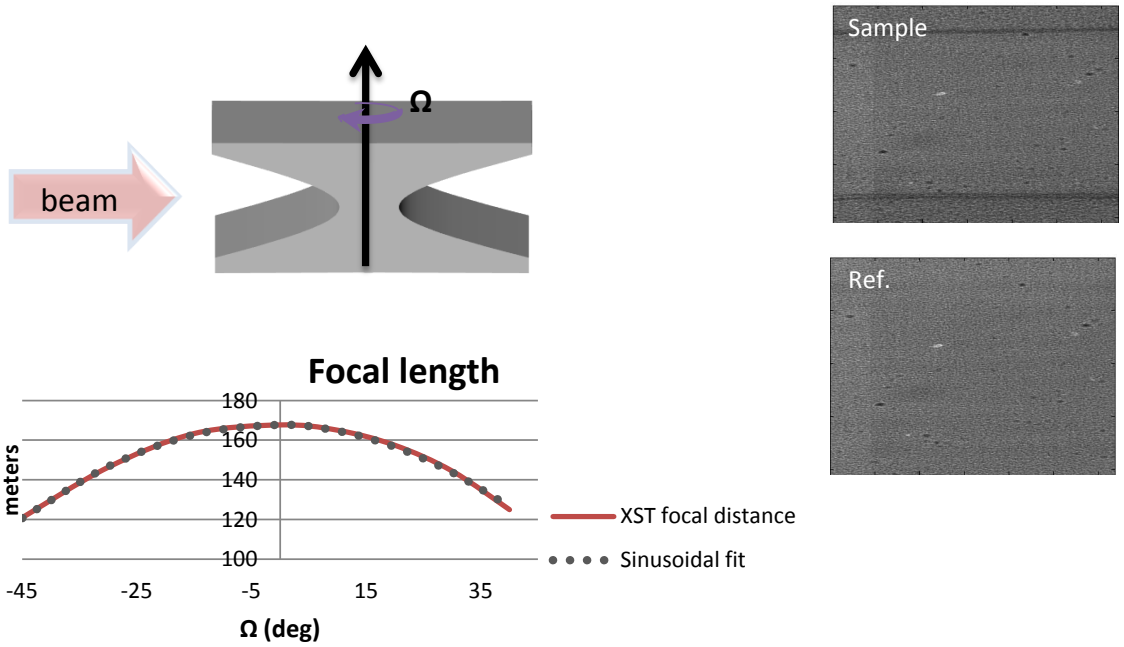

Figure 9.4: XST measurement of the astigmatism generated by a 1D CRL. On the left side are displayed two images used in the XST technique: the top one is an image with the lens inserted in the beam path whilst the bottom one is the reference beam.

wavefront distortions are shown in Fig. 9.5.

One can observe that the wavefront distortion amplitudes are equivalent in both measurements. In addition, the same general shape is recognizable, suggesting that this replacement did not significantly improve the large spatial wavelength aberration.

Because the interaction of the hard x rays with matter is small, i.e. $\delta \approx 10^{-6}$, several micrometers of matter are necessary to induce a phase shift of 2π radians in transmission making the windows unlikely to create large optical aberration. However at a much smaller scale, the polishing and homogeneity quality of the beryllium strip plays an important role in the diffuse scattering behavior of the optics and can be responsible for strong coherence degradation.

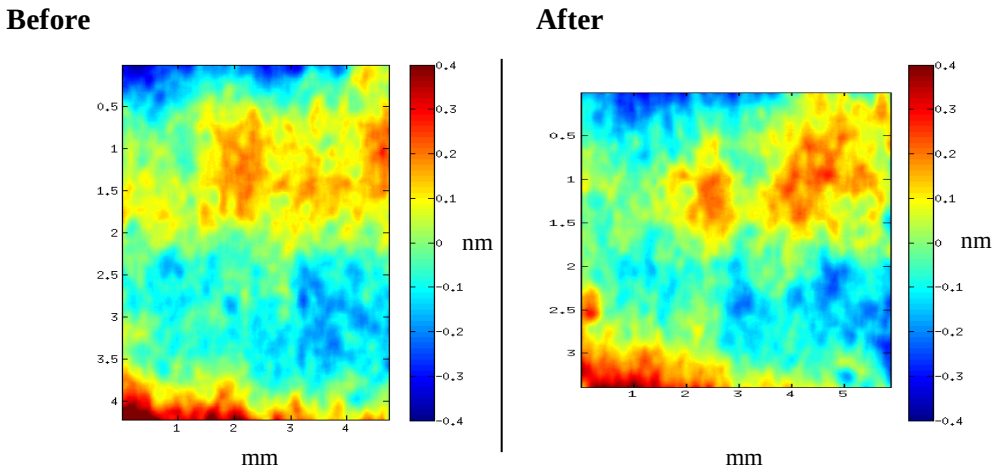

Figure 9.5: Effect of Beryllium windows replacement on the wavefront

9.4 Fresnel Zone Plate investigation with a 2D XGI

A Fresnel zone plate (FZP) provided by C. David and S. Rutishauser from the Paul Scherrer Institut (PSI) in Switzerland, was investigated in working conditions at the Diamond beamline B16 using a two dimensional grating interferometer (2D XGI).

A FZP with a diameter of 200 μm and an outermost zone of 100 nm was placed into the beam. An order sorter aperture was employed to select only the first diffraction order (cf. Sec. 3.2.3). The FZP was then illuminated with photons at an energy of 8.2 keV defined using the double crystal monochromator. The magnified beam was then analyzed using the 2D XGI combined with the X-ray Eye CCD detector (pixel size of 6.4 μm). The G_1 and G_2 gratings had pitch of respectively $p_1 = 3.576$ μm and $p_2 = 2$ μm. The intergrating distance was set to the third Talbot order ($\Delta l = 36.4$ mm) and scans of 16x16 images were recorded. The data were processed using Eq. 5.4 applied in the two orthogonal directions as explained in Ref. [94] and the wavefront reconstructed by two dimensional integration [130].

The wavefront reconstructions calculated from two scans using two different illuminations (from different areas of the incoming beam) are displayed in Fig. 9.6 (a-b). Because the grating pitches did not match upon magnification, a spherical component was observed in the reconstructed images corresponding to the deviation of the wavefronts from the perfect spherical wave having a magnification $M = \frac{2}{3.576/2}$. The wavefront errors with respect to the best ellipsoid was calculated (Fig. 9.6) from the previous images.

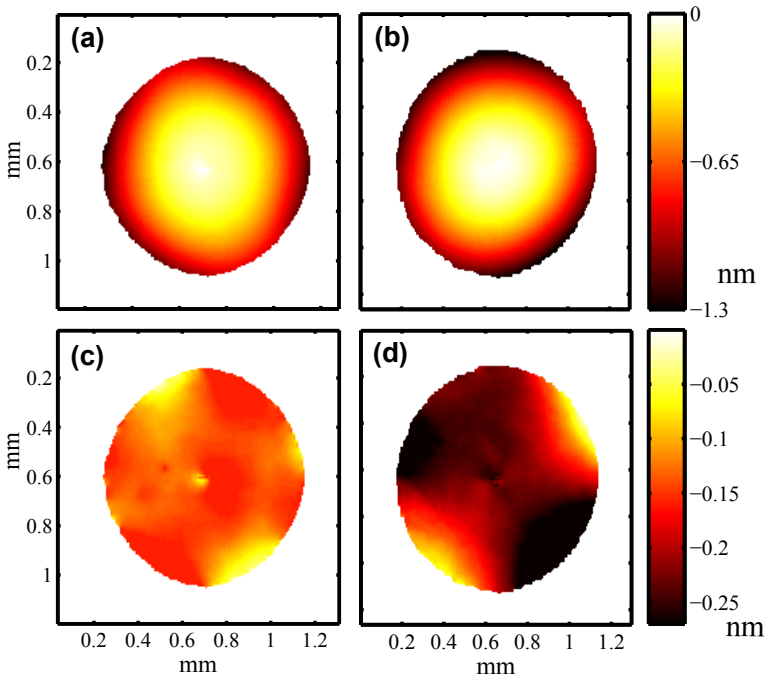

Figure 9.6: (a- b) Partial wavefront measured using the 2D XGI downstream the FZP illuminated with two different areas of the X-ray beam. (c-d) Optical wavefront abberation after ellipsoid removal from a-b.

The wavefront errors calculated for two different area of the beam are in the order or below the Å, i.e smaller than the wavelength. When using the grating interferometer in an absolute mode, i.e without removing flat field reference, it is difficult to separate the contribution to the error due to the incoming beam imperfections from the one caused by the optics defects. In addition, the contribution of the XGI itself should also be taken into account. Conversely, when working in the differential mode, the contributions of both the XGI and the incoming beam vanish.

The difficulty of characterizing an FZP optics arises mainly from the strong magnification they provide and from the fact that there is no simple way to isolate the incoming wavefront defects from the optics imperfections. This drawback usually prevents from extracting information pertinent for improving the fabrication of an FZP. This issue is also encountered when measuring other strongly focusing optics such as mirrors.

9.5 Conclusions

Transmission optics normally provides good focusing performance while being comparatively easier to align than reflective optics. However, they have usually a lower

efficiency compared to, e.g., grazing incidence mirrors. While transmission optics deforms only weakly the wavefront low spatial frequencies, surface roughness and inhomogeneities in the material bulk (high spatial frequency features) may lead to coherence degradation.

From the on-line metrology investigations presented here, it is seen that transmission optics does not create significant optical aberrations. As a matter of fact, due to the small interaction of x -rays with matter, a phase shift error of 2π in the X-ray regime is equivalent to an optical path in excess of 10 μm through a light element material (E $>$ 10 keV). Considering that current technology permits manufacturing of transmission optics with a sub-micrometer accuracy, it is unlikely to find important wavefront aberrations generated by such optics.

Conversely, reflective optics can generate much larger optical aberrations due to their intrinsic principle of operation. For instance, a single Angström of a mirror shape error creates upon reflection in the X-ray regime a phase shift larger than 2π radians.

10 The ESRF Ion Beam Figuring project

The ESRF Ion Beam Figuring project (IBF) aims at producing high quality focusing X-ray mirrors with the assistance of on line metrology. Its concept consists of etching flat substrates using ion erosion to reach a given stigmatic mirror shape. Care is taken to not degrade the surface roughness. The eroded surface eventually receives a heavy metal or multilayer coating to increase the reflectivity efficiency and the incidence angle of operation.

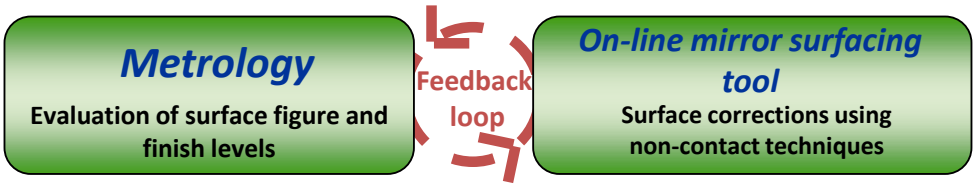

Figure 10.1: The OLMS iterative scheme.

One key idea of this profiling method for the achievement of a shape error free surface, is to operate the figuring iteratively, assessing the goodness of the etching with online metrology at regular steps [160, 168, 169]. As sketched in Fig. 10.1, two distinctive operations are successively iterated; the metrology measurements and the etching operation. This feedback loop is implemented to achieve minimization of the surface figure error, targeting intermediate surface profiles during the iterations. Online metrology methods are employed to measure the surface errors in order to quantify the required corrections, both to eliminate the present error and to compensate for the one predicted for the following iterations.

The figuring station available at the ESRF BM05 is sketched in Fig. 10.2. Its principle is the following: a flat substrate is positioned in a vacuum chamber (10^{-7} hPa) on a movable support and precision motors are available for the fine alignment of the mirror

in the beam. The station is equipped with a plasma ion beam for the etching of the substrate. An other important equipment is a pair of movable blades located in front of the substrate and acting as a screen. These blades are controlled through servo motors allowing independent control of their speed. The distance between the blades and the substrate is reduced to minimize the effects of the edges of the blades on the etching foot print. The primary goal of this thesis, in the frame of the IBF project,

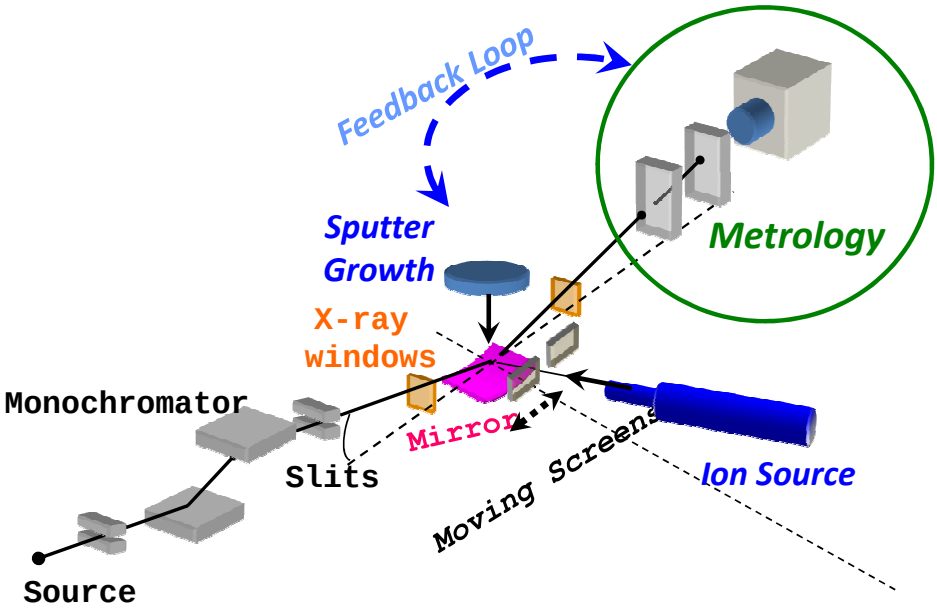

Figure 10.2: Sketch of the online mirror surfacing station on a beamline.

aimed at developing online metrology tools that could be integrated in the iterative process. This translated in the development of X-ray metrology mapping technique with sensitivity better than 0.1 μrad. One constraint of the process was also that the measured mirrors do not systematically present a focusing shape: the development of the method presented in Sec. 8 was for instance motivated by this problematic.

11 Adaptive optics

This chapter deals with the use of at-wavelength metrology methods for tuning adaptive optics. At synchrotron, one can take full advantage of deformable mirrors providing the presence of an online metrology method. Here we will present how the new developed techniques can contribute to the optimization of deformable focusing optics.

11.1 Interest and principle

The first approach to X-ray adaptive optics in this project occurred at an early stage of the project with the first experiment being the online characterization of a KB bender available at the ESRF BM05. The principle of adaptive optics consists of the deformation of a reflective surface shape with the aim of i) improving or correcting residual optical shape error after its manufacturing process and ii) correcting or reducing the influence of the incoming beam optical aberrations.

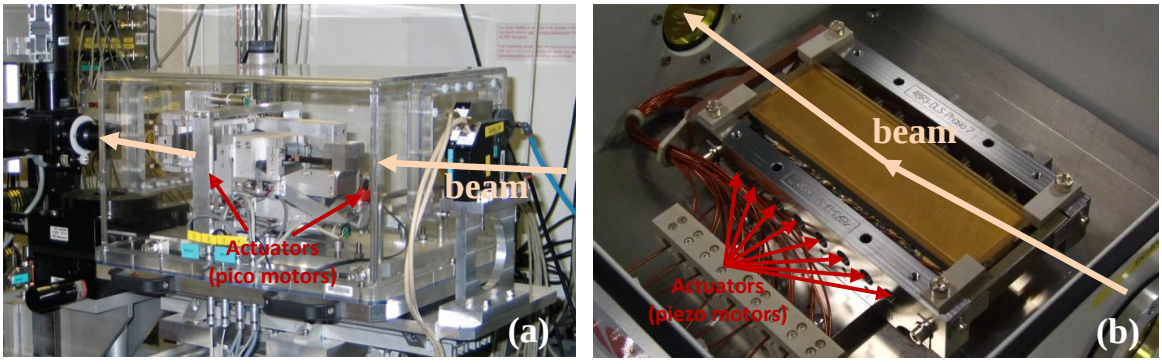

Figure 11.1: (a) The ESRF BM05 KB bender and (b) the Diamond superpolished bimorph mirror.

At synchrotrons, two kinds of reflective adaptive optics are employed:

- **Dynamically-bent mirrors**: These mirrors are equipped with mechanical motor actuators placed at each extremity of the mirror surface (2-moment bender). The substrate shape is designed so the mirror distorts into a shape approaching an ellipse when applying the correct force on each actuator. The possibility of applying small displacement increments through actuators permits to obtain a surface figure which is then kept under static strain over a long period of time. These mirrors are usually mounted in a KB configuration, i.e with two mirrors set perpendicular to each other [49]. To achieve better focusing efficiency, the optics is installed at a large distance from the source and a short distance from the focused image where the sample under study will be located. The Kirk-Patrick bender mirror of the ESRF BM05 in its protective chamber is shown in Fig. 11.1.(a).

- **Bimorph mirrors**: These mirrors use electrically activated piezo actuators maintained under tension to hold the shape of a relatively elastic surface. The design consists of a multitude of actuators distributed all along the surface and is suitable also for long mirrors (>1 m). One drawback of this principle is the quite long timescale necessary to reach a stable position after a change command is sent. A photo of a bimorph tested at Diamond B16 is displayed in Fig. 11.1.(b).

As mirrors, both devices are achromatic and require at-wavelength online metrology for their optimization. The next two sections present some original speckle based work on online characterization and optimization of the two optics shown in Fig. 11.1.

11.2 The ESRF KB bender

The XST technique was first tested for adaptive optics characterization using the ESRF BM05 KB bender. The goal was to measure the mirror slope change (response function) when applying various commands to the pico-motor actuators. At the early stage of this project, only the vertical mirror of the KB system was used, reducing the problem to two 1-dimensional ones.

The experimental setup consisted of the insertion of a speckle generator membrane downstream the mirror (here at a distance of 405 mm) and the placement of a FReLoN CCD camera at a distance of 1400 mm from the mirror center. The non optimized mirror focal distance was approximately 350 mm. The wavefront slope change when

activating an actuator was derived using the XST technique in the differential mode (see Sec. 6.2.2). Two images were taken before and after the sending of a displacement command to each of the actuators. The calculation of the deflection angles using the speckle subset displacements, allowed the characterization of the wavefront slope evolution per actuator step increment. For an efficient and reliable numerical tracking of the speckle, the wavefront distortion between images was kept small, using only moderate command steps, i.e in the order of ten pico-motor steps. The actuators response functions in the plane of the membrane and per unit of command extracted are displayed in Fig. 11.2.

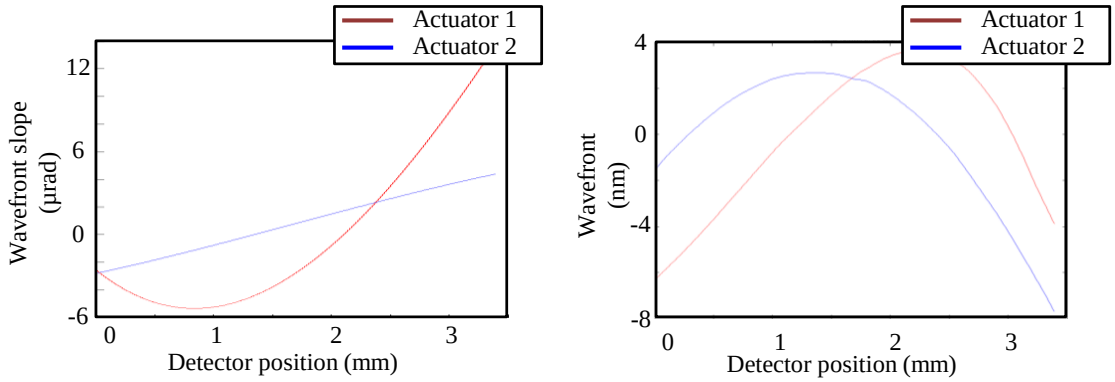

Figure 11.2: KB bender actuator response functions on the beam wavefront slope (a) and wavefront (b), per unit of command and measured at the detector position.

From the magnification factor of the probe beam in the plane of the membrane (here $M \approx \frac{1}{7}$), one can recover the mirror slope deformation per command unit: approximately equal to the wavefront slope differential in the plane of the membrane divided by 2M. In our case, that leads to surface slope response functions in the order of a single micro radian. It is worth mentioning that, despite its interest for the design and manufacturing of mechanical benders, the characteristic distortion function of the mirror surface is not mandatory for online optimization. Indeed, under beamline working conditions, the mirror follows the principle of common adaptive optics: the optimization loop of the benders use only the wavefront aberration information to reduce the shape error.

Thus, these results confirmed the possibility of employing online speckle methods to optimize adaptive optical elements.

11.3 The Diamond super-polished bimorph mirror

X-ray bimorph mirrors are used at synchrotrons to focus the X-ray beams in different configurations. Indeed, their main advantage lies in their highly deformable surface and the presence of multiple actuators to permit users to conveniently change the focal distance and adapt the probing beam properties to their experiment. Because of the grazing incidence imposed in the hard X-ray regime, combined with the high number of actuators, online metrology of such device is a complex task, however mandatory to exploit their full potential.

The Diamond optics group has designed and got fabricated a unique super polished bimorph mirror [170] that has been the subject of deeper experimental characterization and optimization during this thesis project. This 120 mm long mirror substrate was fabricated by SESO (Societé Européenne de Systèmes Optiques) and mounted on 8 piezo actuators. The actuators can be activated with nanometer accuracy thanks to modern highly stable electronic power supplies. Subsequently, the substrate received treatments from the JTEC company in Osaka, Japan: its surface was polished using the Elastic Emission Machining (EEM) process [171] that provided an Angström surface roughness and nanoradians order figure slope error from an elliptical designed shape. The silicon optical surface remaining uncoated, the reflectivity is obtained by operating under total reflection of X-rays. Online characterization and optimization of

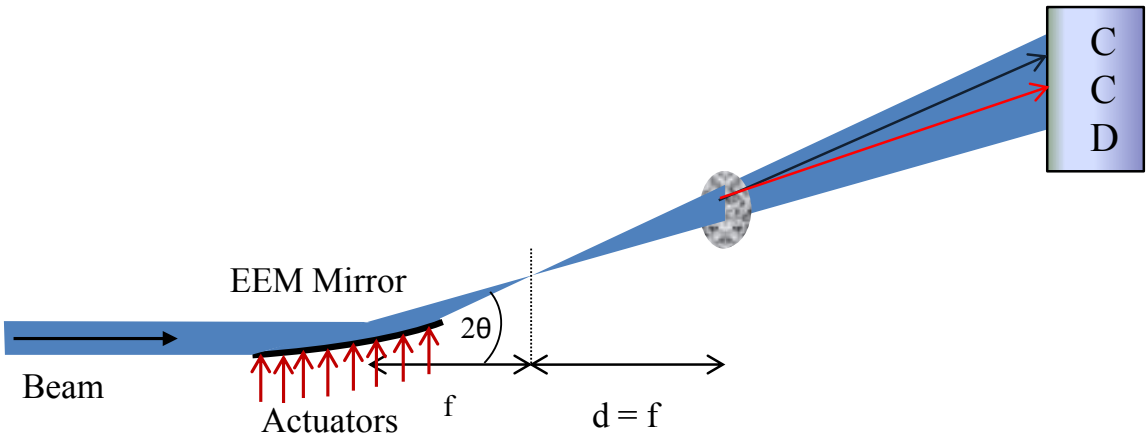

Figure 11.3: Experimental setup for the optimization of the Diamond super polished bimorph mirror.

the mirror behavior was carried out at the Diamond beamline 16. The XST technique combined with the generalized scheme based also on speckle, permitted to improve the focusing parameters of the bimorph mirror by comparison to the parameters obtained using the laboratory and online pencil beam methods.

The experimental setup consisted of mounting the mirror on the first stage of the optics table of the experimental hutch (see Sec. 3.1.2). As schematically displayed in Fig. 11.3, a speckle generator membrane was placed at approximately twice the vertical focal distance ($2f \approx 600$ mm) downstream the mirror. The PCO camera was placed at the furthest possible distance from the membrane, i.e. $d = 600$ mm. As the membrane was located one focal length away from the focus, the magnification between the incoming beam size and the one at the membrane position was expected to be $M \approx 1$ when the mirror was focused. This configuration gave approximately a direct equivalence, apart from the factor 2, between the measured wavefront slope and mirror slope.

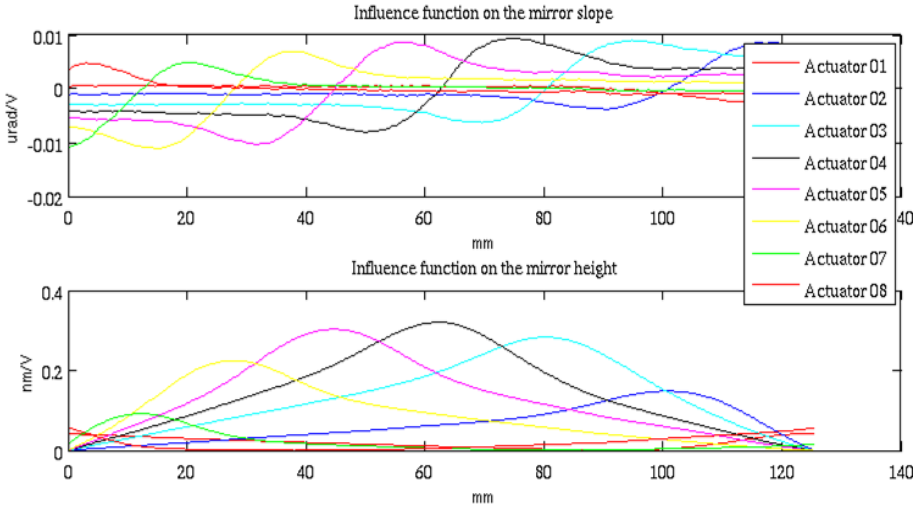

Figure 11.4: Bimorph mirror actuators response functions on the wavefront slope (top) and wavefront (down).

The mirror shape optimization is a three step process, two of them being operated iteratively:

1. First, the actuator response functions are characterized using the XST technique in the differential mode (cf. Sec. 6.2.2). For this, 9 images are acquired: equivalently to the characterization of the ESRF bender an actuator increment is sent between each image acquisition. The XST is then applied to each consecutively taken pair of images and the differential wavefront slope corresponding to each actuator extracted. The calculated gradient maps are averaged along the horizontal dimension and these functions stored in a matrix A of size $8 \times n$, where n is the number of deflection points calculated in the vertical direction. In our case, 300 points were used. The wavefront gradient actuators response functions

are displayed in Fig. 11.4. By comparison with the previous characterization of the BM05 KB bender, one can notice that one unit of command applied on the bender has a larger influence on the surface than a 10 V command sent to the bimorph mirror presented here.

2. Next, the effective beam wavefront is measured using the generalized scheme presented in 7.2.2. This processing method has several advantages: it permits to keep the detector static and to use a large membrane to detector distance d because the speckle size between images does not change contrary to the XST technique in the absolute mode. The second derivative is then calculated from stacks of 30 images and the wavefront slope error recovered by integration.

3. Last, the wavefront error calculated is minimized using the actuators response functions employing a zonal inversion matrix method, well known in the field of adaptive optics [172]. Noting y the wavefront slope error from the second process step and x the piezo correction that needs to be applied, the problem is equivalent to the linear problem solving $y = Ax$. This equation is solved in the least square sense by matrix inversion: $x = A^{-1}y$. Because the matrix A is not square and singular with computer working precision, the inversion is operated in the Moore-Penrose pseudo inverse sense using a singular value decomposition [173]. The calculated command x is sent to the system and the process reiterated from point 2.

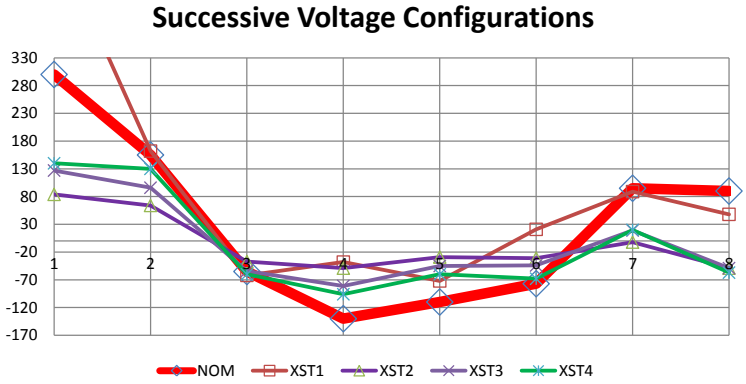

Figure 11.5: Successive voltages applied during the adaptive mirror focusing optimization.

While the first step of the method is only operated once, the next two steps need iterations to compensate for the non perfect linearity of the system. Nevertheless, because of the high sampling resolution and the good sensitivity of the method to wavefront error measurements and response function determination, the process converges in only few iterations.

During the experiment, mirror focusing was attempted for two different configurations: $E_1 = \{p = 46.5\text{m},\ q = 0.40\text{m},\ \theta = 3\text{mrad}\}$ and $E_2 = \{p = 46.5\text{m},\ q = 0.33\text{m},\ \theta = 2.5\text{mrad}\}$.

In Fig. 11.5 are shown the successive calculated voltages for the optimization of the E_1 configuration. The red curve shows the optimal voltage configuration calculated using Diamond-NOM measurements. One can notice the convergence and the profile similarity with the commands calculated from the metrology lab measurements.

After the final iteration, the focus size was measured using the knife edge technique. For configuration E_1, the focus size was 0.84 μm and in configuration E_2 it was 0.52 μm. For comparison, optimizations using the slit scan technique [47] managed to reach respectively 1.01 μm and 0.77 μm: despite being more simple to implement, the smaller number of wavefront characterization points provided by the pencil beam technique, limits the achievable performance of the optimization process[174]. Figure 11.6 shows the correctable zones

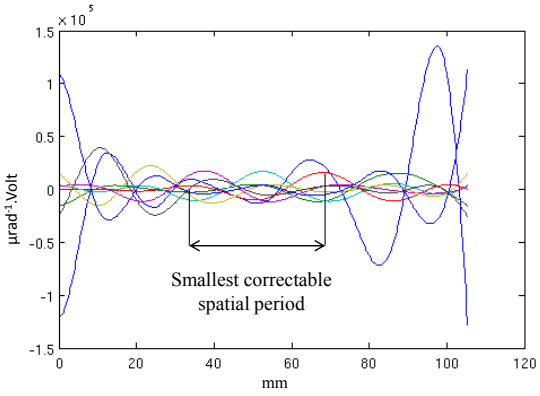

Figure 11.6: Bimorph mirror correctable modes.

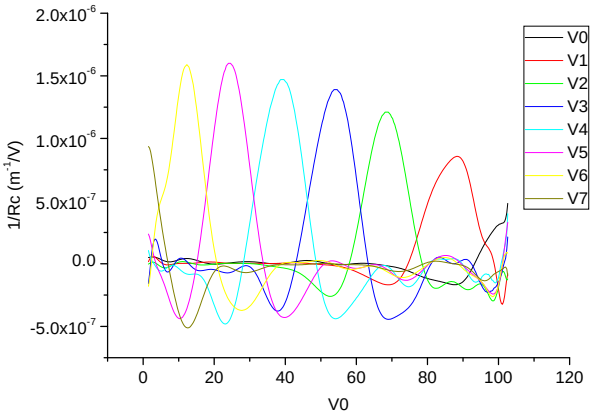

Figure 11.7: Response function of the adaptive mirror actuators on the mirror local curvature.

of the system. They are obtained by matrix inversion of the actuator response functions and permit to visually evaluate the length of the smallest correctable wavefront error. In the case of the 120 mm long mirror and 8 actuators, the smallest wavefront zone correctable is of 40 mm length. More actuators would be required to compensate for higher spatial frequency defects.

In visible optics, the local radius R of a mirror with negligible thickness changes in proportion to the applied voltage V and is given by: $R = \frac{Vd_p}{t^2}$ where t is the thickness of the substrate and d_p is the coefficient of the piezo-electric tensor. Because of this linear relation between the voltage and R, bimorphs are well suited for integration with a wavefront curvature sensor. In theory a perfect punctual actuator would have a very local influence on the mirror surface. In Fig. 11.7, the actuators' influence on the (inverse) mirror surface curvature are plotted. One can observe two interesting points. First, the actuators located on the focus side have smaller influence on the mirror surface: one explanation can be the larger strains in the material located on the focus side of the mirror. The second point is regarding the 'over shoot' on the sides of the gaussian peaks: they are probably due to the stiffness of the substrate preventing from a Dirac distribution shape behavior of the actuators response.

Conclusions

It has been demonstrated that online metrology technique with enhanced sensitivity and wavefront sampling allows one to achieve excellent optimization of adaptive optics. Because of its easiness of mechanical implementation and their high performance, the speckle based methods are expected to become valuable tools at new nano-experiment beamlines using adaptive optics.

12 Sub-micro imaging

In this chapter, sub-micron phase contrast imaging with the two techniques studied in this thesis are presented. Such microscopy techniques are motivated by the need for imaging methods capable of resolving the inner of the matter at the sub-micrometer scale.

12.1 Micro phase contrast imaging using the 2D XGI

12.1.1 Introductory remarks

The following section presents the implementation of the newly introduced 2D XGI for submicrometer phase contrast imaging. This work has been published in the *Optics Letters* under the title "X-ray submicrometer phase contrast imaging with a Fresnel zone plate and a two dimensional grating interferometer". This paper results from a collaboration with S. Rutishauser and C. David from the Paul Scherrer Institute, Switzerland, who have designed and produced both the Fresnel Zone Plate and the 2D gratings. This work was carried out before the germination of the generalized scheme presented in Sec. 7.2. It permitted to reveal the high sensitivity and stability of the device.

12.1.2 Fourth paper

X-ray sub-micron phase contrast imaging with a Fresnel Zone Plate and a two dimensional grating interferometer.

Authors: *Sebastien Berujon, Hongchang Wang, Ian Pape, Kawal Sawhney, Simon Rutishauser and Christian David*

The application of a two dimensional grating interferometer - Fresnel Zone Plate combination for quantitative sub-micron phase contrast imaging is reported. The combination of the two optical elements allows quick recovery of the phase shift introduced by a sample in a hard X-ray beam, avoiding artifacts observed when using the 1D interferometer for sample with features oriented in the unsensitive direction of the interferometer. The setup provides sub-micron resolution due to the optics magnification ratio and a fine sensitivity in both transverse orientations due to the 2D analysis gratings. The method opens up possibilities for sub-micro phase contrast tomography of microscopic objects made of light and/or homogeneous materials with randomly oriented features.

Hard X-ray phase contrast imaging has been subject to an increasing interest over the last decade as it allows imaging of the inner structure of weakly absorbing -low-Z- objects, which display poor contrast in traditional absorption radiography. In parallel, the development of adapted focusing optics has opened the imaging methods of the matter at the nanometer scale to many fields. Phase microscopy is regarded as one of the most valuable tools in the prospect of a better understanding of materials. Several techniques have been described to measure quantitatively the distortion of hard X-ray beam wavefronts passing through a sample. The drawback for most of those techniques is that they usually use specific optics [175], require a fully coherent beam [11] or become less quantitative in certain cases [176, 144]. In contrast, X-ray grating interferometers provide a high accuracy on the X-ray wave front gradient measurement: they have a low sensitivity to vibrations and do not have any stringent requirement on transversal and longitudinal coherence [66, 91, 68]. Advantage has been taken of this technique to design an X-ray microscopes when used in a combination with a Fresnel Zone Plate (FZP) [110]. Tomography with a one-dimensionally Talbot interferometer and a FZP has even been performed using a comparable setup to the one displayed here [177]. However, this design of interferometers, comprising of one dimensional gratings, displays reconstruction artifacts when applied to many real situations, due to the lack of sensitivity of the device to one of the transverse dimension.

Recently, a 2D grating interferometer has been introduced into the X-ray regime which allows simultaneously the recovery of both the horizontal and vertical beam phase gra-

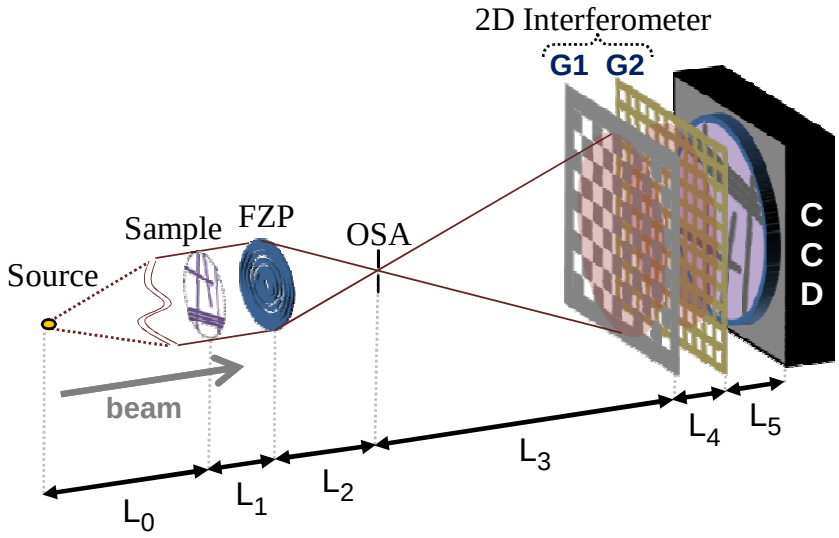

Figure 12.1: Setup of the experiment. In our case $L_0 = 47.5\ m$, $L_1 = 30\ mm$, $L_2 = 129\ mm$, $L_3 = 930\ mm$, and $L_4 = 64\ mm$.

dient, eliminating most of the common reconstruction artifacts usually encountered with the 1D interferometer. Indeed, the most serious errors associated with the unwrapping of strong gradient and the 1d integration process have now been overcome thanks to the sensitivity of the device to object which were not visible before because positioned parallel to the grating lines [178, 94, 78]. In this letter, we demonstrate that it is possible to perform sub-micron phase microscopy using a FZP and the 2D grating interferometer. We show that the technique both provides the spatial resolution that is obtained when working with absorption-contrast microscopy, and also provides the dephasing profile of a sample with a high sensitivity independent of the orientation of the sample features. As the increase in contrast compared with absorption radiography is many orders of magnitude for light elements, this device is expected to provide access to a better knowledge of light materials which possess randomly oriented features.

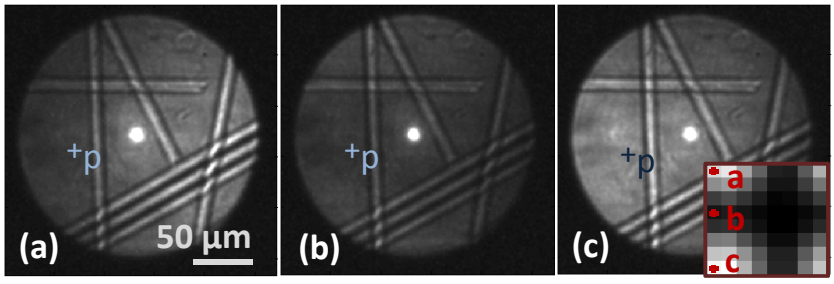

Figure 12.2: Three images from the raster scan. The three images (a), (b) and (c) correspond to three acquisitions taken at different positions of the grating during the scan. The intensity in the point p during the scan is displayed at the bottom right where are also shown the corresponding position of the three images.

As a focusing optics for hard X-rays, the FZP is a good choice due to the relatively good efficiency and short focal distance; the latter gives the high magnification ratio

that such kind of optics offers. Moreover, it provides magnification ratios which are equal in both directions, which is required by the equivalent pitches in the two direction of the 2D gratings.

Our experimental setup is presented in Fig. 12.1. The sample was composed of a bunch of carbon fibers which were attached to a Kapton foil. An imaging configuration putting the sample upstream the FZP, has been preferred over the projection microscope, in order to minimize the blurring occurring from the defocusing effect [177]. The sample was therefore placed at a distance $L_0 = 47.5\ m$ from the bending magnet source and at a distance $L_1 \approx 30\ mm$ upstream of the FZP. The energy of the X-rays was 8.2 keV selected by means of a double Si(111) monochromator ($\Delta E/E \simeq 10^{-4}$) located 15 m from the source. The FZP used to focus the beam was made using the process described in Ref. [179]: it offered an aperture of $D = 200\ \mu m$ while its smallest zone was of $\Delta r = 100\ nm$. At 8.2 keV, the FZP was then focusing the beam at a distance $L_2 = 129\ mm$ from the FZP. No central stop was used on the zone plate but an order sort aperture (OSA) with a diameter of $\phi = 10\ \mu m$ was placed in the focal plane in order to remove the higher orders leaving only the first diffraction order.

The 2D grating interferometer works on the principle of a "standard" grating interferometer with a phase grating and an absorption grating. The first grating G_1 separates the beam into the -1 and 1 order to create interference between these two diffraction orders. The absorption grating G_2 is then used to resolve the interference pattern which is usually too small to be resolved directly by the detector [91]. The distortion of this recorded pattern from the expected one permits to calculate accurately the phase gradient of the wave front. The pitch of the first grating $p_1 = 3.576\ \mu m$ was chosen to be less than twice pitch of the second grating $p_2 = 2.000\ \mu m$. This choice was made considering the beam divergence downstream the FZP, which is responsible for the magnification of the spatial period of the Talbot interference pattern. To obtain a magnification ratio that almost matched the second grating pitch p_2 and the magnified interference pattern, the first grating of the interferometer was placed at a distance $L_3 = 930\ mm$ downstream the focus and the intergrating distance was set to the fifth order ($N = 5$) Talbot distance when considering the divergence of the beam $Z_{T_5} = L_3/(8L_3\lambda/p_1^2 - 1) \approx L_4 = 61\ mm$. The magnification ratio obtained was then $M \approx 7.6$. The detector used was a CCD device coupled with a scintillator forming an indirected illumination system, providing an effective pixel size of $S_{pix} = 6.4\ \mu m$. To avoid any diffraction artefact from the second grating, the detector was placed as close as possible to the absorption grating, i.e. $\sim 15\ mm$. The extraction of the

interferences phase was done using the method described by Zanette et *al.* [78]: a raster scan of 8 x 8 points of the first grating was made over one period of the grating in each direction thanks to two piezo motors. Images corresponding to three different points of the scan are presented in Fig. 12.2. A small change in intensity of the images of the scan can be seen: for each pixel the intensity is varying periodically along both directions as shown at the bottom right of Fig. 12.2. From this image stack, the use of a bidirectional Fourier process permits to recover the phase information Φ of the interference pattern created by G_1. To deal with the zeroth order (direct beam) and the spherical aperture of the lens, a mask was used in the data processing to select only the pixels of interest identified by two thresholds.

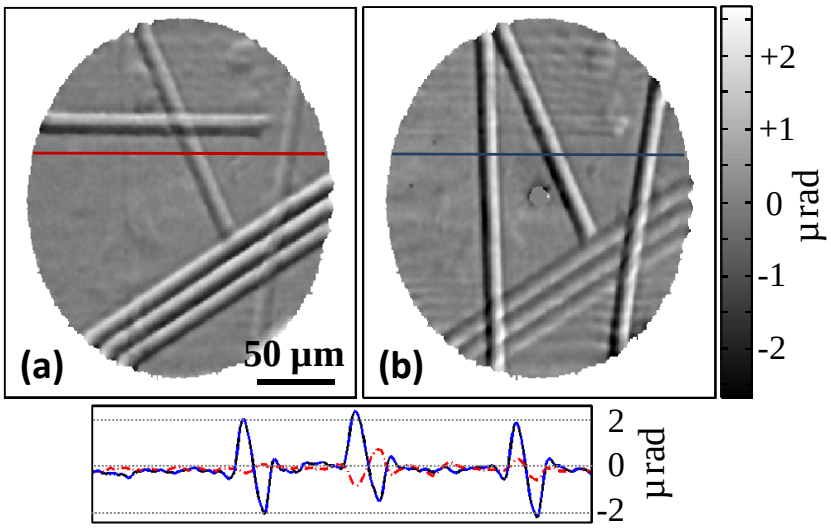

Figure 12.3: Calculated deflection angle in μrad (a) vertical gradient. (b) Horizontal gradient. As the profile cuts mirror it, one can notice the difference of visibility of the fibers depending on their orientation.

The two orthogonal difference wave front gradient maps were reconstructed using the relationship between the wave front gradient ∇W and the phase difference $\Phi^{samp} - \Phi^{ref}$of the scan with and without the sample [94, 91, 68]:

$$\nabla W \cdot \boldsymbol{e_{x/y}} = \frac{p_2}{2\pi} \frac{(\Phi^{samp}_{x/y} - \Phi^{ref}_{x/y})}{L_4}$$

These two difference gradient maps are displayed in Fig. 12.3. It can be seen that the very low visibility of the vertical features in the horizontal wave front gradient map and vice versa: this demonstrates the advantage of the two dimensional grating interferometer over the previous traditional single dimensional interferometer used so far. When working using a 1D grating interferometer, the gradient map is lost in one direction: the insensitivity of the device to objects oriented parallels to the lines of the grating, combined with some unavoidable measurement noise, often created some, as

yet, unrecoverable errors in the reconstruction process [78].

The final wave front was reconstructed by solving the Poisson equation, using simultaneously the vertical and horizontal gradients in a pseudo inversion matrix algorithm [180]. The calculated wave front, as well as the equivalent dephasing is displayed in Fig. 12.4. The refractive index of the carbon fibers at 8.2 keV being $\delta = 6.8 \times 10^{-6}$ and its absorption index being $\beta = 1.07 \times 10^{-8}$, their ratio is of $\delta/\beta = 635$ (Ref. [131]). The expected phase shift for our carbon fiber with a diameter of $\approx 11\ \mu m$ is π: this fits very closely to the values calculated in the reconstruction and demonstrating the quantitative accuracy of the method whatever the orientation of the imaged objects. The spatial resolution is theoretically limited either by the shear $2\Delta s \approx Np_1/2$ in the plane of the first grating, or by the detector resolution $\sim 2S_{pix}$. In the first case, where the shear is larger than the pixel size, the limit in resolution in the sample plane becomes $\sim Np_1/(2M(L_3+L_4)/L_3)$. Whereas in the second case this limit is $2S_{pix}/M$. For our experiment, the pixel size being larger than the shear ($\Delta s \approx 2.6\ \mu m$), the resolution was of $\sim$ 840 nm.

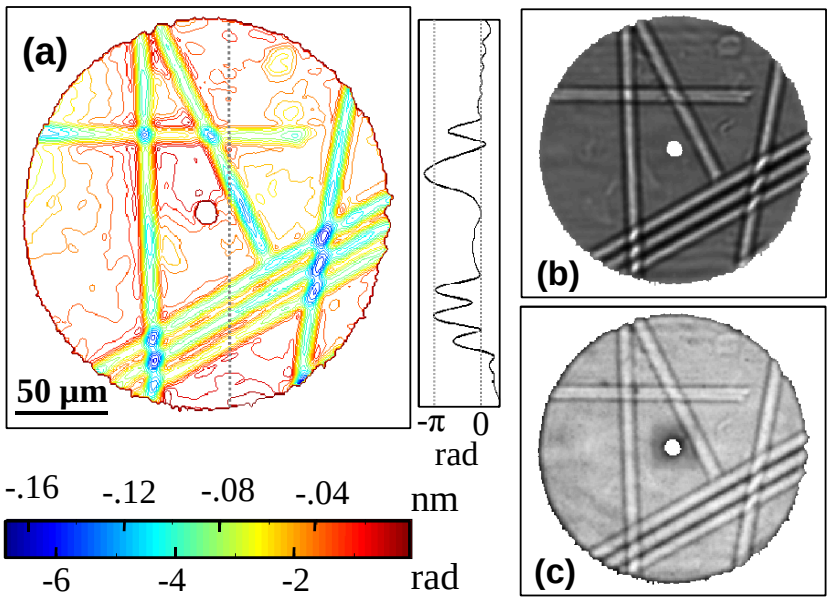

Figure 12.4: (a) Wave front reconstruction from the two directional gradient and corresponding wave front phase shift. The profile shown on the side corresponds to a cut following the dashed. (b) Absorption image (c) Dark field image.

Fig. 12.4 shows two different contrast images that can be obtained using the 2D GI grating interferometer. The absorption image (b) is an image taken after propagation, and therefore partial coherence is responsible for the contrast at the edges of the sample features. As the electron density difference between the rods and surrounding medium is very smooth, only little edge contrast is available in the absorption image (b) and in the dark field image (c). Oppositely, differential phase contrast allows quantitative

analysis of homogeneous part of sample, even when these ones are larger than the transverse coherence length.

Compared to our setup, one can already gain in resolution using a stronger focusing FZP and/or putting the 2D interferometer further from the focal point. However, as the beam wave front becomes smoother as the photon diverge, the working magnification ratio is limited by the decreases of the angular sensitivity: following the same method as in Ref. [92], this angular sensitivity Ψ scales here as $\Psi = L_2 L_5/(p_2(L_3 + L_5)) \sim 1/M$. Therefore, depending on the sample spatial frequencies and phase distortions, the setup must be optimized to find the best compromise between the researched resolution and sensitivity. In our case, the sensitivity of the device, defined by the standard deviation of the refracted angle in a constant phase area, was of 70 *nrad*.

In conclusion, the high and quantitative sensitivity and the sub-micron resolution of the 2D grating interferometer microscope make this technique a promising candidate for sub-microns analysis of complex samples made of light materials and different feature orientations through radiography and soon tomography.

12.2 Micro phase contrast imaging using XST

12.2.1 Introductory remarks

Soon after the demonstration of sub-micrometer phase contrast imaging with the 2D XGI, the question of a comparable feasibility with the XST technique arised. The equivalent technique was implemented to try to get a better resolution. The following contribution will show that contrary to the XGI, this can be done without sacrificing the sensitivity. The sample imaged in this reprint entitled "X-Ray phase microscopy using the Speckle Tracking technique" and published in the *Applied Physics Letters*, are micrometer size spheres that have characteristic sizes ten times smaller than the fiber samples used in the previous section. Again, despite the good focusing performance of the FZP, one had to deal with the moderate flux transmission efficiency of the optics. It is worth mentioning that the spheres imaged therein are at the limit of what is probably feasible with the photon flux provided by a bending magnet and focused by a narrow spectrum band focusing optics.

12.2.2 Fifth paper

X-Ray phase microscopy using the Speckle Tracking technique

Authors: *Sebastien Berujon, Hongchang Wang, Ian Pape, Kawal Sawhney*

Hard X-ray phase microscopy using the Speckle Tracking technique is presented and the practical implementation of this microscope explained. It is demonstrated that the spatial resolution of the Speckle Tracking technique can be pushed down to the nanometer scale without sacrificing the angular sensitivity, which is in the tens of nanoradians range. Moreover, the method is suitable for the analysis of dynamic samples. Experimental demonstration of the method is given for the case of phase imaging of micrometer size polystyrene spheres using a Fresnel zone plate as a magnifying optical element.

For the last decade, hard X-ray microscopy has been viewed with an increasing interest as large scale facilities like synchrotrons offer beams with improved intensity and quality. Indeed, because of their short wavelength, hard X-rays theoretically allow the imaging of matter up to a limit set by the diffraction far below the visible light wavelength, i.e in the order of few tens of nanometers. Meanwhile, X-ray phase contrast imaging has also benefited from intensive efforts, and now permits the imaging of materials made of light elements with a sensitivity many orders of magnitude higher than the one obtained with absorption contrast [132]. In addition, researchers have put increasing efforts in the development of techniques that can map the phase shift induced by a sample from a single exposure of it, as they allow the analysis of dynamic samples [143, 181].

Several methods are now-a-days used by the synchrotron community to perform X-ray microscopy. One of the most employed techniques is X-ray scanning microscopy in which a sample is moved across the focal point of a beam. Despite presenting the advantage of providing both the absorption and fluorescence maps of a sample, the technique spatial resolution is limited by the smallest focal spot size achievable and requires one exposure of the sample for each map point. The scanning Zernike phase contrast microscope is an improvement of the method providing in addition an enhanced phase contrast signal and that has recently been made available in the hard X-ray regime [176]. Nevertheless, because of their better compatibility with tomography processes, new full field imaging methods are today regarded with higher interest. New reciprocal space (far field) techniques such as coherent diffraction imaging [50, 51]

and ptychography [12, 11] have recently been developed, demonstrating the ability of nanometer scale spatial resolution. However, they also require a large number of sample exposures and put strong requirements on the beam stability, coherence and flux. Real space, near field, phase imaging technique are methods commonly employed that use the partial coherence of third generation synchrotron sources. Propagation based techniques for instance are sensitive to the second derivative of the phase [56, 144, 58]. This kind of technique is easy to implement but can suffer from artifacts when imaging homogeneous sample. Phase sensitive methods relying on the principle of high spatial frequency wavefront modulation and deflection angle calculation such as grating interferometry [67, 91, 94], coded apertures [182] or Hartmann-like instruments [183, 143] are phase imaging techniques sensitive to the beam phase gradient and having demonstrated several advantages. Nevertheless, when used in combination with a magnifying optic, the gain in spatial resolution in these techniques is obtained at the cost of a reduced sensitivity [142]. Various kind of alternative attempts have been made but they suffer from the requirements of specific optics or beam coherence [184, 176].

The recently introduced X-ray Speckle Tracking (XST) technique [137, 125] fall in the full field technique category, and also use the principle of high spatial frequency wavefront modulation. It benefits from many advantages such as low requirements on longitudinal and transversal coherence and the ability to provide the two dimensional gradient of a beam wavefront distortion from a single exposure of the sample and the subsequent phase imaging of dynamic samples. We show here that, using a magnifying optical element, the resolution of the technique can be enhanced far below the detector pixel size and without degrading the sensibility of the device. An experimental verification is provided below in an experiment consisting of imaging polystyrene spheres.

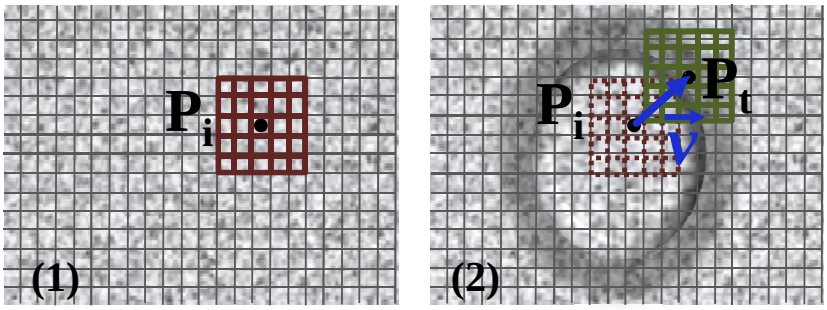

Figure 12.5: Illustration of the DIC algorithm. Image (1): reference speckle pattern (direct beam); image (2): displaced pattern (sample present).

In order to get around the trade off between angular sensitivity and spatial resolution usually encountered in deflection angle based techniques [142, 92], one has to consider

the XST basic principle: an x-ray speckle pattern is generated using a membrane illuminated by the partially-coherent light produced by third generation synchrotrons [24, 117]. A first image of this pattern is recorded with the direct beam (no sample). Next, the sample is inserted in the beam, modifying the beam propagation direction and hence distorting the speckle pattern recorded in a second image. The next step of the data processing uses digital imaging correlation (DIC) algorithms [127] whose principle is illustrated in Fig. 12.5. A subset centered around a given pixel is selected in the first image. Then, this piece of speckle pattern is moved across the second image to find a subset with similar speckle features in the second image. This step is performed using a cross correlation algorithm which allows to track similar subset from one image to the other with a subpixel accuracy [127] and hence calculate an accurate displacement vector $\mathbf{v}$ for each subset. For each pixel (i, j) the wavefront gradient is calculated using the relationship:

$$\overrightarrow{\nabla} \cdot W(i,j) = \frac{\overrightarrow{v_{ij}}}{L_3} \tag{12.1}$$

where $\overrightarrow{v} = \overrightarrow{P_i P_t}$. The deflection angle in the base $(\mathbf{x}, \mathbf{y})$ introduced by the sample are then $\Theta_x(i,j) = \frac{\mathbf{v_{ij}} \cdot \mathbf{x}}{L_3}$ and $\Theta_y(i,j) = \frac{\mathbf{v_{ij}} \cdot \mathbf{y}}{L_3}$.

The method proposed here is to apply the XST technique in a magnifying setup to recover the dephasing profile of micrometer size objects of light material from a single exposure. As a demonstration, sub-micron imaging using XST has been performed at beamline B16 of Diamond Light Source. The objective was to characterize with a high spatial resolution polystyrene spheres, which had a design radius on the order of one micron. A Fresnel Zone Plate (FZP) was used to get the high magnification ratio. The FZP was chosen for its ease of alignment and the short focal length it provides. The one used for the experiment was made from Au with a zone height of 1 μm on a silicon nitride membrane. Its diameter was of 200 μm and its outermost zone width was 100 nm. Its fabrication and a more more complete description of it is provided in Ref. [179]. An order sorting aperture with a 10 μm diameter was placed just upstream of the focal plane to select only the first diffraction order of the FZP. The photon energy was set to $E = 11\ keV (\lambda = 0.11\ nm)$ by a double crystal monochromator ($\frac{\Delta E}{E} \sim 10^{-4}$). At this working energy, the efficiency of the FZP was of ~ 10 % [179]. The sample, a speckle generating membrane with 0.45 μm pore size, the FZP and the detector were all mounted on independent tri-axis translation stages of a single versatile table located at ~ 50 m from the bending magnet source of the Diamond Light Source 3 GeV storage ring. A schematic of the experiment is shown in Fig. 12.6. The specifications of the beamline are described in Ref. [26]. The sample

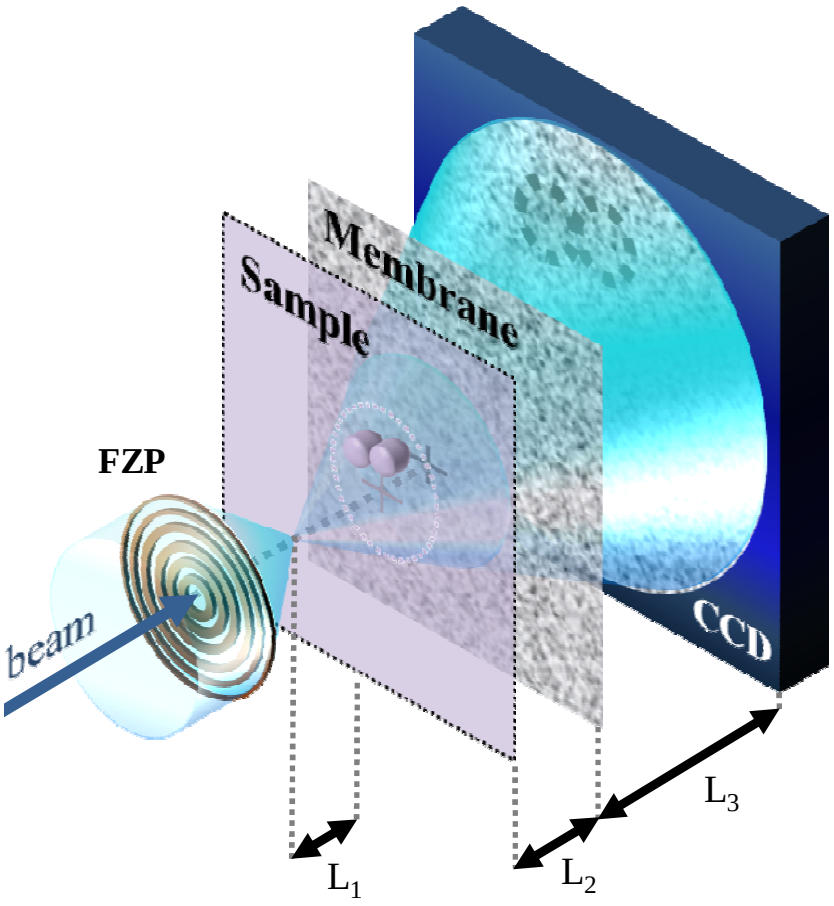

Figure 12.6: Sketch of the setup of the experiment (not to scale). In our case the distance from the focal point to the sample was of $L_1 \simeq 8\ mm$, the membrane was located $L_2 = 172\ mm$ beyond the sample and the detector at a distance $L_3 = 3985\ mm$ from this membrane.

was placed only a few millimeters ($L_1 \simeq 8\ mm$) beyond the focal plane of the FZP to get a very high magnification ratio. The other distances were set to $L_2 = 172\ mm$ for the distance from the sample to the membrane and $L_3 = 3985\ mm$ for the distance from the membrane to the detector. These distances correspond to a magnification $M \simeq 500$ of the sample in the plane of the detector and an equivalent pixel size of 13 nm. Moreover, the magnification of the speckle in the plane of the detector and the magnification of the sample in the plane of the speckle generating membrane should be also considered. From these physical parameters, one can calculate that the spheres image would be magnified by a factor $\sim$ 22 in the plane of the membrane. This matches well with the criterion that the frequencies of the carriers, i.e the speckle grain size, must be higher than the one of the investigated object in the plane of the scattering pattern. In addition, the speckle grains were magnified by a factor $\sim$ 23, having a typical size of 10 μm in the plane of the detector, making then the speckle pattern resolvable by the camera with a 6.4 μm effective pixel size.

Following the same method as in Ref. [92], the angular sensitivity defined by $\Psi = \frac{|\mathbf{v}|}{\alpha}$

can be calculated in the case of the XST in a magnifying geometry setup. In other words, this sensitivity factor expresses the size of the measurable displacement vector for a given deflection angle and then, knowing the smallest vector $\mathbf{v}$, the achievable sensitivity can be measured [137]. For this calculation, we consider (see Fig. 12.7) a ray passing through the sample and being deflected by an angle α (ray plot in green) and a ray passing the same point A in the plane of the membrane when no sample is present in the beam (ray plot in red). The norm of the displacement vector is then the distance separating the point of impact on the detector of these two rays.

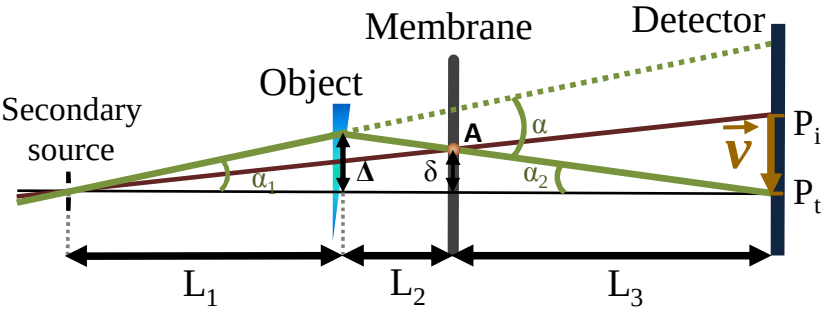

Figure 12.7: Geometrical consideration for the calculation of the angular sensitivity.

With the notation of Fig. 12.7, the following equations can be extracted:

$$\begin{aligned} \alpha &= \alpha_1 + \alpha_2 \\ \Delta &= \alpha_1 L_1 = \alpha_2 (L_2 + L_3) \\ \delta &= \alpha_2 L_3 = |\mathbf{v}| \frac{L_1 + L_2}{L_1 + L_2 + L_3} \end{aligned}$$

Eliminating α_1 and α_2, the calculation ends up to:

$$\Psi = \frac{|\mathbf{v}|}{\alpha} = \frac{L_1 L_3}{L_1 + L_2} \tag{12.2}$$

As one would expect, the sensitivity increases with an increase of the distance L_3 and a decrease of the distance L_2. For smaller L_2 values, membranes with smaller grain size would be required to satisfy the criteria on the spatial frequencies of the speckle to remain higher than those of the sample features. This is however not an issue as commercial filter membranes are available in a wide range of pore sizes ranging from 0.2 μm to > 8 μm. This therefore relaxes the requirement on the placement of the membrane unlike some other techniques [142] and hence allows to get a high sensitivity by minimizing L_2.

The raw images are shown in Fig. 12.8. The top images are recorded data and were used

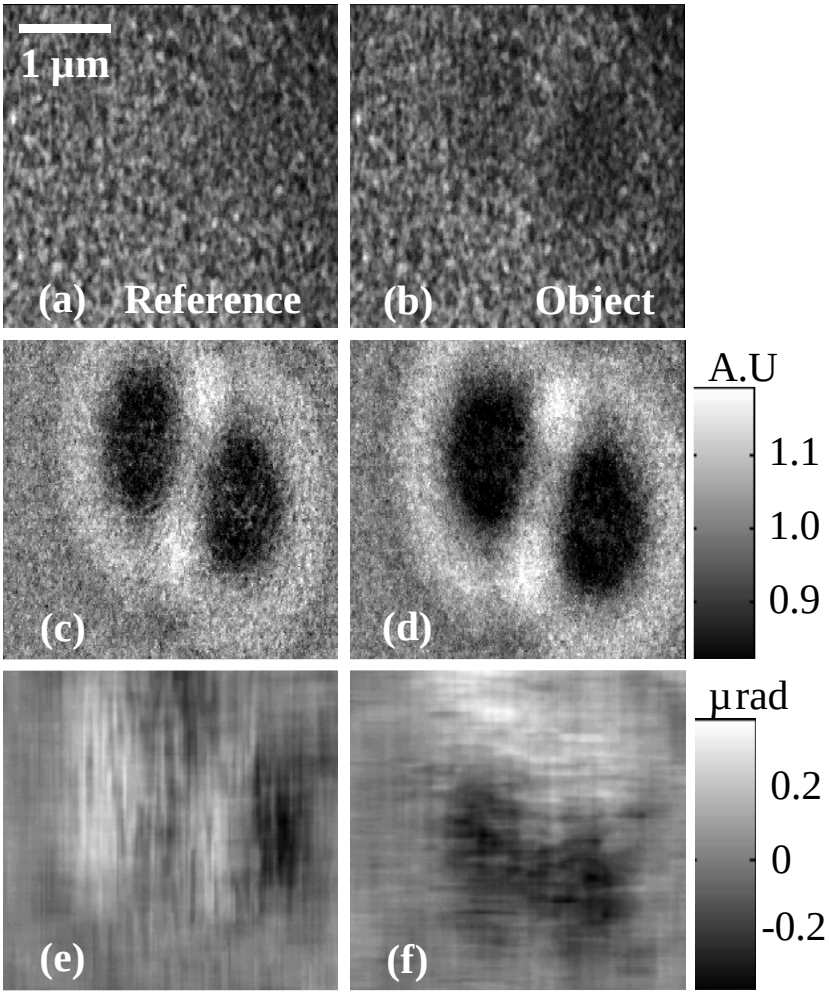

Figure 12.8: (a) Speckle image without any sample in the beam (reference image). (b) Speckle image with the sample in the beam (object image). (c) Absorption image calculated with the two previous speckle images. (d) Absorption image obtained without the scattering membrane in the beam. (e) Horizontal wavefront gradient. (f) Vertical wavefront gradient.

to calculate the differential beam phase. Image (a) was acquired without any sample present in the beam (reference image) while image (b) was recorded with the sample introduced in the beam (object image). From these two images, an absorption image can be calculated from the ratio of the pixel counts in each pixel. For comparison, the absorption image obtained when the speckle membrane is present in the beam (c) and when it is not (d) are displayed side by side in Fig. 12.8: as the displacement of the speckle pattern is smaller than the grain size, the absorption image obtained with the membrane resembles the one obtained without the membrane in the beam.

The vertical (e) and horizontal (f) wavefront gradients were derived after calculating the displacement vector for each subset of 21 pixel width centered on each pixel using Eq. 12.1. It can be observed that the speckle grains frequencies have disappeared from the image.

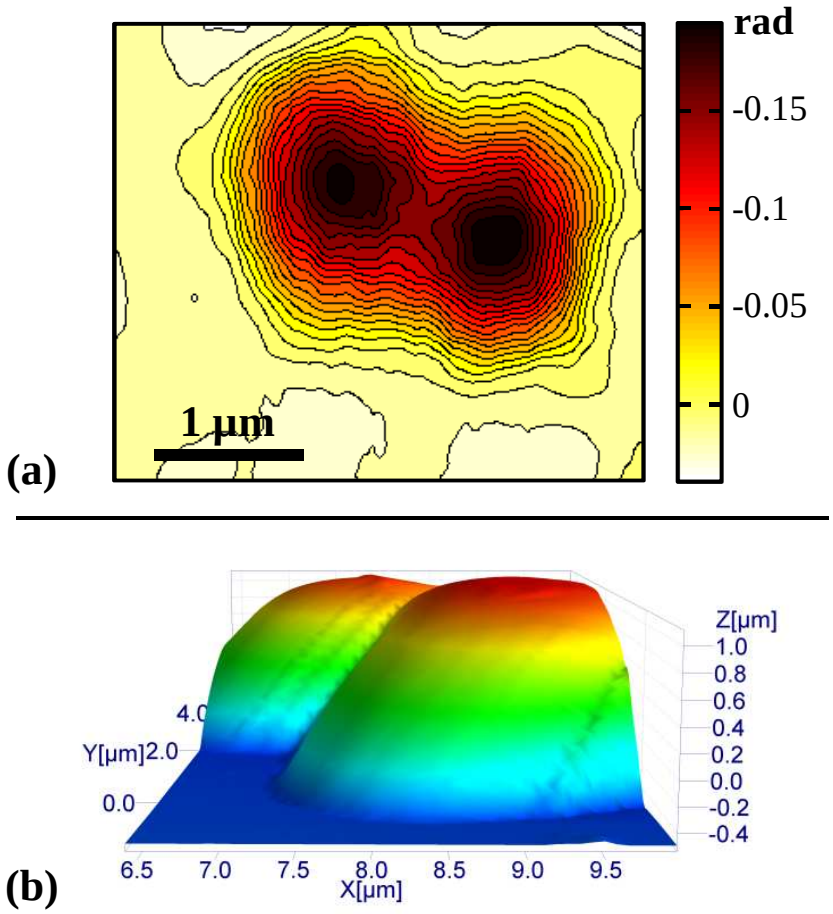

Figure 12.9: (a) Reconstructed map of the phase shift introduced by the micron thick polystyrene spheres. One can clearly distinguish the two spheres. (b) Image from an atomic force microscopy scan of some of the polystyrene spheres.

The reconstructed phase shift map calculated using a 2D Fourier integration scheme [146], is shown in Fig. 12.9.(a) where the two polystyrene spheres are distinguishable and a liquid interface can be seen between them. For this wavefront reconstruction, particular care was taken for the integration step in the algorithm to match the equivalent pixel size of the detector in the plane of the wavefront sampling, i.e in the plane of the membrane (270 nm in our case). The maximum phase shift induced by the spheres is equal to $\sim 0.022\ \lambda$ while the expected value would be $0.016\ \lambda$ for a single micron size sphere, considering the decrement from unity of the real part of the refractive index of the polystyrene spheres to be $\delta = 1.96e - 6$. Atomic Force Microscopy scans performed on the same spheres revealed a maximum size of 1.5 μm (peak to valley value) as shown in Fig. 12.9.(b), which eventually corroborates well with our X-ray measurements. In addition, the standard deviation in an area of known constant phase is approximately 20 $nrad$: that indicates the good sensitivity and stability of the method. Considering that our DIC algorithm has an accuracy of better than 0.05 pixel, the smallest displacement vector measurable was of < 320 nm suggesting using

Eq. 12.2 a sensitivity value better than 90 *n*rad.

As a conclusion, the technique demonstrates untouched sensitivity to phase shift when increasing the spatial resolution through magnification. The process still requires a single exposure of the sample that makes the technique very attractive to study dynamic samples. Moreover, there is a scope to further increase the sensitivity of the technique by at least one order of magnitude, by a combination of increasing the distance L3 and using a smaller pixel-size detector. If the flux density becomes an issue then the FZP can be replaced by a more efficient optics like a reflecting mirror, which will substantially increase both the focusing efficiency and the usable energy bandwidth[137]. The method presented is hence very attractive for nanoscale imaging of both static and dynamic samples made of light materials, such as the ones of interest in the field of biology and medical sciences.

12.3 Conclusions

The successful demonstration of sub-micron phase contrast imaging by two different techniques has been presented. One could notice similarity on several aspects: both are full field techniques employing a FZP as focusing element and measuring the differential wavefront gradient by wavefront modulation. Nevertheless, the XGI implementation was arranged such that the sample was located in focus and the XST implementation within an out-of-focus projection geometry. While the first geometry set up provides better edge contrast the second permits the use of a larger magnification ratio.

It is worthwhile to discuss here about the advantages that the generalized scheme of Sec. 7.2 would offer in a similar configuration. The membrane scanning scheme is expected to provide, equivalently to the micro imaging XST method, a fine sensitivity thanks to the possibility of tuning the size of the speckle grains and of employing a long propagation distance. In addition, a really high resolution is achievable using a high magnification ratio: similar to the 2D XGI scheme, it would have a pixel size resolution. As a future perspective, it is reasonable to think about potential achievement of sub 50-nm size structure resolution using the projection setup and a large bandwidth, high flux efficiency focusing optics.

13 Conclusions

This thesis aimed at developing at-wavelength metrology methods usable at synchrotrons. The project was motivated by the demand for X-ray phase sensing methods to further improve the manufacturing process and therefore the performance of X-ray optics. The investigated methods were near field methods based on the use of either gratings or speckle. Grating interferometry, an already quite spread method in the synchrotron community for imaging, still required additional work for routine metrology applications. Studies were carried out on this device and a derivative method for mirror characterization was developed. Regarding speckle based method, no such method was previously available in the X-ray regime. However, recent advances opened up perspectives for the development of a class of techniques using randomly scattering phase objects. Performance and possible applications of the techniques were then studied.

13.1 Scientific contribution

Several new methods have been developed during this project. Although they first aimed at investigating the quality and performance of optical elements, the improved sensitivity and spatial resolution of the developed methods permitted to widen the field of applications to microscopy.

The following methods were investigated or improved:

- **Grating interferometry**: The grating interferometer was a device already widespread in the hard X-ray community at the time of the project inception. Several competitive groups still spend important resources in the development and improvement of the XGI, with for instance new applications at X-FEL fa-

cilities. The effort in this project was put on the improvement of the spatial resolution and sensitivity of the device to push its metrology performance forward. Most of the XGI work in this project consisted in optimization and application to metrology cases in the frame of optics characterization.

- **X-ray Speckle Tracking technique**: The XST technique is an *original* technique developed at the beginning of the project and, since then, has been employed for various applications. Despite the simultaneous publication of a strongly related technique by a competitive group [125], extensive developments of our technique permitted us to keep an edge over competition. For instance, demonstration of the technique's ability for micro imaging, optics characterization and adaptive optics optimization were achieved.

- **X-ray generalized stepping scheme**: This *new* technique can be seen as a merging of the XST and XGI techniques, borrowing principles from both techniques. This advanced scheme then provides several advantages in terms of spatial resolution and sensitivity. Despite being only at its early development stage, the technique lets one envisage several applications and improvements: considering the high magnification ratio accessible combined with the moderate flux requirements, the method is a promising candidate for micro-imaging at moderate brilliance beamlines.

- **X-ray grating deflectometry**: The development of this method, *novel* in the hard X-ray regime, was motivated by the Ion Beam Figuring project of the ESRF with the goal of determining online the profile of mirrors. The technique uses a single absorption grating and is conceptually related to both the LTP instrument and the pencil beam technique. Thanks to the more advanced numerical processing schemes, one can access higher accuracy than the pencil beam technique combined with a greatly improved sampling resolution. The technique is expected to be of interest to optics manufacturing applications as it provides fine metrology maps of reflective optics under real working environment.

The applications attempted and presented in this thesis relate to both metrology and microscopy topics. In carrying out the presented research, special emphasis was put on deriving higher sensitivity and greater resolution. The XST and XGI methods were both employed for online metrology of transmission optics and then further for X-ray microscopy. In parallel, the work carried out on the ESRF IBF project permitted to progress on the potential of the at-wavelength metrology as a feedback for an X-

ray optics manufacturing process. During the final period of this thesis project, the effectiveness of the developed techniques was exemplified by the successful optimization of a high quality super-polished adaptive optics.

13.2 Perspectives and opinions

The core of this Ph.D. work concerns phase sensing and despite the quite ambitious title given to the XST paper [137], it would be pretentious to claim the existence of an absolute phase sensing method. Each technique finds applications depending on its specific advantages as already discussed in Sec. 6.3. Nonetheless, some further personal points of view are added here. They result from the experience acquired in the course of this three year project.

- Online characterization of X-ray mirrors is a complex task due to the necessity of employing grazing incidence. The grating based deflectometry method developed is a sophisticated version of the pencil beam technique that provides improved sampling resolution and sensitivity for reflective optics characterization. Even though further mechanical and environmental optimization are required for achieving routine sub micro-radian measurements. The technique can replace, at small additional cost, the crude pencil beam technique by substituting an absorption grating to the probing pair of slits.

- Regarding the XGI, there is no doubt that it presents several important advantages for imaging applications. However, at-wavelength metrology applications do not directly benefit from these advantages. I have now a somewhat sceptical opinion of the XGI's ability to measure absolute wavefront using the phase stepping mode. This opinion comes about from the experience of analyzing several XGI data wherein measurement artifacts due to the grating defects were unavoidable: they became problematic especially when the device was used in an absolute mode, i.e in the absence of flat field substraction. It seems to me that these defects are inherent to the production of gratings and preclude artefact-free measurements, especially at low Talbot working orders. In parallel, the shear distance induced by the use of a phase grating as a beam splitter may become an important drawback for metrology applications as it limits the wavefront sampling resolution of the measurements. It would be worthwhile to make further progress on the grating metrology methods based on only absorption gratings,

as it would be a way to by-pass the shear effects, although at the cost of reduced usable photons.

The speckle techniques are original ones and the pioneer experiments presented in this manuscript definitely deserve further systematic studies to assess their potentials. It is in my opinion too early to draw some serious comparison with, for instance, the XGI, subject of investigation for nearly ten years.

- The new stepping generalized scheme will mainly find applications at synchrotrons: it offers the same advantages as the 2D XGI, i.e the phase and scattering mapping of an object, but at a much lower investment cost. One aspect that will make it favorite over its 2D XGI cousin for certain applications is its spatial resolution. As a matter of fact, the method can be applied in a very high magnification geometry and does not suffer from grating shear limitation. Nevertheless, this stepping scheme requires a detector able to resolve the wavefront intensity modulation features, contrary to the 2D XGI. As seen in the theoretical part of the method description (cf. Sec. 7.2.2), the technique is based on an intrinsically incoherent principle. There are then possibilities of employing absorption patterns instead of phase ones in the general stepping scheme to make it compatible with laboratory sources. In contrast, the 2D XGI, which is a special case of the stepping scheme, is likely to find applications at laboratory sources when one wants to map objects at a scale smaller than the detector pixel size.

- The X-ray speckle tracking technique will, in my opinion, reach a large community of users both for metrology and for imaging purposes. As a metrology instrument, the XST technique is surely an efficient alternative to the pencil beam technique. Such substitution would simplify the experimental setup and provide higher sensitivity and beam phase monitoring. For imaging, the technique will find applications when a single exposure process is desired to retrieve the phase. Here, we expect the XST technique to be more robust and efficient than the 2D XGI in the Moiré mode and usable in tomography and in general, to image dynamic processes. I also believe XST has the potential of becoming a valuable tool for applications where the XGI is presently employed, such as at the new compact X-ray sources [185] and X-Free Electron Laser instruments [72] where pulse to pulse variations need to be measured.

As a final word, it is important to point out that at-wavelength metrology is still in its infancy. For a long time, laboratory metrology instruments were able to provide the accuracy necessary for the production of state of the art X-ray optics. Now that the metrology has become the limiting factor in the production of the present and future nanofocusing optics, the use of high-resolution online at-wavelength metrology methods is the way forward. Important improvements in this field are therefore expected. May this contribution be valuable to the community and generate further advances.

Conclusion en français

Cette thèse avait pour but le développement de méthodes de métrologie à la longueur d'onde pour synchrotrons. Elle était motivée par le besoin de méthodes sensibles à la phase des faisceaux de rayons X pour la fabrication d'optiques pour faisceau X de génération supérieure. Les méthodes étudiées s'appuyaient soit sur le speckle en champ proche, soit sur l'utilisation de réseaux. Au commencement de ce projet l'interférométrie à réseaux était déjà une méthode d'imagerie répandue dans les synchrotrons. Toutefois, elle nécessitait encore des améliorations pour pouvoir être utilisée comme instrument de métrologie en ligne de façon routinière. Divers travaux ont été effectués sur cet instrument et une méthode dérivée a été mise au point pour la caractérisation d'optiques X travaillant en réflexion. Concernant les méthodes utilisant le speckle, aucune n'était disponible dans le domaine des rayons X durs. Toutefois, des découvertes récentes laissaient entrevoir des possibilités pour l'exploitation de ce phénomène observable lorsque l'on place un objet diffractant dans un faisceau synchrotron partiellement cohérent. Les performances et les applications possibles des techniques ont donc nécessité une étude approfondie pour les rendre utilisables par le plus grand nombre.

Contribution scientifique

Plusieurs méthodes nouvelles ont été mises au point au cours de cette thèse. Bien que leur but premier concernât la caractérisation en ligne d'optiques, la précision et la résolution spatiale des nouvelles techniques développées ont permis des applications de microscopie.

Les méthodes suivantes ont été conçues ou améliorées.

- **L'interférométrie à réseaux :** Les interféromètres à réseaux étaient des ins-

truments déjà assez répandus dans le milieu synchrotron au début de ce projet, plusieurs groupes consacrant des ressources conséquentes au développement et à l'amélioration de l'interféromètre, par exemple pour son utilisation au sein des nouvelles installations X-FEL. Au cours de ce projet, l'effort a été mis sur l'amélioration de la sensibilité et de la résolution spatiale de l'instrument afin d'optimiser ses performances pour la métrologie de routine. Plusieurs applications de l'interféromètre furent mises en œuvre pour la caractérisation en ligne d'optiques pour rayons X.

- **Le suivi de speckle X :** La méthode de suivi de speckle est une technique originale de mesure de la phase d'un faisceau de rayons X. Elle a été mise au point au début de cette thèse et ensuite largement employée. Une méthode comparable fut publiée simultanément par un groupe concurrent [125], mais des améliorations constantes nous ont permis de garder une avance sur nos concurrents. Ainsi, la démonstration a été faite de l'efficacité de la technique pour la microscopie de rayons X, la caractérisation d'éléments optiques et l'optimisation d'optiques adaptatives.

- **La méthode à pas généralisée :** Cette nouvelle technique peut être interprétée comme l'intersection de la technique du suivi de speckle en ligne et de l'interférométrie à réseaux ; elle emprunte des principes aux deux techniques. Cette procédure de traitement élaborée fournit plusieurs avantages en termes de résolution spatiale et de précision. En dépit de sa jeunesse, les études préliminaires laissent envisager de multiples applications. Du fait du grossissement important accessible avec cette technique et des faibles contraintes en flux qu'elle impose, des applications d'imagerie à l'échelle nanométrique peuvent être envisagées.

- **La deflectometrie à réseaux :** Cette méthode fut mise au point afin de pouvoir déterminer en ligne le profil de surface d'un miroir X. Cette problématique était soulevée notamment par le projet IBF conduit au sein de l'ESRF. La technique est basée sur l'utilisation d'un seul réseau en absorption et peut être conceptuellement rapprochée de la technique du faisceau en pinceau. Grâce à des méthodes numériques plus avancées, elle permet de dépasser les performances de la technique du faisceau en pinceaux, non seulement en termes de précision, mais aussi de résolution. Cette méthode trouve des applications dans le domaine de la production d'optiques où des cartes topographiques de haute précision et en conditions réelles de fonctionnement sont nécessaires.

Les applications présentées dans ce manuscrit concernent les domaines de la métrologie et de la microscopie. Au cours des recherches, les efforts portèrent plus particulièrement sur l'optimisation de la résolution des méthodes. Les capacités des techniques ont été démontrées dans de multiples applications. Ainsi, les deux techniques de suivi de speckle et d'interférométrie furent employées pour la caractérisation métrologique en ligne d'optiques en transmission et pour la microscopie. En parallèle, les travaux conduits sur le projet IBF de l'ESRF ont permis l'étude de l'intégration de la métrologie en ligne dans la boucle de production d'optique pour rayons X. Vers la fin du projet, l'efficacité des méthodes développées pour l'optimisation d'optique adaptative fut démontrée dans le cas d'un miroir bimorphe multi-electrodes de haute qualité.

Bibliography

[1] J. Als-Nielsen and D. McMorrow, *Elements of Modern X-ray Physics*. John Wiley and Sons, 2001.

[2] H. Winick, G. Brown, K. Halbach, and J. Harris., "Wiggler and undulator magnets," *Physics Today*, vol. 34:5, 1981.

[3] H. Wiedemann, *Synchrotron Radiation*. Springer, 2002.

[4] P. J. Duke, *Synchrotron Radiation: Production and Properties*. Oxford University Press, 2009.

[5] J. W. Goodman, *Statistical Optics*. John Wiley and Sons, 1985.

[6] D. Vaughan, "X-ray data booklet. Center for X-ray optics. [tables]," Tech. Rep. LBL-PUB-490, 1985.

[7] D. M. Paganin, *Coherent X-ray Optic*. England: Oxford Series on Synchrotron Radiation, 2006.

[8] J. Goodman, *Introduction to Fourier Optics*, 3rd ed. Roberts and Company Publishers, 2005.

[9] M. Born and E. Wolf, *Principles of Optics: Electromagnetic Theory of Propagation, Interference and Diffraction of Light*, 7th ed. Cambridge University Press, 1999.

[10] L. Bragg, "The development of X-ray analysis," *Contemporary Physics*, vol. 17, pp. 103–4, 1976.

[11] M. Dierolf, A. Menzel, P. Thibault, P. Schneider, C. M. Kewish, R. Wepf, O. Bunk, and F. Pfeiffer, "Ptychographic X-ray computed tomography at the nanoscale," *Nature*, vol. 467, pp. 436–9, 2010.

[12] P. Thibault, M. Dierolf, A. Menzel, O. Bunk, C. David, and F. Pfeiffer, "High-resolution scanning X-ray diffraction microscopy," *Science*, vol. 321, pp. 379–82, 2008.

[13] A. Schropp, P. Boye, J. M. Feldkamp, R. Hoppe, J. Patommel, D. Samberg, S. Stephan, K. Giewekemeyer, R. N. Wilke, T. Salditt, J. Gulden, A. P. Mancuso, I. A. Vartanyants, E. Weckert, S. Schoder, M. Burghammer, and C. G. Schröer, "Hard X-ray nanobeam characterization by coherent diffraction microscopy," *Applied Physics Letters*, vol. 96, p. 091102, 2010.

[14] J. R. Fienup, "Phase retrieval algorithms: a comparison," *Applied Optics*, vol. 21, pp. 2758–69, 1982.

[15] M. M. Woolfson, "Direct methods in crystallography," *Reports on Progress in Physics*, vol. 34, p. 369, 1971.

[16] C. M. Kewish, M. Guizar-Sicairos, C. Liu, J. Qian, B. Shi, C. Benson, A. M. Khounsary, J. Vila-Comamala, O. Bunk, J. R. Fienup, A. T. Macrander, and L. Assoufid, "Reconstruction of an astigmatic hard X-ray beam and alignment of K-B mirrors from ptychographic coherent diffraction data," *Optics Express*, vol. 18, pp. 23 420–7, 2010.

[17] C. M. Kewish, P. Thibault, M. Dierolf, O. Bunk, A. Menzel, J. Vila-Comamala, K. Jefimovs, and F. Pfeiffer, "Ptychographic characterization of the wavefield in the focus of reflective hard X-ray optics," *Ultramicroscopy*, vol. 110, pp. 325–9, 2010.

[18] H. F. Talbot, "Facts relating to optical science," *Phil. Mag, 3rd Series*, vol. 9, p. 401, 1836.

[19] T. J. Suleski, "Generation of Lohmann images from binary-phase Talbot array illuminators," *Applied Optics*, vol. 36, pp. 4686–91, 1997.

[20] J. T. Winthrop and C. R. Worthington, "Theory of Fresnel images. I. Plane periodic objects in monochromatic light," *Journal of the Optical Society of America*, vol. 55, pp. 373–80, 1965.

[21] R. F. Edgar, "The Fresnel diffraction images of periodic structures," *Optica Acta: International Journal of Optics*, vol. 16, no. 3, pp. 281–7, 1969.

[22] J. P. Guigay, "On Fresnel diffraction by one-dimensional periodic objects, with application to structure determination of phase objects," *Optica Acta: International Journal of Optics*, vol. 18, pp. 677–82, 1971.

[23] P. Cloetens, J. P. Guigay, C. De Martino, J. Baruchel, and M. Schlenker, "Fractional Talbot imaging of phase gratings with hard x rays," *Optics Letters*, vol. 22, pp. 1059–61, 1997.

[24] R. Cerbino, L. Peverini, M. A. C. Potenza, A. Robert, P. Bösecke, and M. Giglio, "X-ray scattering information obtained from near-field speckle," *Nature Physics*, vol. 4, pp. 238–43, 2008.

[25] E. Ziegler, J. Hoszowska, T. Bigault, L. Peverini, J. Y. Massonnat, and R. Hustache, "The ESRF BM05 metrology beamline: Instrumentation and performance upgrade," *AIP Conference Proceedings*, vol. 705, pp. 436–9, 2004.

[26] K. J. S. Sawhney, I. P. Dolbnya, M. K. Tiwari, L. Alianelli, S. M. Scott, G. M. Preece, U. K. Pedersen, and R. D. Walton, "A test beamline on Diamond Light Source," *AIP Conference Proceedings*, vol. 1234, pp. 387–90, 2010.

[27] "Experimental physics and industrial control system (EPICS)." [Online]. Available: http://www.aps.anl.gov/epics/docs/index.php

[28] "GDA - Software for science." [Online]. Available: http://opengda.org

[29] H. Mimura, S. Handa, T. Kimura, H. Yumoto, D. Yamakawa, H. Yokoyama, S. Matsuyama, K. Inagaki, K. Yamamura, Y. Sano, K. Tamasaku, Y. Nishino, M. Yabashi, T. Ishikawa, and K. Yamauchi, "Breaking the 10 nm barrier in hard X-ray focusing," *Nature Physics*, vol. 6, pp. 122–5, 2010.

[30] A. Snigirev, V. Kohn, I. Snigireva, A. Souvorov, and B. Lengeler, "Focusing high-energy X-rays by compound refractive lenses," *Applied Optics*, vol. 37, pp. 653–62, 1998.

[31] B. Lengeler, C. G. Schröer, B. Benner, A. Gerhardus, T. F. Günzler, M. Kuhlmann, J. Meyer, and C. Zimprich, "Parabolic refractive X-ray lenses," *Journal of Synchrotron Radiation*, vol. 9, no. 3, pp. 119–24, 2002.

[32] K. Evans-Lutterodt, J. Ablett, A. Stein, C.-C. Kao, D. Tennant, F. Klemens, A. Taylor, C. Jacobsen, P. Gammel, H. Huggins, G. Bogart, S. Ustin, and L. Ocola, "Single-element elliptical hard X-ray micro-optics," *Optics Express*, vol. 11, pp. 919–26, 2003.

[33] A. J. Fresnel, *Oeuvres Complètes d'Augustin Fresnel*. Imprimerie Impériale, Paris, 1866, ch. Calcul de l'intensité de la lumière au centre de l'ombre d'un ecran et d'une ouverture circulaires eclairés par un point radieux.

[34] C. G. Schröer, "Focusing hard X-rays to nanometer dimensions using Fresnel zone plates," *Physical Review B*, vol. 74, p. 033405, 2006.

[35] D. H. Bilderback, A. K. Freund, G. S. Knapp, and D. M. Mills, "The historical development of cryogenically cooled monochromators for third-generation synchrotron radiation sources," *Journal of Synchrotron Radiation*, vol. 7, pp. 53–60, 2000.

[36] I. V. Kozhevnikov, I. N. Bukreeva, and E. Ziegler, "Design of X-ray supermirrors," *Nuclear Instruments and Methods in Physics Research Section A: Accelerators, Spectrometers, Detectors and Associated Equipment*, vol. 460, pp. 424–43, 2001.

[37] C. Morawe, E. Ziegler, J.-C. Peffen, and I. V. Kozhevnikov, "Design and fabrication of depth-graded X-ray multilayers," *Nuclear Instruments and Methods in Physics Research Section A: Accelerators, Spectrometers, Detectors and Associated Equipment*, vol. 493, pp. 189–98, 2002.

[38] H. Yan, "X-ray nanofocusing by kinoform lenses: a comparative study using different modeling approaches," *Physical Review B*, vol. 81, p. 075402, 2010.

[39] S. Goto, M. Yabashi, K. Tamasaku, and T. Ishikawa, "Characterization of beryllium windows for coherent X-ray optics," *AIP Conference Proceedings*, vol. 879, pp. 1057–60, 2007.

[40] J.-C. Labiche, "The FReLoN camera," 2007. [Online]. Available: http://www.esrf.eu/UsersAndScience/Experiments/Imaging/ID19/BeamlineDescription/Detectors/Frelon_intro

[41] PCO, "The PCO camera," 2012. [Online]. Available: http://www.pco.de/applications/physical-science/pco4000/

[42] S. G. Alcock, K. J. S. Sawhney, S. Scott, U. Pedersen, R. Walton, F. Siewert, T. Zeschke, F. Senf, T. Noll, and H. Lammert, "The Diamond-NOM: a non-contact profiler capable of characterizing optical figure error with sub-nanometre repeatability," *Nuclear Instruments and Methods in Physics Research Section A: Accelerators, Spectrometers, Detectors and Associated Equipment*, pp. 224–8, 2010.

[43] A. V. Rommeveaux, B. Lantelme, and R. Barrett, "ESRF metrology laboratory: overview of instrumentation, measurement techniques, and data analysis," vol. 7801, pp. 780 107–11, 2010.

[44] E. b. Yoshizawa, *Handbook of Optical Metrology: principles and applications*. CRC Press, 2009.

[45] R. Soufli, M. J. Pivovaroff, S. L. Baker, J. C. Robinson, E. M. Gullikson, T. J. McCarville, P. M. Stefan, A. L. Aquila, J. Ayers, M. A. McKernan, and R. M. Bionta, "Advances in X-ray/EUV optics and components III," C. M. S. Goto, A. Khounsaryc, Ed., vol. 7077. SPIE, 2008, p. 707716.

[46] E. Ziegler, L. Peverini, N. Vaxelaire, A. Cordon-Rodriguez, A. Rommeveaux, I. V. Kozhevnikov, and J. Susini, "Evolution of surface roughness in silicon X-ray mirrors exposed to a low-energy ion beam," *Nuclear Instruments and Methods in Physics Research Section A: Accelerators, Spectrometers, Detectors and Associated Equipment*, vol. 616, pp. 188–92, 2010.

[47] O. Hignette, A. K. Freund, and E. Chinchio, "Incoherent X-ray mirror surface metrology," vol. 3152, pp. 188–99.

[48] P. Naulleau, P. Batson, P. Denham, D. Richardson, and J. Underwood, "An in situ scanning slit alignment system for Kirkpatrick Baez optics," *Optics Communications*, vol. 212, pp. 225–33, 2002.

[49] P. Kirkpatrick and A. V. Baez, "Formation of optical images by X-rays," *Journal of the Optical Society of America*, vol. 38, pp. 766–73, 1948.

[50] J. Miao, P. Charalambous, J. Kirz, and D. Sayre, "Extending the methodology of X-ray crystallography to allow imaging of micrometre-sized non-crystalline specimens," *Nature*, vol. 400, pp. 342–4, 1999.

[51] G. J. Williams, M. A. Pfeifer, I. A. Vartanyants, and I. K. Robinson, "Three-dimensional imaging of microstructure in Au nanocrystals," *Physical Review Letters*, vol. 90, p. 175501, 2003.

[52] F. Livet and M. Sutton, "X-ray coherent scattering in metal physics," *Comptes Rendus Physique*, vol. 13, pp. 227–36, 2012.

[53] A. Schropp, R. Hoppe, J. Patommel, D. Samberg, F. Seiboth, S. Stephan, G. Wellenreuther, G. Falkenberg, and C. G. Schröer, "Hard X-ray scanning microscopy with coherent radiation: beyond the resolution of conventional X-ray microscopes," *Applied Physics Letters*, vol. 100, p. 253112, 2012.

[54] U. Bonse and M. Hart, "An X-ray interferometer," *Applied Physics Letters*, vol. 6, p. 155, 1965.

[55] A. Momose, T. Takeda, Y. Itai, and K. Hirano, "Phase-contrast X-ray computed tomography for observing biological soft tissues," *Nature Medical*, vol. 2, pp. 473–5, 1996.

[56] P. Cloetens, W. Ludwig, J. Baruchel, D. V. Dyck, J. V. Landuyt, J. P. Guigay, and M. Schlenker, "Holotomography: quantitative phase tomography with micrometer resolution using hard synchrotron radiation X-rays," *Applied Physics Letters*, vol. 75, pp. 2912–4, 1999.

[57] T. E. Gureyev, S. Mayo, S. W. Wilkins, D. Paganin, and A. W. Stevenson, "Quantitative in-line phase-contrast imaging with multienergy X-rays," *Physical Review Letters*, vol. 86, pp. 5827–30, 2001.

[58] D. Paganin, S. C. Mayo, T. E. Gureyev, P. R. Miller, and S. W. Wilkins, "Simultaneous phase and amplitude extraction from a single defocused image of a homogeneous object," *Journal of Microscopy*, vol. 206, pp. 33–40, 2002.

[59] T. Weitkamp, D. Haas, D. Wegrzynek, and A. Rack, "ANKAphase: software for single-distance phase retrieval from inline X-ray phase-contrast radiographs," *Journal of Synchrotron Radiation*, vol. 18, pp. 617–29, 2011.

[60] M. Langer, P. Cloetens, J.-P. Guigay, and F. Peyrin, "Quantitative comparison of direct phase retrieval algorithms in in-line phase tomography," *Medical Physics*, vol. 35, pp. 4556–66, 2008.

[61] P. Coan, F. Bamberg, P. C. Diemoz, A. Bravin, K. Timpert, E. Mutzel, J. G. Raya, S. Adam-Neumair, M. F. Reiser, and C. Glaser, "Characterization of osteoarthritic and normal human patella cartilage by computed tomography X-ray phase-contrast imaging: a feasibility study," *Investigative Radiology*, vol. 45, pp. 437–44, 2010.

[62] P. Mercere, S. Bucourt, G. Cauchon, D. Douillet, G. Dovillaire, K. A. Goldberg, M. Idir, X. Levecq, T. Moreno, P. P. Naulleau, S. Rekawa, and P. Zeitoun, "X-ray beam metrology and X-ray optic alignment by Hartmann wavefront sensing," vol. 5921, pp. 592 109–10.

[63] P. Mercère, M. Idir, T. Moreno, G. Cauchon, G. Dovillaire, X. Levecq, L. Couvet, S. Bucourt, and P. Zeitoun, "Automatic alignment of a Kirkpatrick-Baez active optic by use of a soft X-ray Hartmann wavefront sensor," *Optics Letters*, vol. 31, pp. 199–201, 2006.

[64] A. Olivo and R. Speller, "A coded-aperture technique allowing X-ray phase contrast imaging with conventional sources," *Applied Physics Letters*, vol. 91, pp. 074 106–3, 2007.

[65] A. Olivo, K. Ignatyev, P. R. T. Munro, and R. D. Speller, "Noninterferometric phase-contrast images obtained with incoherent X-ray sources," *Applied Optics*, vol. 50, pp. 1765–9, 2011.

[66] C. David, B. Nöhammer, H. H. Solak, and E. Ziegler, "Differential X-ray phase contrast imaging using a shearing interferometer," *Applied Physics Letters*, vol. 81, pp. 3287–9, 2002.

[67] A. Momose, S. Kawamoto, I. Koyama, Y. Hamaishi, K. Takai, and Y. Suzuki, "Demonstration of X-ray Talbot interferometry," *Japanese Journal Of Applied Physics*, vol. 42, p. 866, 2003.

[68] F. Pfeiffer, T. Weitkamp, O. Bunk, and C. David, "Phase retrieval and differential phase-contrast imaging with low-brilliance X-ray sources," *Nature Physics*, vol. 2, pp. 258–61, 2006.

[69] D. X. P. Group, *XFEL: The European X-ray Free-electron Laser : Technical Design Report*. DESY, 2006.

[70] I. Zanette, M. Bech, A. Rack, G. Le Duc, P. Tafforeau, C. David, J. Mohr, F. Pfeiffer, and T. Weitkamp, "Trimodal low-dose X-ray tomography," *Proceedings of the National Academy of Sciences*, 2012.

[71] T. Weitkamp, B. Nöhammer, A. Diaz, C. David, and E. Ziegler, "X-ray wavefront analysis and optics characterization with a grating interferometer," *Applied Physics Letters*, vol. 86, pp. 054 101–3, 2005.

[72] S. Rutishauser, L. Samoylova, J. Krzywinski, O. Bunk, J. Grunert, H. Sinn, M. Cammarata, D. M. Fritz, and C. David, "Exploring the wavefront of hard X-ray free-electron laser radiation," *Nature Communication*, vol. 3, p. 947, 2012.

[73] *Handbook of Optical Metrology: Principles and Applications*. Yokohama, Japan: CRC Press, 2009.

[74] J. Wyant and K. Creath, "Applied optics and optical engineering, Volume XI," 1992.

[75] V. Ronchi, "Forty years of history of a grating interferometer," *Applied Optics*, vol. 3, pp. 437–51, 1964.

[76] S. Yokozeki and T. Suzuki, "Shearing interferometer using the grating as the beam splitter," *Applied Optics*, vol. 10, pp. 1575–80, 1971.

[77] A. W. Lohmann and D. E. Silva, "An interferometer based on the Talbot effect," *Optics Communications*, vol. 2, pp. 413–5, 1971.

[78] I. Zanette, C. David, S. Rutishauser, and T. Weitkamp, "2D grating simulation for X-ray phase-contrast and dark-field imaging with a Talbot interferometer," *AIP Conference Proceedings*, vol. 1221, pp. 73–9, 2010.

[79] C. David, J. Bruder, T. Rohbeck, C. Grunzweig, C. Kottler, A. Diaz, O. Bunk, and F. Pfeiffer, "Fabrication of diffraction gratings for hard X-ray phase contrast imaging," *Microelectronic Engineering*, vol. 84, 2007.

[80] S. Rutishauser, M. Bednarzik, I. Zanette, T. Weitkamp, M. Börner, J. Mohr, and C. David, "Fabrication of two-dimensional hard X-ray diffraction gratings," *Microelectronic Engineering*, vol. 101, pp. 12–6, 2013.

[81] C. David, B. Nöhammer, and E. Ziegler, "Wavelength tunable diffractive transmission lens for hard x rays," *Applied Physics Letters*, vol. 79, pp. 1088–90, 2001.

[82] H. W. Schnopper, L. P. Van Speybroeck, J. P. Delvaille, A. Epstein, E. Källne, R. Z. Bachrach, J. Dijkstra, and L. Lantward, "Diffraction grating transmission efficiencies for XUV and soft X-rays," *Applied Optics*, vol. 16, pp. 1088–91, 1977.

[83] J. P. Guigay, C. Morawe, V. Mocella, and C. Ferrero, "An analytical approach to estimating aberrations in curved multilayer optics for hard X-rays: 1. derivation of caustic shapes," *Optics Express*, vol. 16, no. 16, pp. 12 050–9, 2008.

[84] F. Krejci, J. Jakubek, and M. Kroupa, "Single grating method for low dose 1-D and 2-D phase contrast X-ray imaging," *Journal of Instrumentation*, vol. 6, p. C01073, 2011.

[85] E. Reznikova, J. Mohr, M. Boerner, V. Nazmov, and P.-J. Jakobs, "Soft X-ray lithography of high aspect ratio SU8 submicron structures," *Microsystem Technologies*, vol. 14, pp. 1683–8, 2008.

[86] S. Rutishauser, I. Zanette, T. Donath, A. Sahlholm, J. Linnros, and C. David, "Structured scintillator for hard X-ray grating interferometry," *Applied Physics Letters*, vol. 98, pp. 171 107–3, 2011.

[87] K. Creath, *Phase-shifting interferometry techniques*, ser. Progress in Optics, 1988, vol. 26.

[88] P. Krzysztof, "Moiré methods in interferometry," *Optics and Lasers in Engineering*, vol. 8, pp. 147–70, 1988.

[89] K. A. Goldberg and J. Bokor, "Fourier-transform method of phase-shift determination," *Applied Optics*, vol. 40, pp. 2886–94, 2001.

[90] M. V. R. K. Murty and E. C. Hagerott, "Rotational-shearing interferometry," *Applied Optics*, vol. 5, pp. 615–9, 1966.

[91] T. Weitkamp, A. Diaz, C. David, F. Pfeiffer, M. Stampanoni, P. Cloetens, and E. Ziegler, "X-ray phase imaging with a grating interferometer," *Optics Express*, vol. 13, pp. 6296–304, 2005.

[92] T. Donath, M. Chabior, F. Pfeiffer, O. Bunk, E. Reznikova, J. Mohr, E. Hempel, S. Popescu, M. Hoheisel, M. Schuster, J. Baumann, and C. David, "Inverse geometry for grating-based X-ray phase-contrast imaging," *Journal of Applied Physics*, vol. 106, pp. 054 703–7, 2009.

[93] S. A. McDonald, F. Marone, C. Hintermuller, G. Mikuljan, C. David, F. Pfeiffer, and M. Stampanoni, "Advanced phase-contrast imaging using a grating interferometer," *Journal of Synchrotron Radiation*, vol. 16, pp. 562–72, 2009.

[94] I. Zanette, T. Weitkamp, T. Donath, S. Rutishauser, and C. David, "Two-dimensional X-ray grating interferometer," *Physical Review Letters*, vol. 105, no. 24, p. 248102, 2010.

[95] S. Rutishauser, I. Zanette, T. Weitkamp, T. Donath, and C. David, "At-wavelength characterization of refractive X-ray lenses using a two-dimensional grating interferometer," *Applied Physics Letters*, vol. 99, p. 221104, 2011.

[96] A. Momose, Y. Takeda, W. Yashiro, A. Takeuchi, and Y. Suzuki, "X-ray phase tomography with a Talbot interferometer in combination with an X-ray imaging microscope," *Journal of Physics: Conference Series*, vol. 186, p. 012044, 2009.

[97] A. Momose, W. Yashiro, M. Moritake, Y. Takeda, K. Uesugi, A. Takeuchi, Y. Suzuki, M. Tanaka, and T. Hattori, "Biomedical imaging by Talbot-type X-ray phase tomography," U. Bonse, Ed., vol. 6318. SPIE, 2006, p. 63180.

[98] T. Weitkamp, A. Diaz, B. N'öhammer, F. Pfeiffer, M. Stampanoni, E. Ziegler, and C. David, "Moiré interferometry formulas for hard X-ray wavefront sensing," A. M. Khounsary, U. Dinger, and K. Ota, Eds., vol. 5533. SPIE, 2004, pp. 140–4.

[99] H. Wang, K. Sawhney, S. Berujon, E. Ziegler, S. Rutishauser, and C. David, "X-ray wavefront characterization using a rotating shearing interferometer technique," *Optics Express*, vol. 19, pp. 16 550–9, 2011.

[100] M. Takeda, H. Ina, and S. Kobayashi, "Fourier-transform method of fringe-pattern analysis for computer-based topography and interferometry," *Journal of the Optical Society of America*, vol. 72, pp. 156–60, 1982.

[101] Q. Kemao, "Windowed Fourier transform for fringe pattern analysis," *Applied Optics*, vol. 43, pp. 2695–702, 2004.

[102] L. R. Watkins, S. M. Tan, and T. H. Barnes, "Determination of interferometer phase distributions by use of wavelets," *Optics Letters*, vol. 24, pp. 905–7, 1999.

[103] H. Itoh, K. Nagai, G. Sato, K. Yamaguchi, T. Nakamura, T. Kondoh, C. Ouchi, T. Teshima, Y. Setomoto, and T. Den, "Two-dimensional grating-based X-ray phase-contrast imaging using Fourier transform phase retrieval," *Optics Express*, vol. 19, pp. 3339–46, 2011.

[104] D. C. Ghiglia and L. A. Romero, "Minimum Lp-norm two-dimensional phase unwrapping," *Journal of the Optical Society of America A*, vol. 13, pp. 1999–2013, 1996.

[105] T. J. Flynn, "Two-dimensional phase unwrapping with minimum weighted discontinuity," *Journal of the Optical Society of America*, vol. 16, 1997.

[106] J. M. Bioucas-Dias and Valadao, "Phase unwrapping via Graph Cut," *IEEE Transactions on Image Processing*, 2007.

[107] M. A. Herráez, D. R. Burton, M. J. Lalor, and D. B. Clegg, "Robust, simple, and fast algorithm for phase unwrapping," *Applied Optics*, vol. 35, pp. 5847–52, 1996.

[108] M. A. Schofield and Y. Zhu, "Fast phase unwrapping algorithm for interferometric applications," *Optics Letters*, vol. 28, 2003.

[109] S. A. Karout, M. A. Gdeisat, D. R. Burton, and M. J. Lalor, "Two-dimensional phase unwrapping using a hybrid genetic algorithm," *Applied Optics*, vol. 46, pp. 730–43, 2007.

[110] M. Engelhardt, J. Baumann, M. Schuster, C. Kottler, F. Pfeiffer, O. Bunk, and C. David, "High-resolution differential phase contrast imaging using a magnifying projection geometry with a microfocus X-ray source," *Applied Physics Letters*, vol. 90, p. 224101, 2007.

[111] R. S. Sirohi, T. Eiju, K. Matsuda, and T. H. Barnes, "Multiple-beam lateral shear interferometry for optical testing," *Applied Optics*, vol. 34, pp. 2864–70, 1995.

[112] C. Elster and I. Weingartner, "Solution to the shearing problem," *Applied Optics*, vol. 38, pp. 5024–31, 1999.

[113] L. M. Sanchez-Brea and F. J. Torcal-Milla, "Near-field diffraction of gratings with surface defects," *Applied Optics*, vol. 49, pp. 2190–7, 2010.

[114] G. H. Kaufmann, *Advances in Speckle Metrology and Related Techniques*. Wiley-VCH, 2011.

[115] S. Sirohi, *Speckle Metrology (Optical Science and Engineering)*, 1993.

[116] A. Labeyrie, "Attainment of diffraction limited resolution in large telescopes by Fourier analysing speckle patterns in star images," *Annals of Applied Probability*, vol. 6, p. 85, 1970.

[117] J. W. Goodman, *Speckle phenomena in optics; theory and applications.*, 1st ed. Roberts and Company Publishers, Greenwood Village, 2006.

[118] L. Leushacke and M. Kirchner, "Three-dimensional correlation coefficient of speckle intensity for rectangular and circular apertures," *Journal of the Optical Society of America A*, vol. 7, pp. 827–32, 1990.

[119] M. Giglio, M. Carpineti, and A. Vailati, "Space intensity correlations in the near field of the scattered light: a direct measurement of the density correlation function g(r)," *Physical Review Letters*, vol. 85, p. 1416, 2000.

[120] M. Giglio, M. Carpineti, A. Vailati, and D. Brogioli, "Near-field intensity correlations of scattered light," *Applied Optics*, vol. 40, pp. 4036–40, 2001.

[121] R. Cerbino, "Correlations of light in the deep Fresnel region: an extended Van Cittert and Zernike theorem," *Physical Review A*, vol. 75, p. 053815, 2007.

[122] G. Grübel and F. Zontone, "Correlation spectroscopy with coherent X-rays," *Journal of Alloys and Compounds*, vol. 362, pp. 3–11, 2004.

[123] X. Lu, S. G. J. Mochrie, S. Narayanan, A. R. Sandy, and M. Sprung, "X-ray near-field speckle: implementation and critical analysis," *Journal of Synchrotron Radiation*, vol. 18, pp. 823–34, 2011.

[124] M. D. Alaimo, M. A. C. Potenza, M. Manfredda, G. Geloni, M. Sztucki, T. Narayanan, and M. Giglio, "Probing the transverse coherence of an undulator X-ray beam using Brownian particles," *Physical Review Letters*, vol. 103, p. 194805, 2009.

[125] K. S. Morgan, D. M. Paganin, and K. K. W. Siu, "X-ray phase imaging with a paper analyzer," *Applied Physics Letters*, vol. 100, pp. 124 102–4, 2012.

[126] K. A. Nugent, T. E. Gureyev, D. F. Cookson, D. Paganin, and Z. Barnea, "Quantitative phase imaging using hard X-rays," *Physical Review Letters*, vol. 77, p. 2961, 1996.

[127] B. Pan, K. Qian, H. Xie, and A. Asundi, "Two-dimensional digital image correlation for in-plane displacement and strain measurement: a review," *Measurement Science and Technology*, vol. 20, p. 062001, 2009.

[128] W. Zou, K. P. Thompson, and J. P. Rolland, "Differential Shack-Hartmann curvature sensor: local principal curvature measurements," *Journal of the Optical Society of America A*, vol. 25, pp. 2331–7, 2008.

[129] R. Coisson, "Spatial coherence of synchrotron radiation," *Applied Optics*, vol. 34, pp. 904–8, 1995.

[130] W. H. Southwell, "Wave-front estimation from wave-front slope measurements," *Journal of the Optical Society of America*, vol. 70, pp. 998–1006, 1980.

[131] B. L. Henke, E. M. Gullikson, and J. C. Davis, "X-ray interactions: Photoabsorption, scattering, transmission, and reflection at E = 50-30,000 eV, Z = 1-92," *Atomic Data and Nuclear Data Tables*, vol. 54, pp. 181–342, 1993.

[132] A. Momose, "Recent advances in X-ray phase imaging," *Japanese Journal of Applied Physics*, vol. 44, pp. 6355–67, 2005.

[133] K. Iwata, "X-ray shearing interferometer and generalized grating imaging," *Applied Optics*, vol. 48, pp. 886–92, 2009.

[134] F. Pfeiffer, M. Bech, O. Bunk, P. Kraft, E. F. Eikenberry, C. Bronnimann, C. Grunzweig, and C. David, "Hard-X-ray dark-field imaging using a grating interferometer," *Nature Material*, vol. 7, pp. 134–7, 2008.

[135] K. S. Morgan, D. M. Paganin, and K. K. W. Siu, "Quantitative X-ray phase-contrast imaging using a single grating of comparable pitch to sample feature size," *Optics Letters*, vol. 36, pp. 55–7, 2011.

[136] J. Rizzi, T. Weitkamp, N. Guérineau, M. Idir, P. Mercère, G. Druart, G. Vincent, P. da Silva, and J. Primot, "Quadriwave lateral shearing interferometry in an achromatic and continuously self-imaging regime for future X-ray phase imaging," *Optics Letters*, vol. 36, pp. 1398–400, 2011.

[137] S. Berujon, E. Ziegler, R. Cerbino, and L. Peverini, "Two-dimensional X-ray beam phase sensing," *Physical Review Letters*, p. 158102, 2012.

[138] T. Thuering, P. Modregger, T. Grund, J. Kenntner, C. David, and M. Stampanoni, "High resolution, large field of view X-ray differential phase contrast imaging on a compact setup," *Applied Physics Letters*, vol. 99, pp. 041 111–3, 2011.

[139] V. Revol, C. Kottler, R. Kaufmann, I. Jerjen, T. Lüthi, F. Cardot, P. Niedermann, U. Straumann, U. Sennhauser, and C. Urban, "X-ray interferometer with bent gratings: towards larger fields of view," *Nuclear Instruments and Methods in Physics Research Section A: Accelerators, Spectrometers, Detectors and Associated Equipment*, vol. 648, Supplement 1, pp. S302–5, 2011.

[140] D. Noda, M. Tanaka, K. Shimada, W. Yashiro, A. Momose, and T. Hattori, "Fabrication of large area diffraction grating using LIGA process," *Microsystem Technologies*, vol. 14, pp. 1311–5, 2008.

[141] K. Ignatyev, P. R. T. Munro, D. Chana, R. D. Speller, and A. Olivo, "Coded apertures allow high-energy X-ray phase contrast imaging with laboratory sources," *Journal of Applied Physics*, vol. 110, pp. 014 906–8, 2011.

[142] S. Berujon, H. Wang, I. Pape, K. Sawhney, S. Rutishauser, and C. David, "X-ray submicrometer phase contrast imaging with a Fresnel zone plate and a two dimensional grating interferometer," *Optics Letters*, pp. 1622–4, 2012.

[143] K. S. Morgan, D. M. Paganin, and K. K. W. Siu, "Quantitative single-exposure X-ray phase contrast imaging using a single attenuation grid," *Optics Express*, vol. 19, pp. 19 781–9, 2011.

[144] T. E. Gureyev, D. M. Paganin, A. W. Stevenson, S. C. Mayo, and S. W. Wilkins, "Generalized eikonal of partially coherent beams and its use in quantitative imaging," *Physical Review Letters*, vol. 93, p. 068103, 2004.

[145] M. R. Teague, "Image formation in terms of the transport equation," *Journal of the Optical Society of America A*, vol. 2, pp. 2019–26, 1985.

[146] R. T. Frankot and R. Chellappa, "A method for enforcing integrability in shape from shading algorithms," *IEEE Transactions on Pattern Analysis and Machine Intelligence*, vol. 10, pp. 439–51, 1988.

[147] C. Kottler, C. David, F. Pfeiffer, and O. Bunk, "A two-directional approach for grating based differential phase contrast imaging using hard X-rays," *Optics Express*, vol. 15, pp. 1175–81, 2007.

[148] M. Engelhardt, J. Baumann, M. Schuster, C. Kottler, F. Pfeiffer, O. Bunk, and C. David, "Inspection of refractive X-ray lenses using high-resolution differential phase contrast imaging with a microfocus X-ray source," *Review of Scientific Instruments*, vol. 78, pp. 093 707–15, 2007.

[149] V. Ronchi, "Le frange di combinazioni nello studio delle superficie e dei sistemi ottici," *Rivista d'Ottica e Meccanica di precisione*, vol. 2, pp. 9–35, 1923.

[150] V. Ronchi, "Due nuovi metodi per lo studio delle superficie e dei sistemi ottici," *Annali della Scuola Normale Superiore di Pisa - Classe di Scienze*, vol. 15, pp. 1–50, 1927.

[151] O. Kafri, "Noncoherent method for mapping phase objects," *Optics Letters*, vol. 5, pp. 555–7, 1980.

[152] O. Kafri and A. Livnat, "Reflective surface analysis using Moiré deflectometry," *Applied Optics*, vol. 20, pp. 3098–100, 1981.

[153] A. Asundi and K. H. Yung, "Phase-shifting and logical Moiré," *Journal of the Optical Society of America A*, 1991.

[154] Y. Nakano and K. Murata, "Talbot interferometry for measuring the small tilt angle variation of an object surface," *Applied Optics*, vol. 25, pp. 2475–7, 1986.

[155] Y. Nakano, "Measurements of the small tilt-angle variation of an object surface using Moiré interferometry and digital image processing," *Applied Optics*, vol. 26, pp. 3911–4, 1987.

[156] P. Wu, F. Yu, Z. Li, Z. Yan, and Y. Shun, "Analysis technique for the measurement of a three-dimensional object shape," *Applied Optics*, vol. 32, pp. 737–42, 1993.

[157] ESRF, *Purple Book: Science and Technology Programme 2008-2017.* ESRF editor, 2007.

[158] R. Signorato and M. S. del Rio, "Structured slope errors on real X-ray mirrors: ray tracing versus experiment," P. Z. Takacs and T. W. Tonnessen, Eds., vol. 3152. SPIE, 1997.

[159] P. Revesz, A. Kazimirov, and I. Bazarov, "Optical measurement of thermal deformation of multilayer optics under synchrotron radiation," *Nuclear Instruments and Methods in Physics Research Section A: Accelerators, Spectrometers, Detectors and Associated Equipment*, vol. 582, pp. 142–5, 2007.

[160] E. Ziegler, L. Peverini, I. V. Kozhevnikov, T. Weitkamp, and C. David, "On-line mirror surfacing monitored by X-ray shearing interferometry and X-ray scattering," *AIP Conference Proceedings*, vol. 879, pp. 778–81, 2007.

[161] H. Yumoto, H. Mimura, S. Matsuyama, S. Handa, Y. Sano, M. Yabashi, Y. Nishino, K. Tamasaku, T. Ishikawa, and K. Yamauchi, "At-wavelength figure metrology of hard X-ray focusing mirrors," *Review of Scientific Instruments*, vol. 77, p. 063712, 2006.

[162] I. Glatt and O. Kafri, "Moiré deflectometry–ray tracing interferometry," *Optics and Lasers in Engineering*, vol. 8, pp. 277–320, 1988.

[163] B. F. Oreb and R. G. Dorsch, "Profilometry by phase-shifted Talbot images," *Applied Optics*, vol. 33, 1994.

[164] S. Mirza and C. Shakher, "Surface profiling using phase shifting Talbot interferometric technique," *Optics Engineering*, vol. 44, 2005.

[165] J. D. Hoffman, *Numerical Methods for Engineers and Scientists, Second Edition*. Marcel Dekker, 2001.

[166] B. Lengeler, C. Schröer, J. Tümmler, B. Benner, M. Richwin, A. Snigirev, I. Snigireva, and M. Drakopoulos, "Imaging by parabolic refractive lenses in the hard X-ray range," *Journal of Synchrotron Radiation*, vol. 6, pp. 1153–67, 1999.

[167] H. Wang, S. Berujon, and K. Sawhney, "Characterization of a one dimensional focusing compound refractive lens using the rotating shearing interferometer technique," *AIP Conference Proceedings*, vol. 1466, pp. 223–8, 2012.

[168] L. Peverini, I. V. Kozhevnikov, A. Rommeveaux, P. V. Vaerenbergh, L. Claustre, S. Guillet, J. Y. Massonnat, E. Ziegler, and J. Susini, "Ion beam profiling of aspherical X-ray mirrors," *Nuclear Instruments and Methods in Physics Research Section A: Accelerators, Spectrometers, Detectors and Associated Equipment*, vol. 616, pp. 115–8, 2010.

[169] I. Preda, A. Vivo, F. Demarcq, S. Berujon, J. Susini, and E. Ziegler, "Ion beam etching of a flat silicon mirror surface: a study of the shape error evolution," *Nuclear Instruments and Methods in Physics Research Section A: Accelerators, Spectrometers, Detectors and Associated Equipment*, 2012.

[170] K. J. S. Sawhney, S. G. Alcock, and R. Signorato, "A novel adaptive bimorph focusing mirror and wavefront corrector with sub-nanometre dynamical figure control," p. 780303, 2010.

[171] K. Yamauchi, H. Mimura, K. Inagaki, and Y. Mori, "Figuring with subnanometer-level accuracy by numerically controlled elastic emission machining," *Review of Scientific Instruments*, vol. 73, pp. 4028–33, 2002.

[172] R. K. Tyson, *Principles of Adaptive Optics, Third Edition*, ser. Series in Optics and Optoelectronics. CRC Press, 2010.

[173] S. Barnett, *Matrices: methods and applications*, ser. Oxford Applied Mathematics & Computing Science Series. Clarendon Press, 1990.

[174] R. Huang, "The inverse problem of bimorph mirror tuning on a beamline," *Journal of Synchrotron Radiation*, vol. 18, pp. 930–7, 2011.

[175] T. J. Davis, D. Gao, T. E. Gureyev, A. W. Stevenson, and S. W. Wilkins, "Phase-contrast imaging of weakly absorbing materials using hard X-rays," *Nature*, vol. 373, pp. 595–8, 1995.

[176] C. Holzner, M. Feser, S. Vogt, B. Hornberger, S. B. Baines, and C. Jacobsen, "Zernike phase contrast in scanning microscopy with X-rays," *Nature Physics*, vol. 6, pp. 883–7, 2010.

[177] A. Momose, Y. Takeda, W. Yashiro, A. Takeuchi, and Y. Suzuki, "X-ray phase tomography with a Talbot interferometer in combination with an X-ray imaging microscope," *Journal of Physics: Conference Series*, vol. 186, p. 012044, 2009.

[178] K. L. Baker, "X-ray wavefront analysis and phase reconstruction with a two-dimensional shearing interferometer," *Optical Engineering*, pp. 086 501–5, 2009.

[179] C. David, S. Gorelick, S. Rutishauser, J. Krzywinski, J. Vila-Comamala, V. A. Guzenko, O. Bunk, E. Farm, M. Ritala, M. Cammarata, D. M. Fritz, R. Barrett, L. Samoylova, J. Grunert, and H. Sinn, "High-efficiency Fresnel zone plates for hard X-rays by 100 keV e-beam lithography and electroplating," *Journal of Synchrotron Radadiation*, vol. 18, pp. 442–6, 2011.

[180] T. Simchony, R. Chellappa, and M. Shao, "Direct analytical methods for solving poisson equations in computer vision problems," *IEEE Transactions on Pattern Analysis and Machine Intelligence*, vol. 12, pp. 435–46, 1990.

[181] H. H. Wen, E. E. Bennett, R. Kopace, A. F. Stein, and V. Pai, "Single-shot X-ray differential phase-contrast and diffraction imaging using two-dimensional transmission gratings," *Optics Letters*, vol. 35, pp. 1932–34, 2010.

[182] P. R. Munro, K. Ignatyev, R. D. Speller, and A. Olivo, "Phase and absorption retrieval using incoherent X-ray sources," *Proceedings of the National Academy of Sciences*, vol. 109, pp. 13 922–7, 2012.

[183] S. C. Mayo and B. Sexton, "Refractive microlens array for wave-front analysis in the medium to hard X-ray range," *Optics Letters*, vol. 29, pp. 866–8, 2004.

[184] W. Yashiro, Y. Takeda, A. Takeuchi, Y. Suzuki, and A. Momose, "Hard-X-ray phase-difference microscopy using a Fresnel zone plate and a transmission grating," *Physical Review Letters*, vol. 103, p. 180801, 2009.

[185] S. Schleede, M. Bech, K. Achterhold, G. Potdevin, M. Gifford, R. Loewen, C. Limborg, R. Ruth, and F. Pfeiffer, "Multimodal hard X-ray imaging of a mammography phantom at a compact synchrotron light source," *Journal of Synchrotron Radiation*, vol. 19, pp. 525–9, 2012.

List of publications

Peer-reviewed publications as first author:

1. **S. Berujon**, H. Wang, I. Pape, K. Sawhney, S. Rutishauser, and C. David, "X-ray submicrometer phase contrast imaging with a Fresnel zone plate and a two dimensional grating interferometer," *Optics Letters*, vol. **37**, pp. 1622-4, 2012.

2. **S. Berujon**, E. Ziegler, R. Cerbino, and L. Peverini, "Two-dimensional X-ray beam phase sensing," *Physical Review Letters*, vol. **108**, p. 158102, 2012.

3. **S. Berujon** and E. Ziegler, "Grating-based at-wavelength metrology of hard x-ray reflective optics," *Optics Letters*, vol. **37**, pp. 4464-6, 2012.

4. **S. Berujon**, H. Wang, and K. Sawhney, "X-ray multimodal imaging using a random-phase object," *Physical Review A*, vol. **86**, p. 063813, 2012.

5. **S. Berujon**, H. Wang, I. Pape and K. Sawhney, "X-Ray phase microscopy using the Speckle Tracking technique," *Applied Physics Letters*, 2013.

Conference proceedings as first author:

1. **S. Berujon**, H. Wang, E. Ziegler, and K. Sawhney, "Shearing interferometer spatial resolution for at-wavelength hard X-ray metrology," *AIP Conference Proceedings*, vol. **1466**, pp. 217-22, 2012.

2. **S. Berujon**, H. Wang, and K. Sawhney, "At-wavelength metrology using the X-ray speckle tracking technique: case study of a X-ray compound refractive lens," *Journal of Physics: Conference Series*, vol. **425**, p. 052020, 2013.

Peer-reviewed publications as co-author:

1. H. Wang, K. Sawhney, **S. Berujon**, E. Ziegler, S. Rutishauser, and C. David, "X-ray wavefront characterization using a rotating shearing interferometer technique," *Optics Express*, vol. **19**, pp. 16550-9, 2011.

Conference proceedings as co-author:

1. H. Wang, **S. Berujon**, and K. Sawhney, "Characterization of a one dimensional focusing compound refractive lens using the rotating shearing interferometer technique," *AIP Conference Proceedings*, vol. **1466**, pp. 223-8, 2012.

2. H. Wang, **S. Berujon**, I. Pape, S. Rutishauser, C. David, and K. Sawhney, "At-wavelength metrology using the moiré fringe analysis method based on a two dimensional grating interferometer," *Nuclear Instruments and Methods in Physics Research Section A: Accelerators, Spectrometers, Detectors and Associated Equipment*, vol. **710**, pp. 78-81, 2013.

3. I. Preda, A. Vivo, F. Demarcq, **S. Berujon**, J. Susini, and E. Ziegler, "Ion beam etching of a flat silicon mirror surface: A study of the shape error evolution," *Nuclear Instruments and Methods in Physics Research Section A: Accelerators, Spectrometers, Detectors and Associated Equipment*, vol. **710**, pp. 98-100, 2013.

4. K. Sawhney, S. Alcock, J. Sutter, **S. Berujon**, H. Wang, and R. Signorato, "Characterisation of a novel super-polished bimorph mirror," *Journal of Physics: Conference Series*, vol. **425**, p. 052026, 2013.

5. H. Wang, **S. Berujon**, and K. Sawhney, "Development of at-wavelength metrology using grating-based shearing interferometry at Diamond Light Source," *Journal of Physics: Conference Series*, vol. **425**, p. 052021, 2013.

Appendices

A Symbols and acronyms

Acronym	
ESRF	European Synchrotron Radiation Facility
DLS	Diamond Light Source
XGI	X-ray Grating Interferometer
XST	X-ray Speckle Tracking
CRL	Compound Refractive Lens
FZP	Fresnel Zone Plate
LTP	Long Trace Profiler
NOM	Nanometer Optical Measuring machine
KB	Kirkpatrick-Baez system
AFM	Atomic Force Microscope
CCD	Charge-Coupled Device
X-FEL	X-ray Free Electron Laser
TIE	Transport of Intensity Equation
GPU	Graphics Processing Unit
DBT	Deflection Based Techniques
IBF	Ion Beam Figuring
EEM	Elastic Emission Machining

Table A.1: Symbols table

Symbol	
λ	Wavelength
E	Photon energy
∇	The del operator
G_1	Phase grating of the XGI
G_2	Absorption grating of the XGI
p_1 and p_2	Grating pitch
W	Beam wavefront
φ	Beam phase
Φ	Moiré fringes phase
k	Wavenumber
$\mathbf{k}$	Wavevector

Table A.2: Symbols table

B Ellipse equation useful for mirror shaping

The general ellipse equation in the base (e_u, e_v) is:

$$\frac{x_{e_u}^2}{a^2} + \frac{y_{e_v}^2}{b^2} = 1 \tag{B.1}$$

Retaining only the negative solution (mirror oriented reflective side up):

$$y_{e_v} = -b\sqrt{1 - \frac{x_{e_u}^2}{a^2}} \tag{B.2}$$

The source and focus position are defined by:

$$SX_0 + X_0F = p + q = cst \tag{B.3}$$

Considering the point of the ellipse p_1, one can derive the relation linking a to $p + q$ by:

$$\begin{aligned} p + q &= (a - c) + a + c = 2a \\ a &= \frac{p+q}{2} \end{aligned} \tag{B.4}$$

When considering the point p_2, we have: $p = q = a$ and then:

$$a^2 = b^2 + c^2 \tag{B.5}$$

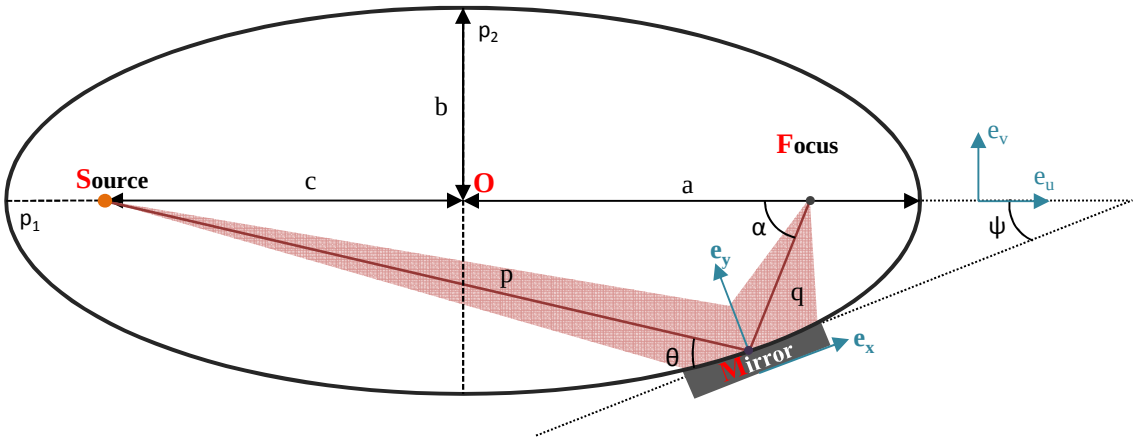

Figure B.1: Geometry considerations for the derivation of the ellipse equations. S, F are respectively the source and focal point while M is the center of the mirror.

Using the Al-Kashi formulae in the triangle SFX_0:

$$c = \frac{1}{2}\sqrt{p^2 + q^2 - 2pq\cos(\pi - 2\Theta)} \tag{B.6}$$

And the expression of b with p and q is:

$$\begin{aligned} b^2 &= a^2 - c^2 \\ &= \frac{1}{2}pq(1 + \cos 2\Theta) \end{aligned}$$

And so

$$b = \sqrt{pq}\sin\Theta \tag{B.7}$$

In the triangle SFM, the following relation hold:

$$\frac{sin(\pi - 2\Theta)}{p} = \frac{\sin\alpha}{2c} \tag{B.8}$$

leading to

$$\alpha = \arcsin\left(\frac{p}{2c}\sin(\pi - 2\Theta)\right) \tag{B.9}$$

The rotation angle Ψ between the ellipse axis (e_u, e_v) and the mirror axis (e_x, e_y) is:

$$\Psi = \alpha - \Theta \tag{B.10}$$

The coordinate of the point M are:

$$\begin{aligned} x_0 &= c - q\cos\alpha \\ y_0 &= -b\sqrt{1 - \frac{x_0^2}{a^2}} \end{aligned} \tag{B.11}$$

After rotation and translation to the base (e_x, e_y) centered in M, the relation of the base vectors of the two bases at the first order approximation are:

$$\begin{aligned} x_{e_u} &= x_0 + x_{e_x}\cos\Psi - y_{e_y}\sin\Psi \approx x_0 + x_{e_x}\cos\Psi \\ y_{e_v} &= y_0 + y_{e_y}\cos\Psi + x_{e_x}\sin\Psi \end{aligned} \tag{B.12}$$

Then:

$$y_{e_v} = -b\sqrt{1 - \frac{x_{e_u}^2}{a^2}} \tag{B.13}$$

becomes by substitution of the coordinates:

$$y_0 + y_{e_y}\cos\Psi + x_{e_x}\sin\Psi = -b\sqrt{1 - \left(\frac{x_0 + x_{e_x}\cos\Psi}{a}\right)^2} \tag{B.14}$$

and finally:

$$y_{e_y} = -\frac{1}{\cos\Psi}\left(b\sqrt{1 - \left(\frac{x_0 + x_{e_x}\cos\Psi}{a}\right)^2} + y_0\right) - x_{e_x}\tan\Psi \tag{B.15}$$

And from a straight forward derivation, the slope is:

$$Sl = y'_{e_y} = \frac{b}{a} \frac{x_0 + x_{e_x} \cos \Psi}{\sqrt{a^2 - x_0^2 - 2x_0 x \cos \mu - x^2 \cos^2 \mu}} - \tan \Psi \tag{B.16}$$

However, these two last equations correspond to the mirror profile and slope in the referential of the mirror center(which is not the deepest point). For the etching process, the target slope has to be considered when the mirror is set horizontally, or more precisely, with its two extrema at the same altitude. To account for this, another rotation has to be performed with an angle:

$$\Theta = -atan\left(\frac{y_{e_y}(\frac{L}{2}) - y_{e_y}(-\frac{L}{2})}{L}\right) \tag{B.17}$$

where L is the mirror length. This is also equivalent to:

$$Sl_{flat} = Sl - < Sl > \tag{B.18}$$

where the operator $< . >$ denotes the average value over the definition space.
Beside that, the theoretical radius of the ellipse is defined by :

$$R_{th} = \frac{2}{sin\Theta}\left(\frac{pq}{p+q}\right) \tag{B.19}$$

C XST data processing

XST implementation steps

With two acquisition of size *(m*n)*